Characterization of thermo-viscoplastic behavior of the metallic alloys under dynamic biaxial loadings

Jiabin Liang

DOCTORAT BRETAGNE LOIRE SCIENCES POUR L'INGENIEUR

INSA RENNES

THESE DE DOCTORAT DE

L'INSTITUT NATIONAL DES SCIENCES APPLIQUEES RENNES

ECOLE DOCTORALE N° 602
Sciences pour l'Ingénieur
Spécialité : *Génie Mécanique*

Par

Jiabin LIANG

Characterization of thermo-viscoplastic behavior of metallic alloys under dynamic biaxial loadings

Thèse présentée et soutenue à Rennes, le 03/06/2020
Unité de recherche : Laboratoire de Génie Civil et Génie Mécanique (LGCGM), INSA Rennes
Thèse N° : 20ISAR 06 / D20 - 06

Rapporteurs avant soutenance :

Nathalie Boudeau	Professeur des Universités, ENSMM, Besançon
Carl Labergère	Professeur des Universités, Université de Technologie de Troyes

Composition du Jury :

Président :	Fodil Meraghni	Professeur des Universités, ENSAM, Metz
Examinateurs :	Nathalie Boudeau	Professeur des Universités, ENSMM, Besançon
	Dominique Guines	Maître de Conférences, INSA Rennes
	Carl Labergère	Professeur des Universités, Université de Technologie de Troyes
Dir. de thèse :	Lionel Léotoing	Maître de Conférences HDR, INSA Rennes

Remerciements

Avant tout, je voudrais remercier sincèrement mes superviseurs, Dr Lionel LEOTOING et Dr Dominique GUINES pour leurs aides pendant mes études doctorales au Laboratoire de génie civil et mécanique (LGCGM). Je voudrais encore les remercier beaucoup pour leurs patiences et leurs conseils sur mon sujet de recherche. Leurs styles d'enseignement et leurs connaissances approfondies m'ont beaucoup aidé et m'ont permis de mieux faire mes recherches. Je voudrais encore les exprimer mes sincères remerciements pour m'avoir aidé avec dévouement.

D'ailleurs, je tiens à remercier le temps, les efforts et les conseils professionnels des professeurs Boudeau Nathalie, Labergere Carl et Meraghni Fodil en tant que membres de mon comité de thèse de doctorat. J'aimerais remercier pour leurs suggestions éclairantes et leurs commentaires encourageants.

Aussi, j'aimerais en particulier remercier les ingénieurs de l'équipe GMA pour leur préparation des échantillons et leur soutien technique.Je n'aurais pas pu accomplir ce travail seul sans leur aide précieuse.

J'aimerais également exprimer mes remerciements particuliers au China Scholarship Council (CSC) pour son soutien financier pendant mon travail, ainsi qu'à la faculté du CSC pour son aimable assistance dans ma vie pendant mon séjour en France.

Enfin, je tiens à exprimer mes remerciements les plus sincères à mon épouse, mes parents et mes amis. Leurs compagnonnages, leur soutien sans faille et la confiance qu'ils m'ont accordée sont les atouts les plus importants de ma vie et les motivations qui me permettent de continuer à avancer .

Abstract

Sheet metal forming processes are widely adopted in industries to produce thin-wall parts. Nowadays, with increasing demands for safety, lower weight or reduced fabrication costs, new materials and innovative forming processes emerge. In order to reduce the amount of the time-consuming and expensive trial-and-error processes, Finite Element (FE) simulations are intensively used to analyze the capabilities of sheet metal forming processes. To improve the accuracy of FE models, the material must be characterized for conditions close to the ones encountered in practice. In sheet metal forming processes, the material is deformed under biaxial loading states and is subjected to large strains. Hence, the identification of material constants, corresponding to the different behavior models (yield criterion, plastic hardening, temperature and strain rate dependencies …), under biaxial tensile states has become a basic issue for the characterization of phenomenological models.

The objective of this thesis is to propose calibration methods of thermo-viscoplastic models of metallic alloys submitted to in-plane biaxial tensile loadings. In this case, AA6061 is adopted to study the temperature and strain rate effect on plastic behavior through experimental and numerical approaches.

Anisotropic behavior of AA6061 is investigated by mean of uniaxial tests and equi-biaxial tensile tests at room temperature and quasi-static conditions. The equi-biaxial tensile test on a simple specimen shape is performed to calibrate a complex yield criterion with an improved method.

Based on these uniaxial tensile tests also performed at various temperatures (ambient to 200°C) and strain rate ($0.002s^{-1}$ to $4s^{-1}$), a coupled hardening temperature-strain rate model is identified for AA6061. Then, a heating device is introduced and equipped with the biaxial tensile machine. To study the temperature and strain rate dependent hardening behavior for large strains, the biaxial tensile tests with a dedicated cruciform specimen are performed at temperatures (ambient to 160°C) and strain rates ($10^{-3}s^{-1}$ to $10s^{-1}$) close to the ones of the uniaxial tests. The coupled hardening model selected previously from uniaxial tension experiments is calibrated by inverse analysis, based on the results of the equi-biaxial tensile tests.

Contents

Figures

Tables

Notations

ε_{ij}	Component of strain tensors
ε_i	Component of principal strains
$\bar{\varepsilon}_p$	Equivalent plastic strain
$\dot{\bar{\varepsilon}}_p$	Equivalent plastic strain rate
σ_{ij}	Component of stress tensors
$\bar{\sigma}$	Equivalent stress
σ_0	Initial yield stress
r_θ	Anisotropic coefficients of Lankford parameters
T	Currently temperature
T_0	Reference temperature
T_m	Material melting temperature
E	Young's modulus
υ	Poisson ratio
t	Time

AA	Aluminum alloy
DIC	Digital image correlation
diag	Diagonal direction
Exp	Experimental data
Num	Numerical data

General introduction

Sheet metal forming processes are widely adopted in industries to produce thin-wall parts. Nowadays, with increasing demands for safety, lower weight or reduced fabrication costs, new materials and innovative forming processes emerge. In order to reduce the amount of the time-consuming and expensive trial-and-error processes, Finite Element (FE) simulations are intensively used to analyze the capabilities of sheet metal forming processes. To improve the accuracy of FE models, the material must be characterized for conditions close to the ones encountered in practice. In sheet metal forming processes, the material is deformed under biaxial loading states and is subjected to large strains. Hence, the identification of material constants, corresponding to the different behavior models (yield criterion, plastic hardening, temperature and strain rate dependencies …), under biaxial tensile states has become a basic issue for the characterization of phenomenological models.

Characterization of material behavior under biaxial tensile states can be performed by different tests (hydraulic bulge test of circular specimen, tension-internal pressure test of tubular specimen, biaxial tensile test of flat cruciform specimen, …). Considering the in-plane biaxial tensile test, a cruciform specimen is directly loaded along two perpendicular directions. This test presents several benefits: first, it is a frictionless test without any contact between the tested specimen and tools; moreover, many strain paths ranging from uniaxial tension to biaxial tension can be encountered during the same test in different regions of the specimen; finally, by changing the displacement ratio between the two perpendicular axes, different linear or non-linear biaxial strain and stress states can be obtained in the central region of the specimen. Nevertheless, the main drawback of this test is related to the design of the cross specimen. Several attempts of cruciform shape design have been led these last years. Depending on the targeted application (determination of forming limit strains, calibration of a plastic yield criterion, identification of a hardening behaviour for large strains …) different specimen shapes have been proposed.

The objective of this work is to propose a calibration method of thermo-viscoplastic models of metallic alloys based on an in-plane biaxial tensile test. The calibration methodologies developed these lasts years in the team to characterize the strain-rate dependency of metallic alloys under in-plane biaxial loadings are extended in order to integrate the temperature dependency. For this purpose, an experimental database including both conventional uniaxial tensile tests as well as equi-biaxial tensile tests on dedicated flat cruciform specimens of AA6061 are carried out at different temperatures and strain rates. Based on these experimental data, different strategies for calibrating the thermo-viscoplastic strain-hardening model and the yield criterion are evaluated and discussed. The main content of this work is presented in 4 chapters as follows: Chapter 1 briefly recalls the constitutive models needed to describe the thermo-viscoplastic behavior of metal sheets. Main yield criteria used in sheet forming modeling and various hardening laws including thermal softening effect and strain rate sensitivity suggested in previous works are presented. Then, after a brief recall of the conventional experimental methods used to calibrate the constitutive models implemented in numerical simulation codes, the bibliography focuses on the use of in-plane biaxial tensile test

on cruciform specimens. The different applications of this rheological test are reviewed and particular attention is paid to the experimental devices developed to carry out temperature characterizations.

In Chapter 2, the mechanical behavior of AA6061 is investigated by means of conventional uniaxial tensile tests. Firstly, through tests at ambient temperature along three directions at 0°, 45° and 90° from the rolling direction, the anisotropy coefficients for this material are calculated. Then, the uniaxial tensile tests are performed at different temperatures and tensile velocities to evaluate the temperature and strain rate influences on the hardening behavior of AA6061. Based on this experimental database, several temperature and strain rate dependent hardening models selected from the literature review are calibrated. By comparing the predicted results with experimental ones, the best model is chosen to further investigate the hardening behavior of AA6061 under biaxial tension at different temperatures and strain rates.

In Chapter 3, equi-biaxial tensile tests are performed on dedicated cruciform specimens of AA6061 at temperatures from ambient to 160°C and for an intermediate strain rate range. A FE model of the biaxial tensile test on cruciform specimen is defined to be used in an inverse procedure of identification of the material parameters of the thermo-viscoplastic model selected in chapter 2. The best set of parameters is obtained by minimizing the difference between experimental and numerical principal strains at the center point of the cruciform specimen for each temperature and tensile speed.

In Chapter 4, an equi-biaxial tensile test is performed on a cut type cruciform specimen of AA6061. From the in-plane major and minor strains along three specified paths, the complex anisotropic yield criterion of Bron and Besson is calibrated at room temperature and under quasi-static condition. This yield model and the thermo-viscoplastic hardening model identified in Chapter 3 are both used to simulate the equi-biaxial tensile tests for different operating conditions of temperature and strain rate. The evolution of predicted principal strains along different paths of the cruciform specimen are then compared to the experimental data to discuss the temperature and strain rate influence on the anisotropic behavior of the material.Finally, a summary of contributions of this work is given and some perspectives for further research on this subject are proposed.

Chapter 1 Characterization of thermo-viscoplastic behavior of metallic alloys

1.1 Introduction

In sheet metal forming process (stamping, hydroforming, incremental forming …) , the material is usually deformed under multi-axial states and large plastic strains can be reached. Moreover, these forming processes can be carried out at different temperatures to improve the formability of metallic alloys, in particular for aluminium alloys, while the strain rate may vary in a so-called "intermediate" range (from quasi-static to few tens of s^{-1}). Thus, the identification of thermo-visco-plastic constitutive models suitable for representing the mechanical behavior of sheet metal under biaxial tensile stress states has become a basic issue. In this chapter, a brief review of constitutive models usually encountered in finite element (FE) simulations of forming processes is firstly introduced. Main isotropic and anisotropic yield criteria and temperature and strain rate dependent hardening models for metallic alloys are briefly presented and discussed. Then, conventional experimental method commonly used to investigate temperature and strain rate influences on the mechanical behavior of sheet metal are presented. Finally, a short review of the in-plane biaxial tensile testing technics proposed in the literature to characterize the mechanical behavior of sheet metal is presented.

1.2 Constitutive model of metallic alloys

The accuracy of the FE simulation of sheet metal forming process depends on the use of constitutive model that should precisely describe the material response to different mechanical and/or thermal loading conditions [1]. The constitutive models can be divide into three parts:

1) A yield criterion, which can define the initial plastic response of the material and formulate the relationship between the stress components when plastic yielding happens.
2) A flow rule which governs the relationship between increments of plastic strain and stress after initiation of plastic deformation.
3) A hardening law which describes the evolution of yield stress during the forming process according to the level of deformation in the material.

1.2.1 Yield criterion

The onset of plastic deformation for a material takes place when the stress components meet a certain relationship, which is called the yield criterion. There are two alternative way to describe the yield criterion: micromechanical or phenomenological approach [2]. In this thesis, only the phenomenological yield models are discussed. These yield criteria are usually described by the function *f* as follows:

$$f\left(\sigma_{ij},\sigma_0\right)=\psi\left(\sigma_{ij}\right)-\sigma_0 \tag{1.1}$$

Where $\psi\left(\sigma_{ij}\right)=\bar{\sigma}$ defines the equivalent stress, and σ_0 is the yield stress which is often considered equal to the uniaxial yield stress along the rolling direction. When $f \prec 0$, the material is under elastic deformation thus reversible. When $f=0$, non-reversible plastic deformation occurs. The yield function is a mathematical description of a three-dimension

surface in the principal stress space. Under plane stress condition (usually encountered in sheet metal forming), the yield surface is transformed to a curve as shown in Fig. 1.1.

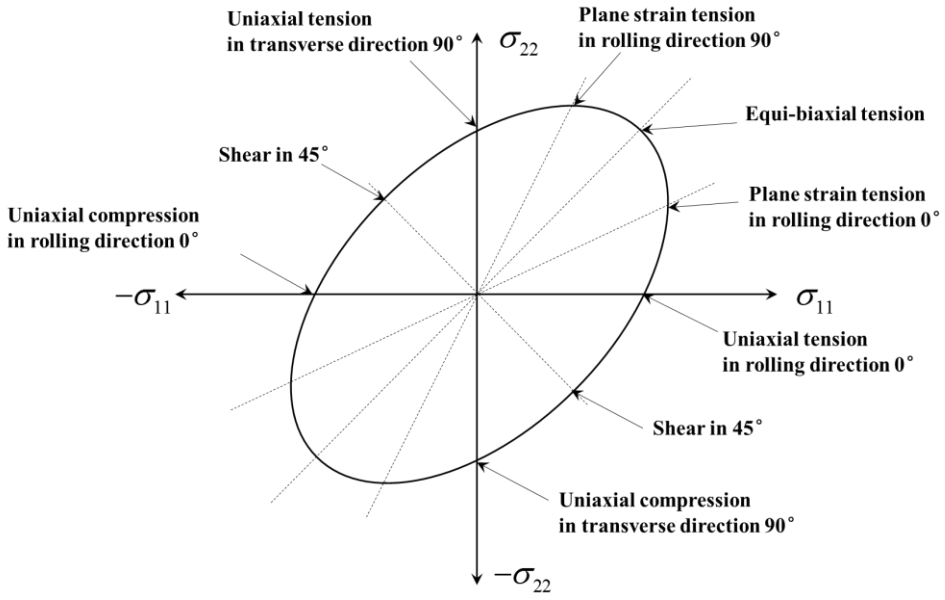

Fig. 1.1 Yield surface under plane stress condition.

Depending on the material, isotropic or anisotropic yield criteria can be adopted to well describe the plastic yielding. Here, the classic isotropic yield criteria Tresca, Mises and anisotropy yield criteria are briefly introduced in the following section.

1.2.1.1 Isotropic yield criterion

For the isotropic materials, plastic yielding depends only on the magnitude of the principal stresses and not on their directions [3]. The commonly used isotropic yield models are the Tresca model and the Von Mises model.

- **Tresca yield criterion**

The Tresca model is proposed based on the assumption that plastic yield occurs when a critical value of shear stress was reached. In general cases, the function can be written in the form:

$$\psi(\sigma_i) = \max\left\{|\sigma_1 - \sigma_2|, |\sigma_1 - \sigma_3|, |\sigma_2 - \sigma_3|\right\} \tag{1.2}$$

Under plane stress condition, the Eq. 1.2 becomes:

$$\psi(\sigma_i) = |\sigma_1 - \sigma_2| \tag{1.3}$$

where σ_i are the principal stresses. In the plane stress condition, the yield surface of this criterion is a hexagon as shown in Fig. 1.2.

- **Von Mises yield criterion**

In 1913, Von Mises proposed an equation for ductile materials, which is known as the Von Mises yield criterion. The material passed from elastic state to a plastic one when the elastic energy of distortion, or a shear stress or uniaxial tensile stress reaches a critical value. This criterion can be written as follow:

$$\psi\left(\sigma_{ij}\right)=\sqrt{\frac{1}{2}\left[\left(\sigma_{11}-\sigma_{22}\right)^2+\left(\sigma_{22}-\sigma_{33}\right)^2+\left(\sigma_{11}-\sigma_{33}\right)^2+6\sigma_{12}^2+6\sigma_{23}^2+6\sigma_{13}^2\right]} \tag{1.4}$$

Under plane stress conditions, the Eq. 1.4 becomes:

$$\psi\left(\sigma_{ij}\right)=\sqrt{\sigma_{11}^2+\sigma_{22}^2-2\sigma_{11}\sigma_{22}+3\sigma_{12}^2} \tag{1.5}$$

The yield surface corresponding to the Von Mises yield criterion in plane stress is an ellipse as shown in Fig. 1.2, where Y is an initial yield stress under uniaxial condition.

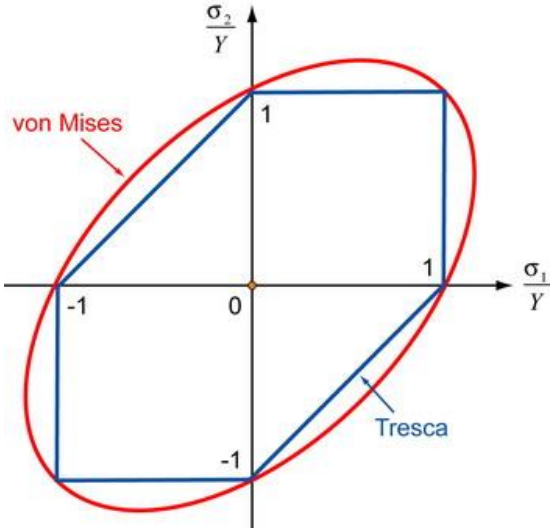

Fig. 1.2 Yield surfaces for Tresca and Von Mises yield criterion.

For isotropic material, both the preceding criteria are sufficiently accurate for approximation. Although there are major differences in the mathematical form of this two model, the values of stress predicted for any given stress ratio will not differ by more than 15% [4]. However, the Von Mises criterion is continuous and more convenient to use in numerical analysis [3].

1.2.1.2 Anisotropic yield criterion

For the anisotropic materials, plastic yielding depends not only on the magnitude of the principal stresses but also on their directions. Metallic sheets usually exhibit a significant anisotropy behavior, due to their crystallographic structure and the characteristics of rolling process [5]. Over the years, numerous anisotropic yield criteria have been developed to account for the plastic anisotropy of sheet metal.

- **Hill 1948 yield criterion**

Based on the Von Mises isotropic yield criterion, Hill [6] proposed an anisotropic yield criterion in 1948, which can be expressed by the following type:

$$\psi\left(\sigma_{ij}\right)=\sqrt{F\left(\sigma_{22}-\sigma_{33}\right)^2+G\left(\sigma_{33}-\sigma_{11}\right)^2+H\left(\sigma_{11}-\sigma_{22}\right)^2+2L\sigma_{23}^2+2M\sigma_{13}^2+2N\sigma_{12}^2} \quad (1.6)$$

Where F, G, H, L, M and N are the parameters to be identified. Under plane stress conditions ($\sigma_{13}=\sigma_{23}=\sigma_{33}=0$), the yield function can be written as:

$$\psi\left(\sigma_{ij}\right)=\sqrt{\left(H+G\right)\sigma_{11}^2+\left(H+F\right)\sigma_{22}^2+2N\sigma_{12}^2} \quad (1.7)$$

The Hill 1948 yield criterion has until recently been used frequently because of its simplicity (few parameters to identify). However, there are also drawback of the Hill 1984 [7]: (i) It can be only applied to materials forming in two or four 'ears' in axisymmetric deep-drawing process; (ii) The equivalent stress-strain curves for different materials depend on the loading path, although they should be unique and intrinsic for a given material; (iii) the dependence of the yield stress on direction is poorly predicted by this model, although the variation of the *r*-value is properly approximately.

- **Hosford yield criterion**

Hosford [8] proposed an anisotropic yield criterion based on Hershey's isotropic model which was related to the crystallographic structure of the material. It is in the form:

$$\psi\left(\sigma_{ij}\right)=\left(F\left|\sigma_{22}-\sigma_{33}\right|^a+G\left|\sigma_{33}-\sigma_{11}\right|^a+H\left|\sigma_{11}-\sigma_{22}\right|^a\right)^{1/a} \quad (1.8)$$

Where F, G and H are the parameters which describe the anisotropy. The exponent *a* is related to the crystallographic structure of the material. He concluded that the best approximation was given by *a*=6 for body centered cubic (BCC) materials and *a*=8 for FCC materials.

- **YLD 91**

Barlat et al. [9] extended Hosford anisotropic yield criterion and took into account the shear stress component with a linear transformation tensor. It is in the form:

$$\psi\left(\sigma_{ij}\right)=\frac{1}{2}\left(\left|S_1-S_2\right|^a+\left|S_1-S_3\right|^a+\left|S_2-S_3\right|^a\right) \quad (1.9)$$

Where the exponent *a* has the same significance as the one used by Hosford. S_i are the principal values of a transformed stress deviator s'_{ij} (Eq. 1.12). A linear transformation on the stress tensor σ_{ij} was introduced in the formulation, as (Eq. 1.10 and Eq. 1.11):

$$s'_{ij} = L\sigma_{ij} \tag{1.10}$$

$$L = \begin{Bmatrix} \frac{c_2+c_3}{3} & -\frac{c_3}{3} & -\frac{c_2}{3} & 0 & 0 & 0 \\ -\frac{c_3}{3} & \frac{c_1+c_3}{3} & -\frac{c_1}{3} & 0 & 0 & 0 \\ -\frac{c_2}{3} & -\frac{c_1}{3} & \frac{c_1+c_2}{3} & 0 & 0 & 0 \\ 0 & 0 & 0 & c_4 & 0 & 0 \\ 0 & 0 & 0 & 0 & c_5 & 0 \\ 0 & 0 & 0 & 0 & 0 & c_6 \end{Bmatrix} \tag{1.11}$$

$$\begin{aligned} S_{1,2} &= \frac{S_{11}+S_{22}}{2} \pm \sqrt{\left(\frac{S_{11}+S_{22}}{2}\right)^2 + S_{12}^2} \\ S_3 &= -\left(S_1+S_2\right) \end{aligned} \tag{1.12}$$

c_i are the six positive coefficients which define the anisotropy of the material. The identification process of the coefficients can be carried out with the results of uniaxial tensile tests along longitudinal, transversal and diagonal directions and equi-biaxial bulge test. The yield function YLD91 can describe the yield surface of materials processed with medium and low cold rolling reductions. The reduction ratio affects on texture and planar anisotropy of the material [10]. However, for materials processed with high cold rolling reduction, YLD91 cannot describe anisotropy with precision, a large difference was observed between experiments and prediction values for the pure shear [11].

- **Karafillis and Boyce yield criterion**

Karafillis and Boyce [12] proposed a general yield model with a linear transformation tensor. A coefficient *c* was introduced to combine an isotropic yield model and an anisotropic one. The yield model is defined by:

$$\begin{aligned} \psi\left(\sigma_{ij}\right) &= \left(\frac{1-c}{2}\psi^1 + \frac{1}{2}\psi^2\right)^{1/a} \\ \psi^1 &= \left|S_1-S_2\right|^a + \left|S_1-S_3\right|^a + \left|S_2-S_3\right|^a \\ \psi^2 &= \frac{3^a}{2^a-1}\left(\left|S_1\right|^a + \left|S_2\right|^a + \left|S_3\right|^a\right) \end{aligned} \tag{1.13}$$

In these equations, the coefficient *a* and S_i are the same significance with the one in YLD91. However, this model is still not sufficient to describe the materials processed with high cold rolling reduction [13].

- **YLD96 yield criterion**

To represent the plastic behavior of aluminum alloy with high cold rolling reductions, the YLD96 model [11] which generated from the YLD91 model is proposed. The generalization consist in giving weight factors to the terms of Eq. 1.9:

$$\psi\left(\sigma_{ij}\right)=\frac{1}{2}\left(\alpha_1\left|S_1-S_2\right|^a+\alpha_2\left|S_1-S_3\right|^a+\alpha_3\left|S_2-S_3\right|^a\right)^{1/a} \tag{1.14}$$

The coefficients *a* and S_i have the same significant with the one in YLD91; The weight factors α_1, α_2 and α_3 are related to the anisotropy of the materials and define as:

$$\begin{aligned}\alpha_1&=\alpha_x\cos^2\beta+\alpha_y\sin^2\beta\\ \alpha_2&=\alpha_x\sin^2\beta+\alpha_y\cos^2\beta\\ \alpha_3&=\alpha_{z0}\cos^2 2\beta+\alpha_{z1}\sin^2 2\beta\end{aligned} \tag{1.15}$$

In the equations above, α_x, α_y , α_{z0} and α_{z1} are the anisotropic coefficients. The parameter β can be calculated as:

$$\beta=\tan^{-1}\left(\frac{S_{11}-S_{22}}{S_{12}}\right) \tag{1.16}$$

This yield criterion has been applied to commercial AA6022-T4 sheets and presented a good match between the predicted and experimental yield stresses and *r*-values. However, the convexity of this model is still not been guaranteed.

- **Bron and Besson yield criterion**

Since the YLD91 and the Karafillis and Boyce model have the same number of parameters to control anisotropy, they have the same limitation for describing complex yield surfaces. In this case, Bron and Besson [14] proposed a 3D yield function, which is an extension of YLD91 and Karafillis and Boyce yield model, based on two linear transformation tensors. The function of this model can be written as follows:

$$\psi=\left(\sum_{k=1}^{2}\alpha^k\left(\bar{\sigma}^k\right)^a\right)^{1/a} \tag{1.17}$$

α^k are positive coefficients, and $\alpha^1+\alpha^2=1$. The $\bar{\sigma}^k$ are expressed in the form:

$$\bar{\sigma}^1=\left[\frac{1}{2}\left(\left|S_2^1-S_3^1\right|^{b_1}+\left|S_3^1-S_1^1\right|^{b_1}+\left|S_2^1-S_1^1\right|^{b_1}\right)\right]^{1/b_1} \tag{1.18}$$

$$\bar{\sigma}^2=\left[\frac{3b_2}{2^{b_2}+2}\left(\left|S_1^2\right|^{b_2}+\left|S_2^2\right|^{b_2}+\left|S_3^2\right|^{b_2}\right)\right]^{1/b_2} \tag{1.19}$$

In these equations, *a*, b_1, b_2 and α_k are parameters which define the shape of the yield

surface. S_i^k are the principal values of transformed stress deviators $s_{ij}'^k$ which were defined by :

$$s_{ij}'^k = L^k \sigma_{ij}$$

$$L^k = \begin{Bmatrix} \frac{c_2^k + c_3^k}{3} & -\frac{c_3^k}{3} & -\frac{c_2^k}{3} & 0 & 0 & 0 \\ -\frac{c_3^k}{3} & \frac{c_1^k + c_3^k}{3} & -\frac{c_1^k}{3} & 0 & 0 & 0 \\ -\frac{c_2^k}{3} & -\frac{c_1^k}{3} & \frac{c_1^k + c_2^k}{3} & 0 & 0 & 0 \\ 0 & 0 & 0 & c_4^k & 0 & 0 \\ 0 & 0 & 0 & 0 & c_5^k & 0 \\ 0 & 0 & 0 & 0 & 0 & c_6^k \end{Bmatrix} \quad (1.20)$$

c_i^k are the parameters related to the anisotropy of the material. In the in-plane stress conditions, the parameter number related to anisotropy reduces down to 8 with $c_5^k = c_6^k = 1$. When $b_1 = b_2 = a$ and the stress deviator $s_{ij}'^1 = s_{ij}'^2$, the yield function is returned to Karafillis and Boyce yield model. When $b_1 = b_2 = a$ and $\alpha^1 = 1$, the function leads to YLD91.

These five yield criterion are based on crystallographic structure of the material. Compared with the other models, the Bron and Besson yield model have more parameters to control the anisotropy, indicating a greater flexibility for this yield criterion. This model is also found to be very accurate to describe the plastic anisotropy of various aluminium sheets such as AA2024-T4, AA6022-T4, AA2090-T3, AA7075-T351 and AA5086 [14,15]. Thus, the Bron and Besson model is adopted to study the anisotropy of the material in the following work.

1.2.1.3 Influence of temperature and strain rate on yield criterion

The use of yield (isotropic or anisotropic) models in FEA is further complicated when complex loadings, such as elevated temperature and/or strain rates, have to be considered [16].

In the research of temperature and strain rate effect on the mechanical behavior of aluminum alloy, the majority are focus on the effect of elevated temperatures or strain rates on the evolution of the flow (hardening) stress. The effect of temperature and strain rate on the anisotropy of the material and how the yield surface of the aluminum alloy evolved as a function of temperature was not fully explored [17].

Abedrabbo et al. [18] have characterized the anisotropy of AA3003-H111 at different temperatures. With uniaxial tensile tests along rolling, 45° and transverse directions and bulge test, the anisotropic coefficients of YLD96 yield criterion were calculated for each temperature (25, 93, 149, 204, and 260°C), respectively.

With the anisotropic coefficients for each temperature, the curve-fitting method was used to obtain the anisotropic coefficients in function of temperature by 3rd or 5th order polynomial

functions. The comparing of yield surface are showed in Fig. 1.3.

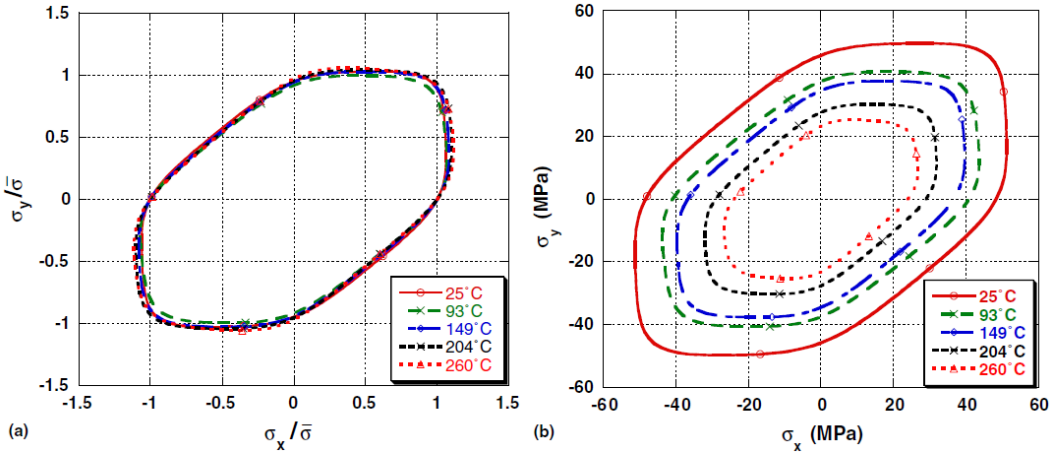

Fig. 1.3 2D-Plot of Barlat's yield function for AA3003-H111 at several elevated temperatures. (a) Stresses normalized with the flow stress to show the change in the yield surface shape. (b) Plot of actual stresses to show the change in the size of the yield surface. [18]

The curve fitting functions were verified by a comparison of the *r*-values (r_0, r_{45} and r_{90}) that were extracted from experimental tests to the values predicted from the yield function in which the anisotropy coefficients vary with temperature. A good agreement can be observed between the predicted and the experimental data at each temperature.

These results show that the temperature has an influence on the shape of the yield surface (particularly near the balanced biaxial region) and also the size, indicating that the effect of temperature on the anisotropy parameters for this material must be considered during the thermo-forming analysis.

Khan et al. [19] further considered the strain rate effect on the anisotropic coefficients of YLD96 yield criterion by characterizing the anisotropic responses of AA5182-O in a range of strain rates (10^{-4} to $1s^{-1}$) and temperatures (296 to 473K) under uniaxial tension (strain level between 14% to 18%) and compression (strain level between 3% to 10%). By comparing the predicted yield stress (σ_0 , σ_{45} , σ_{90} , and σ_b) and *r*-value (r_0, r_{45} and r_{90}) with experimental data at the same time, the anisotropy coefficients of YLD96 were adjusted to satisfy the yield stress anisotropy and *r*-value directionality simultaneously.

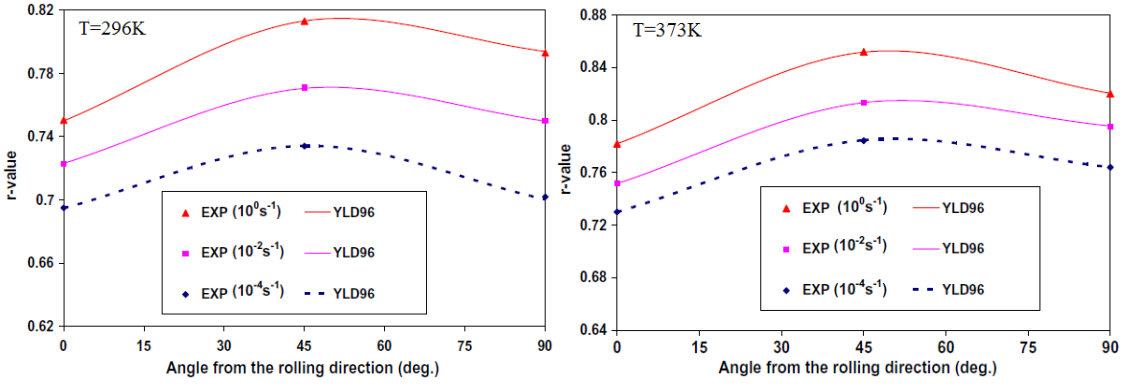

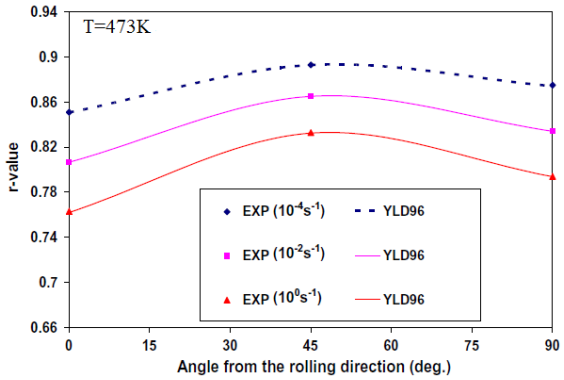

Fig. 1.4 Plot of r-value as a function of strain-rate at different temperature. [19]

The *r*-values obtained from the yield criterion are compared with the one obtained from experiments, as shown in Fig. 1.4. An evident strain rate effect on the *r*-values can be observed at different temperatures. At the temperatures of 296K and 373K, the *r*-values increase with the increasing strain rate, however, an opposite effect is observed for the temperature of 473K.

In conclusion, the strain rate effect should be considered in the characterization of anisotropy behavior for AA5182-O in this range of temperature.

From the literatures presented above, for the considered aluminium grades, anisotropic behavior of aluminium alloys seems to exhibit temperature and strain rate sensitivity.

1.2.2 Hardening law

The hardening law is used to describe the evolution of stress after the yielding of materials. The different types of hardening model consist of the isotropic hardening, kinematic hardening and the combined isotropic-kinematic hardening [20]. The subsequent yield function can be defined as follows:

$$\psi\left(\sigma_{ij}-\alpha_{ij}\right)-\bar{\sigma}=0 \tag{1.21}$$

The equivalent stress $\bar{\sigma}$ governs the size of yield surface. The position of yield in stress space is determined by the back stress α_{ij}. For the isotropic hardening, the $\alpha_{ij}=0$ and the $\bar{\sigma}$ increases with the evolution of plastic strain (Fig. 1.5a). For the kinematic hardening, the $\alpha_{ij}\neq 0$ and $\bar{\sigma}$ remains constant (Fig. 1.5b). While, when the $\alpha_{ij}\neq 0$ and the $\bar{\sigma}$ also expanded, the material is supposed to be combined isotropic-kinematic hardening (Fig. 1.5c).

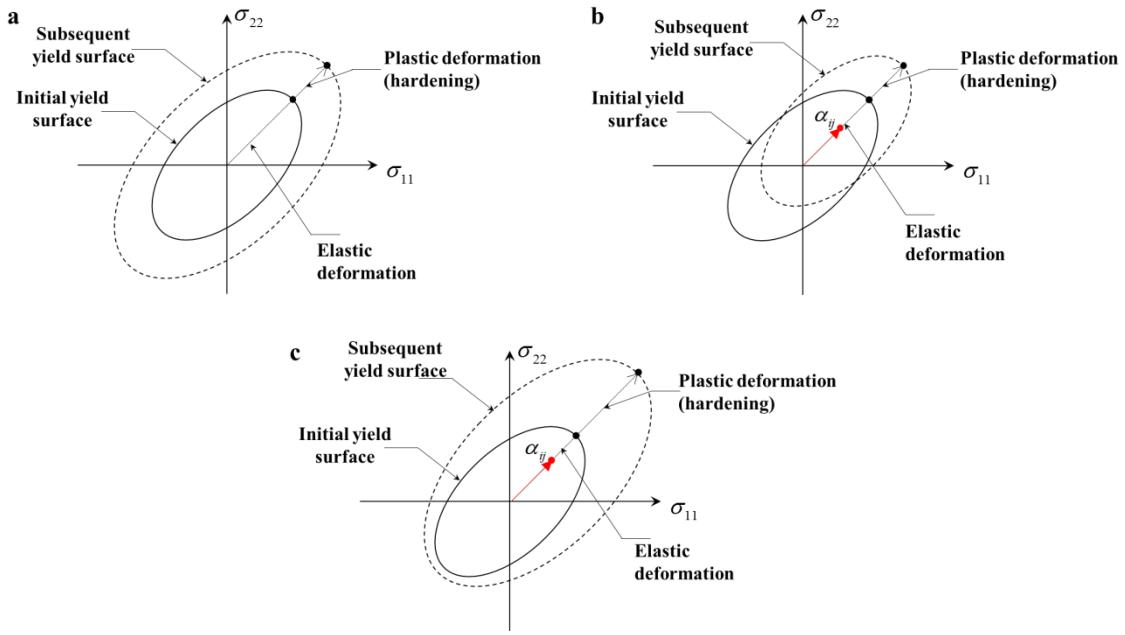

Fig. 1.5 Types of hardening law: (a) isotropic hardening; (b) kinematic hardening; (c) Combined isotropic-kinematic hardening.

For the monotonic deformation without any abrupt change of strain path, the isotropic is usually adopted. However, when there is significant change of loading direction, the kinematic or the combined isotropic-kinematical hardening should be considered, especially for the materials with Bauschinger effect under cyclic loading.

1.2.2.1 Rheological Hardening model

The hardening model are broadly classified in two major categories: physical based model and phenomenological based model, depending on the assumptions adopted for each of them [21].

Attention to physical models has increased in recent years and they are preferred in certain situations [22–26]. One of the reasons is that the material dynamic behavior at high strain rate is affected by the microstructural evolution during deformation, which is not considered in the phenomenological models [21]. However, the large number of parameters in physical models has limited their application to some extent. Physical based models are derived from the analysis of the microstructure evolution [27]. On the micro-scale, when the material is deformed, dislocations will be generated and annihilated, and the texture evolution will occur. It is usually assumed that concept of dislocation density links the flow stress to the underlying microstructure evolution. The flow stress σ can be calculated as follows [28]:

$$\sigma = \sigma_0 + \alpha \cdot G \cdot b \cdot \left(\delta - \delta_0\right) \tag{1.22}$$

Where σ_0 is the initial yield stress corresponding to the initial density δ_0 of dislocation, α is a material coefficient, G is the transversal elastic modulus, b is the burgers vector and δ is the current dislocation density.

Different from physical based models, phenomenological based models are derived from experimental observations. In general, these models present simple expressions, reduce number of material constants and are easier to implement in Finite Element code. The equivalent plastic strain $\bar{\varepsilon}_p$ is usually chosen to represent the dislocation density δ in a phenomenological model. In the similar way of Eq. 1.22, the hardening law can be expressed by a one-internal-variable model as following:

$$\bar{\sigma} = \sigma_0 + H\left(\bar{\varepsilon}_p\right) \tag{1.23}$$

Where σ_0 is the initial yield stress and $H\left(\bar{\varepsilon}_p\right)$ represents the strain hardening effect.

Ludwick and Voce models are two classical phenomenological models as the mathematical formula in Eq. 1.23. The description of these two models is given in Table 1.1.

Table 1.1 Ludwick and Voce models.

Year	Model	Expression	Feature
1909	Ludwick	$\bar{\sigma} = \sigma_0 + K\bar{\varepsilon}_p^n$	Power law
1948	Voce	$\bar{\sigma} = \sigma_0 + K\left(1 - e^{-n\bar{\varepsilon}_p}\right)$	Saturation law

Where *K* and *n* are the fitting parameters used to describe the material strain hardening.

1.2.2.2 Influence of temperature and strain rate for hardening model

When the deformation of materials take place at various temperatures and strain rates, the hardening law should also take into account the thermal softening effect $T\left(T\right)$ and the strain rate sensitivity $V\left(\dot{\bar{\varepsilon}}\right)$ [27,29].

The thermal softening effect and stain rate sensitivity effect can be incorporated additively or multiplicatively into the formulations of the hardening law [30]. For the strain rate function, the additional formulation is usually applied to high strain rate conditions which is not usually encountered in sheet metal forming. So in the following only multiplicative models are considered. In literature, one can find mainly four types of multiplicative formulations applied to the strain hardening model described by Eq. 1.23 [31]. These mathematical formulations are recalled in the Table 1.2 below.

Table 1.2 Multiplicative formulations for hardening model.

Type	Formulation	Main Feature
1	$\bar{\sigma} = \left[\sigma_0 + H\left(\bar{\varepsilon}_p\right)\right] T(T) V\left(\dot{\bar{\varepsilon}}\right)$	• Same temperature and strain rate influences on both the initial yield stress and the strain hardening.
2	$\bar{\sigma} = \sigma_0 + H\left(\bar{\varepsilon}_p\right) T(T) V\left(\dot{\bar{\varepsilon}}\right)$	• Temperature and strain rate influence only on the strain hardening.
3	$\bar{\sigma} = \sigma_0 T(T) V\left(\dot{\bar{\varepsilon}}\right) + H\left(\bar{\varepsilon}_p\right)$	• Temperature and strain rate influences only on the initial yield stress.
4	$\bar{\sigma} = \sigma_0 T_1(T) + H\left(\bar{\varepsilon}_p\right) T_2(T) V_2\left(\dot{\bar{\varepsilon}}\right)$	• Only temperature influence on the initial yield stress, but temperature and strain rate influences on the strain hardening. • Influences are different.

The thermal softening effect can lead to a significant decrease of the flow stress, especially in adiabatic forming conditions. In last decades, several temperature functions have been proposed to describe the temperature effects as recalled in [32], and summarized in Table 1.3. In these functions, T_m is the melting temperature, T_0 is the reference temperature and *T* is the current temperature.

Table 1.3 Temperature functions.

Linear model **[33]**	$T(T) = \left(1 - \beta\left(T - T_0\right)\right)$	RK model **[34]**	$T(T) = 1 - \frac{T}{T_m} \exp\left[K\left(1 - \frac{T_m}{T}\right)\right]$
Power law model **[32]**	$T(T) = \left(\frac{T}{T_0}\right)^{\beta}$	Johnson-cook model [35]	$T(T) = 1 - \left(\frac{T - T_0}{T_m - T_0}\right)^m$
Exponential model **[36]**	$T(T) = \exp\left[C\left(\frac{T - T_0}{T_m - T_0}\right)^m\right]$	Chu et al. model [27]	$T(T) = n_0 \exp\left(n_1 T\right)$

In [32], it is shown that Linear, Power, and Johnson-cook model give the same prediction at temperatures below 100°C. In [37] and [38], the use of the RK model leads to a good match in the prediction of yield stress for AA5086 and AA6061 at temperatures ranging from 20°C to 200°C. Models proposed by Chu et al. in [27] have been applied to the temperature below 200°C.

Similarly to the temperature, several functions of the strain rate sensitivity term $V\left(\dot{\bar{\varepsilon}}\right)$ are listed in Table 1.4. $\dot{\bar{\varepsilon}}_0$ represents the reference strain rate and $\dot{\bar{\varepsilon}}$ is the equivalent strain rate. The range of strain rates for which they are most commonly used in literature is given in the right-hand column of the table.

Table 1.4 Strain rate sensitivity function.

Model	**Function**	**Strain rate (s^{-1})**
Power law (Chu et al.) **[27]**	$V\left(\dot{\bar{\varepsilon}}\right)=\dot{\bar{\varepsilon}}^{m}$	0.01 to 10
Johnson-cook **[35]**	$V\left(\dot{\bar{\varepsilon}}\right)=1+C\ln\left(\frac{\dot{\bar{\varepsilon}}}{\dot{\bar{\varepsilon}}_0}\right)$	Up to 10^4
Kocks and Mecking **[39]**	$V\left(\dot{\bar{\varepsilon}}\right)=\left(\frac{\dot{\bar{\varepsilon}}}{\dot{\bar{\varepsilon}}_0}\right)^{1/m}$	10^2 to 10^4
Gavrus et al. **[40]**	$V\left(\dot{\bar{\varepsilon}}\right)=\arcsin h\left[\frac{1}{2}\left(\frac{\dot{\bar{\varepsilon}}}{\dot{\bar{\varepsilon}}_0}\right)^{m}\right]$	Around 10^3

According to the temperature and strain rate sensitivity functions presented above, the appropriated function to be chosen for a constitutive model depends mainly on the temperature and strain rate ranges concerned (i.e. encountered in the forming process).Two commonly used type-1 models (with temperature and strain rate effects on both initial yield stress and strain hardening at the same time) are given as follows:

- **Johnson-cook (JC) model**

JC model [35] is a widely used model to describe the hardening behavior with consideration of the strain hardening, strain rate sensitivity and thermal softening effect of material. This is a purely empirical hardening model. It can be written as follows:

$$\bar{\sigma}=\left(A+B\bar{\varepsilon}_p^{n}\right)\left[1+C\ln\left(\frac{\dot{\bar{\varepsilon}}}{\dot{\bar{\varepsilon}}_0}\right)\right]\left[1-\left(\frac{T-T_0}{T_m-T_0}\right)^{m}\right] \tag{1.24}$$

A is the yield stress at reference temperature T_0 and reference strain rate $\dot{\varepsilon}_0$. B is a strain hardening coefficient and n is the strain hardening exponent. C and m are material parameters that represent the coefficient of strain rate sensitive and thermal softening effect, respectively. For the JC model, there is no coupling between strain and temperature during plastic deformation. Due to its simplicity and relative few material constants, many modifications of JC model have been proposed such as [41–50]. This model is generally used for impact or fracture analyze, the strain rate can be up to $10^4 s^{-1}$, but rarely applied in sheet metal forming process.

- **Khan-Huang (KH) model**

Khan and Huang [51] studied the mechanical behavior of AA1100 in a wide strain rate range (10^{-5} to $10^4 s^{-1}$). After analyzing the experimental results, they proposed the KH hardening model, without taking into account the temperature effects. The KH model can be written as follows:

$$\bar{\sigma} = \left(\sigma_0 + E_\infty \bar{\varepsilon}_p - a e^{-\alpha \bar{\varepsilon}_p}\right)\left[1 - \frac{\ln\left(\dot{\bar{\varepsilon}}\right)}{\ln\left(\dot{\bar{\varepsilon}}_0\right)}\right]^{-1} \tag{1.25}$$

Where σ_0 , E_∞, a, α are material constants, The reference strain rate $\dot{\bar{\varepsilon}}_0$ is fixed to 10^6 by the authors. The KH model is able to predict a strong hardening behavior in a large range of strain rate. However, the lack of temperature effect led to a further modification for this model [52].

Examples for the type-2 (temperature and strain rate effects on strain hardening) and type-3 (temperature or strain rate effects on the initial yield stress) models are given as follows:

- **Zerilli-Amstrong (ZA) model**

A classic example of a type-2 model is the Zerilli-Amstrong (ZA) [53] model for FCC metals. This model is based on dislocation mechanic and incorporates the effect of strain hardening, strain rate, temperature and grain size. According to this model, the temperature and strain rate have an influence on the strain hardening, but not on the initial yield stress. The ZA model for FCC metal can be written as follows:

$$\bar{\sigma} = \sigma_a + C_1 \bar{\varepsilon}_p^{C_2} e^{-C_3 T + C_4 T \ln \dot{\bar{\varepsilon}}} \tag{1.26}$$

σ_a is an athermal component of stress that considers the contribution of the initial dislocation density for the yield stress, which can be regarded as the initial yield stress σ_0 without consideration of temperature and strain rate influence. C_i are materials parameters.

- **Modified KH model**

The modified KH model proposed by Yu et al. [54] is an example of the type-3 model. This model has been used to study the rate-dependent mechanical behavior of a DP600 steel at strain rate ranging from 10^{-4} to $1600s^{-1}$. It can be written as follows:

$$\bar{\sigma} = \sigma_0 \left[1 + D\left(\ln \frac{\dot{\bar{\varepsilon}}}{\dot{\bar{\varepsilon}}_0}\right)^m\right] + E_\infty \bar{\varepsilon}_p - a e^{-\alpha \bar{\varepsilon}_p} \tag{1.27}$$

The initial yield stress is strain rate dependent, while without consideration of temperature or strain rate effect for the strain hardening. σ_0 , a, D, E_∞ , m and α are the material parameters and the reference strain rate $\dot{\bar{\varepsilon}}_0 = 10^{-4}/s$. This model described well the hardening behavior for DP600 steel in this strain rate range and shows that the strain hardening of DP600 has little dependence on the strain rate.

Several kinds of the type-4 model have been presented and calibrated by Chu et al. [27] These kind of models are well adapted to the range of temperature and strain rate considered here.

- **Chu et al. models**

As long as type 4 models are concerned, Chu et al. [27] investigated the thermo-elasto-viscoplastic hardening behavior for AA5086 in a temperature range from 20°C to 200°C and for a strain rate range from 0.01 to 10s^{-1}. Ludwick (power law type) and Voce (saturation type) hardening models incorporating temperature and strain rate sensitivity functions have been proposed, as follows:

Ludwick model:

$$\bar{\sigma}=\sigma_0(T)+(K_1-K_2T)\bar{\varepsilon}_p^{(n_0-n_1T)}\dot{\bar{\varepsilon}}_p^{m_0\exp(m_1T)} \tag{1.28}$$

Voce model:

$$\bar{\sigma}=\sigma_0(T)+(K_1-K_2T)\left(1-\exp\left(-K_3\exp(K_4T)\bar{\varepsilon}_p\right)\right)\dot{\bar{\varepsilon}}_p^{m_0\exp(m_1T)} \tag{1.29}$$

$\sigma_0(T)$ is the initial yield stress with consideration of temperature effect. K_i, n_i, and m_i are material parameters.

In the ranges of temperature (less than 200°C) and intermediate strain rate (few ten of s^{-1}) of interest here, which also correspond to those targeted by Chu et al. [27], good predictive results were obtained by these type-4 thermo-viscoplastic strain-hardening models. However, a noticeable difference between the power and saturated type models is observed for large plastic strains as encountered in forming processes.

1.3 Conventional experimental tests for metallic material characterizations

In this part, a brief review of the conventional testing methods most commonly used to investigate the mechanical properties of sheet metal under different temperatures and strain rates is introduced. These traditional tests, including uniaxial tensile test, simple shear test, hydraulic bulge test and plane strain test, are usually adopted for characterization of plastic behavior under different stress states.

1.3.1 Uniaxial test

Uniaxial test is widely used to investigate the mechanical properties of metallic materials. It can provide the Young's modulus, Poisson's ratio, yield strength, ultimate tensile strength (UTS), uniform elongation and anisotropic coefficients. The uniaxial tensile specimen is presented below in Fig. 1.6.

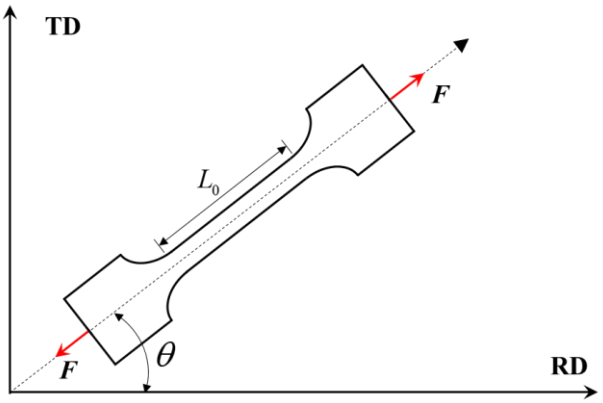

Fig. 1.6 In-plane uniaxial tensile specimen at an angle θ to the rolling direction.

The true strain, stress and strain rate can be calculated when the deformation is uniform in the central gauge area of initial length L_0 before localization, the true strain is calculated by:

$$\varepsilon = \ln \frac{L}{L_0} \tag{1.30}$$

True stress is calculated by:

$$\sigma = \frac{F}{S} = \frac{F \times \exp(\varepsilon)}{S_0} \tag{1.31}$$

Where F is the loading force. S_0 and S are the initial and current cross sections.

True strain rate is calculated by:

$$\dot{\bar{\varepsilon}} = \frac{d\varepsilon}{dt} = \frac{V}{L} \tag{1.32}$$

Where V is the loading velocity.

Based on this uniaxial tensile test, considered as homogeneous, experimental true stress-true strain curves can be obtained at different initial strain rate.

Hereafter are some examples for the uniaxial test at different temperatures and strain rates. In order to study the deformation behavior of aluminum at warm forming conditions, Li et al. [55] have performed the uniaxial tensile tests for three kinds of aluminum alloys (AA5182, AA5754, and AA6111) at different temperatures (200, 250,300, and 350°C) and for a strain rate range from 0.015s^{-1} to 1.5s^{-1}. The dependency of strain hardening and strain rate sensitivity on the temperature is identified. Abedrabbo et al. [18,56] used the uniaxial tensile test to identified the temperature-dependent anisotropic yield models for three aluminum alloys, AA3003-H111, AA5182-O and AA5754-O at the temperature range of 25 to 260°C and strain rate range of 0.001 to 0.08s^{-1}. Codrington et al. [57] identified the hardening model for AA7000-T4 at 260 and 480°C by using an induction heating apparatus with uniaxial tension. A constant

strain rate of $10^{-3}s^{-1}$ was used throughout all the tests. With the induction heater in this work, the temperature of the test specimen can reach around 1500°C, depending on the material and specimen size. Chen et al. [58] evaluated the formability of AA6061 sheet under different forming conditions. With the uniaxial tensile test at the different temperatures (room temperature, 180°C, and 380°C) and strain rates (0.0005 to $0.05s^{-1}$), the hardening exponent *n* and strain rate sensitivity index *m* are identified.

From an experimental point of view, the flow stress-strain curve under uniaxial tension is easily obtained by measuring the experimental force and the specimen elongation of the gauge area (either by a classical extensometer or by image correlation depending of the temperature level) during the test. In this case, it is highly recommended to use a heating device (e.g. an adiabatic box with a window) that provides a good field of view in the uniaxial test.

However, the maximum homogeneous strain level under uniaxial test is limited (generally less than 20% for aluminum alloy), due to the necking phenomenon. Another drawback is only the uniaxial stress state is obtained under uniaxial test, quite different to the one encountered in forming process.

1.3.2 Simple shear test

The simple shear test is commonly used to obtain the shear modulus, elastic limit and shear strength of the materials [27]. It has been proved that simple shear test is a very efficient technique to characterize the material properties of sheet metal at large strains under cyclic loadings [59]. A well-known test device for simple shear testing of sheet metal is based on the American Society for Testing and Materials Standard (ASTM B831) [60]. The ASTM standard is primarily intended to investigate the behavior of thin aluminum products under shear loading using a single shear zone. The shear testing specimen is given in Fig. 1.7(a). A modified simple shear specimen (Fig. 1.7(b)) based on the ASTM standard was developed by Merklein and Biasutti [61] to facilitate a reversal of the load direction. This opens a pathway to evaluate the material behavior under cyclic shear loading to describe kinematic hardening behavior [62].

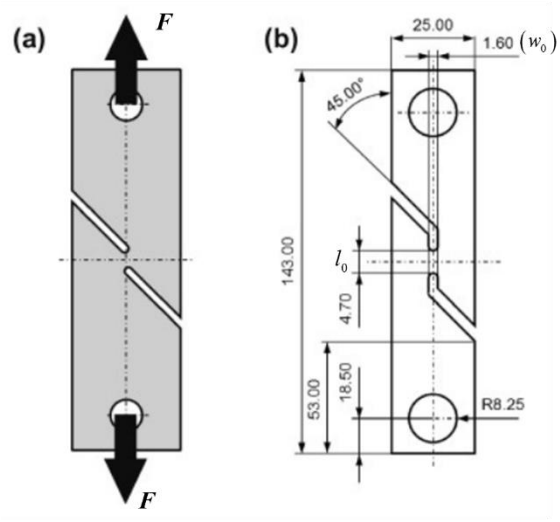

Fig. 1.7 Simple shear specimen according to (a) ASTM B831–05 standard [60] and (b) a modified ASTM specimen proposed by Merklein and Biasutti (2011) [61].

For the modified specimen, the shear zone of the specimen has an initial length of $l_0 = 4.7mm$ and width of $w_0 = 1.6mm$. The shear stress τ is determined from:

$$\tau = \frac{F}{l_0 \cdot w_0} \tag{1.33}$$

The modified ASTM specimen can be directly used in uniaxial testing machines because of its simple geometry. Hence, the heating method for uniaxial test can be adopted directly. In the investigation of plastic behavior for AA6082, Pellegrino et al. [63] performed the shear test with this shape of specimen to obtain the shear stress state from ambient temperature to 500°C. The shear strain rate is $0.001s^{-1}$. Bernard et al. [64] investigated the influence of Portevin-Le Chatelier effect on shear stress-strain curves of AA5754-O at different temperatures (25 to 200°C) and strain rates (1.2×10^{-3} to $1.2\times10^{-1}s^{-1}$) under reversal loadings. The shape of the shear specimen is shown in Fig. 1.8:

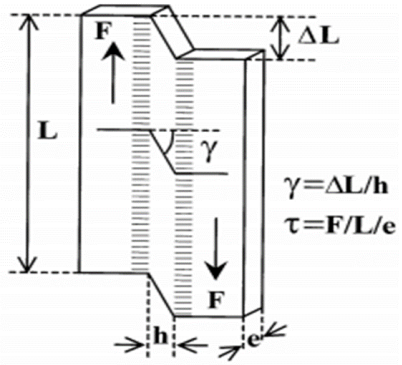

Fig. 1.8 Shape of specimen in [64].

Edwards et al. [65] investigated the temperature influence on the flow shear stress-strain curves for AA2024-T351. The dynamic shear tests were performed with a hat-shaped specimen on split Hopkinson pressure bar machine under different temperatures (ambient temperature,

125°C, and 250°C) and strain rates ($2\times10^{-3}s^{-1}, 5\times10^{3}s^{-1}$, and $17.8\times10^{3}s^{-1}$).

The simple shear test can be also performed at various temperatures and strain rates. Compared with the uniaxial test, a shear test can be used to identify failure parameters due to ductile fracture and not instability. No thinning occurs in a well-designed shear specimen, thus diffuse and localized necking is avoided. Damage growth is retarded because of the lower stress triaxiality. Generally, larger strains can be reached in shear tests, by which better material modeling is achieved [66]. Also, there are some disadvantages for simple shear test. For example, the shear stress is not homogeneously distributed over the gauge section, the tensile and compression stress exist in the shear region; uncontrolled specimen deformation occurs in the clamps which will influence the calculated strain in the gauge area; frequently, bulking and cracking arise at the borders of the shear region [67].

1.3.3 Plane strain compression test

The plane strain compression test is an useful method for extending the flow curve to large strains [68]. A schematic diagram illustrating the configuration of the plane strain compression platens and the specimen is shown in Fig. 1.9. The preferred dimensions of the specimen are given in Eq. 1.34 [69]:

$$\begin{cases} h \le 0.6w \\ b = 5w \\ 1 > 3w \end{cases} \tag{1.34}$$

The stress and strain components can be calculated with the equations as follows, and the respective strain and stress can be obtained.

$$\begin{aligned} \sigma_{11} &= \frac{P}{b \cdot w} & \varepsilon_{11} &= \ln\frac{h}{h_0} \\ \sigma_{22} &= \frac{1}{2}\sigma_{11} & \varepsilon_{22} &= 0 \\ \sigma_{33} &= 0 & \varepsilon_{33} &= -\varepsilon_{11} \end{aligned} \tag{1.35}$$

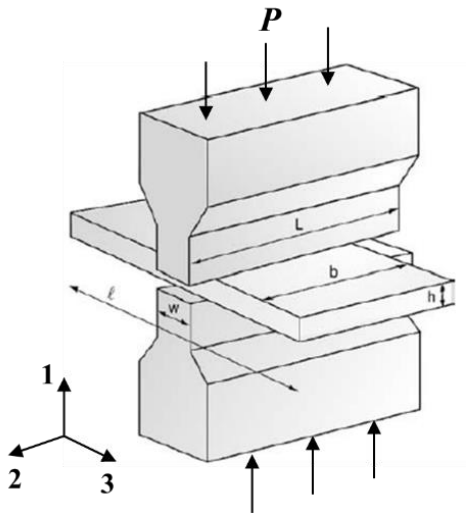

Fig. 1.9 Schematic diagram of plane strain compression test. [69]

There are some works about plane strain compression tests at different temperatures and strain rates.

Boldetti et al. [70] investigated the deformation of AA5182 under plane strain compression. The plane strain compression tests were performed at 400°C and a strain rate of $0.7s^{-1}$. The maximum strain at the gauge area reaches around 25%. Cheng et al. [71] studied the flow behavior of a commercial superalloy IN718 under plane strain compression test with a simulator thermo-mechanical device. The tests were carried out at the temperature range of 900 to 1050°C and the strain rate range of 10^{-3} to $10s^{-1}$. In order to determine the hot working characteristics of the Ti-6242 alloy at high temperature, the plane strain compression test was performed at the temperature of 1223 to 1370K and a strain rate of 0.01 to $10s^{-1}$ [72].

The heating of the plane strain compressions in the literatures above are all performed in a thermo-mechanical treatment simulator (like the simulator Gleeble 3800 [73]), which provide a heating chamber to heat the specimen before the test.

According to the review above, the plane strain compression test can be widely used in the study of thermo-mechanical behavior of metallic alloys. A high temperature (around 1000°C) can be reached for the plane strain compression test. However, One drawback of the plane strain compression test is that the free edges lead to an inhomogeneous strain field in this area and require extra analysis [74].

1.3.4 Hydraulic bulge test

For the bulge test, the central zone of circular plate is deformed under biaxial tensile state, as shown in Fig. 1.10. The hydraulic fluid, viscous materials or gas can be chosen as the pressure medium. The flow stress can be calculated with the following equations:

$$\begin{cases} R_d = \dfrac{\left[\left(d_c/2\right)+R_c\right]^2 + h_d^2 - 2R_c h_d}{2h_d} \\ t_d = t_0\left[\dfrac{1}{1+\left(2h_d/d_c\right)^2}\right] \\ \bar{\sigma} = \dfrac{pR_d}{2t_d} \\ \bar{\varepsilon} = \ln\left(\dfrac{t_d}{t_0}\right) \end{cases} \tag{1.36}$$

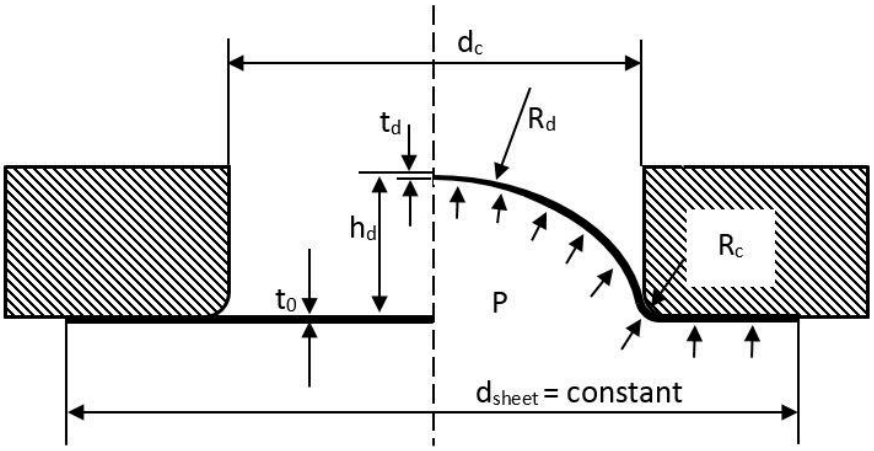

Fig. 1.10 Schematic of bulge test. [75]

Where p is the hydraulic pressure, R_d is the radius of dome, R_c is the radius of fillet of the cavity, d_c is the diameter of the cavity, t_d is the current thickness at the top of the dome, t_0 is the initial sheet thickness, and h_d is the height of dome.

Compared with the uniaxial test, bulge test is usually used to obtain the material behavior under balanced tensile path, especially for the equivalent stress and equivalent strain curves, which can reach up even two times of strain level than that obtained by uniaxial tensile test [76].

In order to make bulge test at high temperature, Kalkman et al. [77] have developed a bulge test setup (Fig. 1.11) which enables testing the mechanical behavior of metallic thin film samples between room temperature and at least 300°C. However, the strain rate with this setup is below $10^{-5}s^{-1}$. Mahabunphachai et al. [78] used the hydraulic bulge test to investigate the formability of AA5052 and AA6061 at different temperatures (room temperature, 100°C, 200°C, and 300°C) and strain rates (0.0013 to 0.013 s^{-1}). Liu et al. [79] determined the plastic hardening curves for AA7075 at elevated temperature with the hydraulic bulge test. The tests were performed from ambient temperature to 350°C. The strain rate reached in the test is around $0.00093s^{-1}$.

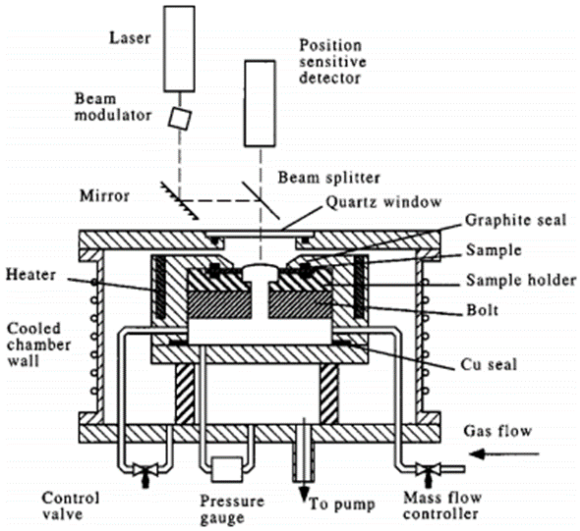

Fig. 1.11 Schematic cross section of the high temperature bulge test setup. [77]

Combined with the split Hopkinson pressure bar system, the bulge test can be performed at higher strain rates (up to $300s^{-1}$) in [80,81].

However, few works have been performed with the bulge test to characterize the mechanical behavior of sheet metal under different temperatures and intermediate or high strain rates. Main reasons are the complexity of the post-treatment stage of this out of-plane test which are due to non-homogeneous of both temperature and strain fields in the specimen, and friction between the sample and the die.

1.3.5 Conclusion

The conventional testing methods presented in this section are widely used to investigate the mechanical properties of the metallic materials. Nevertheless, these conventional tests also have some limitations: low level of strain achieved, heterogeneity of the test, difficulty to reproduce the true stress states of the material during the process, ..., which have been mentioned previously.

1.4 In-plane biaxial tensile test

According to the drawbacks of the conventional test mentioned in the previous section, the in-plane biaxial tensile testing technique has been proposed to characterize the mechanical behavior of sheet metal.

These characterizations, based on the in-plane biaxial test performed on cruciform specimen, mainly involve three aspects: (i) characterization of yield locus; (ii) identification of the hardening model for large strains; (iii) determination of Forming Limit Curve (FLC).

Stand-alone biaxial testing machines, with four independent actuators along two directions by which various linear and non-linear load paths can be realized, are shown in Fig. 1.12.

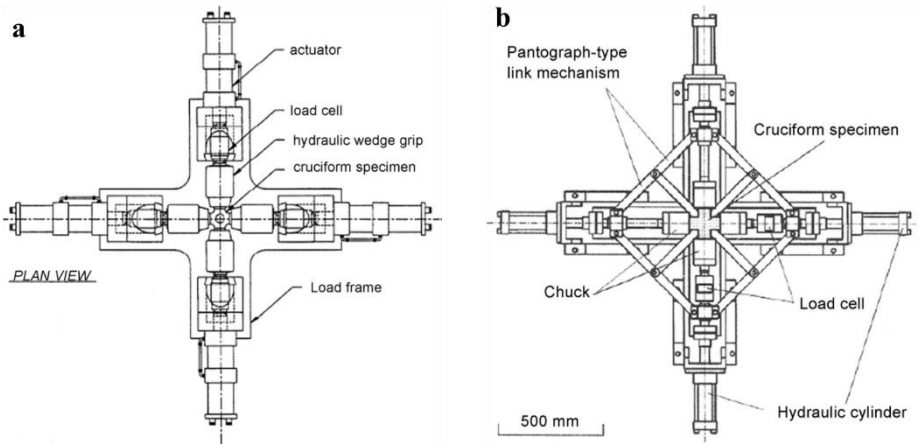

Fig. 1.12 Stand-alone biaxial testing machines: (a) Makinde 1992 [82]; (b) Kuwabara 1998 [83].

This kind of biaxial machines are more appropriated than link mechanism attachments used in a conventional uniaxial testing machine to convert uniaxial tensile or compressive force into two forces along two perpendicular directions of the cruciform specimen.

Despite the testing machine, the most important part is the design of the cruciform specimen [84]. The different goals of investigations require different shapes of specimen. Two main design prerequisites are proposed in [85]: (i) stress-strain homogeneity within the center section, enabling stress calculations with minimal deviations; (ii) ensuring that yield occurs in the test section, to avoid premature rupture in the arms. Three type of specimens have been proposed [86]: cut type with notch between two arms; thickness reduction at the center; strips and slots along each arm, as shown in Fig. 1.13. Most of the cruciform specimens in the researches up to date are using as one of these types or a combination of the different types.

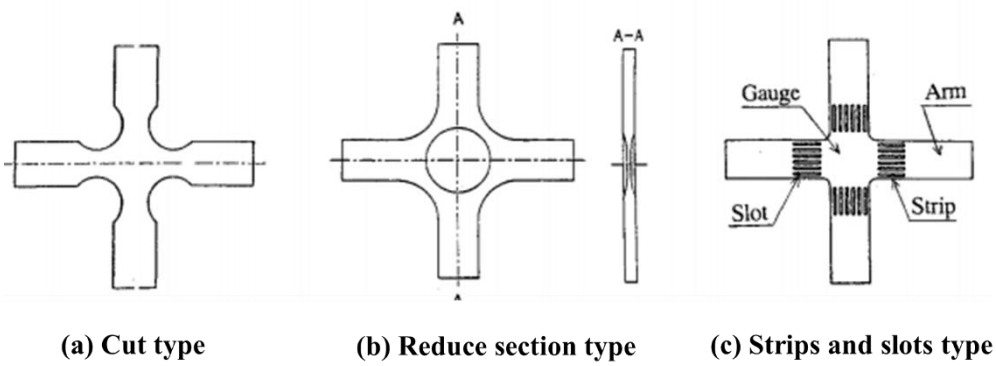

Fig. 1.13 Different type of cruciform specimen. [86]

The application of the in-plane biaxial test to the characterization of the mechanical behavior of sheet metal is presented in the following.

1.4.1 Application of in-plane biaxial tensile test

1.4.1.1 Characterization of yield locus

Kuwabara et al. [87] determined the yield surface for different kinds of cold-rolled steel sheet based on prescribing an abrupt strain path change. The study is performed on the proposed biaxial machine [83] and the shape of specimen with slots along each arm is shown in Fig. 1.14. The cruciform specimen are subjected to biaxial stretching with different tensile loading ratios (1:0, 4;1, 2:1, 4:3, 1:1, 3:4, 1:2, 1:4 and 0:1). Strain rates in the test were low: $(1.6-2.6)\times10^{-4}/s$. The measured yield locus and the directions of plastic strain rate vectors have been compared with the predictions by different yield criteria. It is worth notice that the maximum equivalent strain for this specimen was only 0.04 which is low.

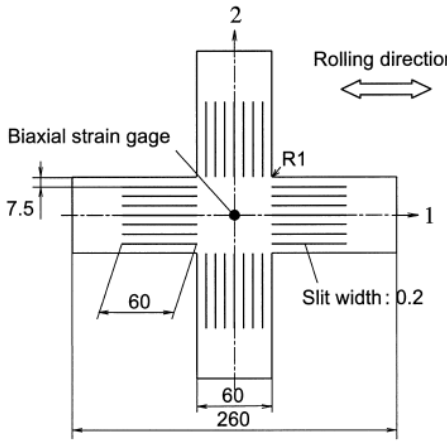

Fig. 1.14 Cruciform of specimen (Units are in mm) [87].

Naka et al. [88,89] investigated the temperature and strain rate effects on the yield locus for AA5083 with the cruciform biaxial tensile test for temperatures between 30 and 300°C and a strain rate of 10^{-5} to $10^{-2}s^{-1}$. The cruciform specimen with notches between two arms is shown in Fig. 1.15. The biaxial testing is performed at the temperature from 30 to 300°C at the strain rate of $10s^{-1}$. To achieve different stress ratio, the testing speed for each axis are defined as X:Y= (0:4), (1:4), (2:4), (3:4), (4:4), (4:3), (4:2), (4:1) and (4:0). The X and Y directions are parallel to the rolling direction and transverse direction respectively. The size of yield locus drastically decreased with increasing temperature. The author concluded that the yield loci and equi-plastic strain surfaces for AA5083 show remarkable temperature dependence; the yield functions of Barlat and Logan-Hosford are the best to describe the shape of the yield locus for this material.

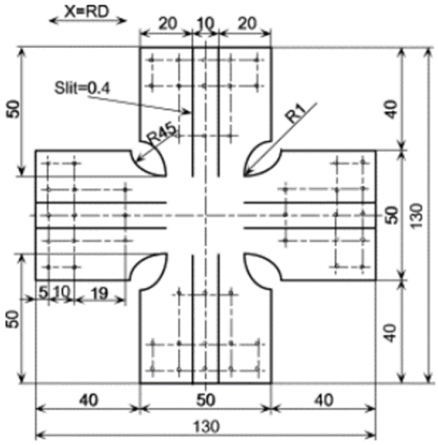

Fig. 1.15 cruciform specimen. [88]

Teaca et al. [90,91] has identified plastic anisotropy for ES steel and 1050A aluminum sheets by using heterogeneous biaxial tensile tests. The cruciform specimen is shown in Fig. 1.16. A two-step strategy of parameter identification is performed to determine the FMM yield model [48] for ES steel and 1050A aluminum sheets. The parameters of hardening law are determined by uniaxial tensile tests at a nominal strain rate of $3\times10^{-4}s^{-1}$. Then, the parameters of the FMM yield model are identified by minimizing the difference between experimental and simulated strain fields in biaxial tensile tests. The nominal average strain rate in the biaxial experiments is equal to $2\times10^{-4}s^{-1}$.

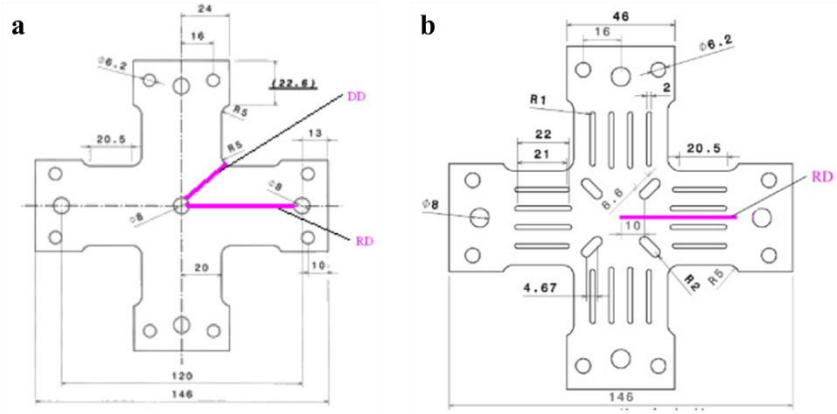

Fig. 1.16 (a) Cruciform specimen of UT/PST; (b) Cruciform specimen of UT/EBT. [90]

Zhang et al. [15] identified the Bron and Besson yield model for AA 5086 with a single biaxial tensile test at room temperature and quasi-static condition. The shape of cruciform specimen is shown in Fig. 1.17. The parameters of Bron and Besson yield model is obtained by minimizing the experimental and numerical simulation data of principal strains along a specified path in the central gauge of the specimen. The identified yield model is compared with the Hill 48 yield model which is identified with the conventional testing method (uniaxial tension, simple shear test and bulge test). The authors concluded that the Bron and Besson yield model has a better performance in the description of principal strains for AA5086, and a single biaxial tensile test is sufficient to obtain all the material parameters of a complex yield criterion.

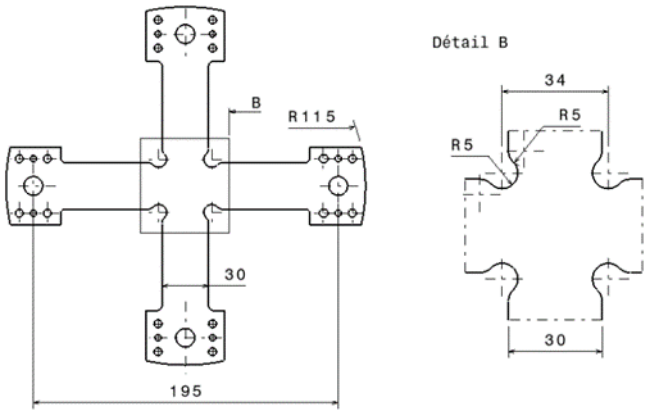

Fig. 1.17 Cruciform shape of specimen [15] .

1.4.1.2 Identification of hardening model

Gozzi et al. [92,93] investigated the plastic behavior of extra high strength steel under nonlinear strain paths in the biaxial tension. Two shapes of cruciform specimen have been designed for the biaxial tensile test, as shown in Fig. 1.18. With the smooth transition shape of the specimen, the stress concentration can be reduce on the arms, and three slots along each arm can make the deformation uniform. The maximum equivalent strain at the center zone is about 0.01, which is obtain by the strain gauge at the center of the specimen. The stress is calculated from the force divided by the modified cross section. A series of tests are carried out under two stage loading path: an initial proportional path; an unloading and a subsequent proportional reloading path in a new direction. From the results, it can be seen that the kinematic hardening model is better to predict the material under non-monotonic loading.

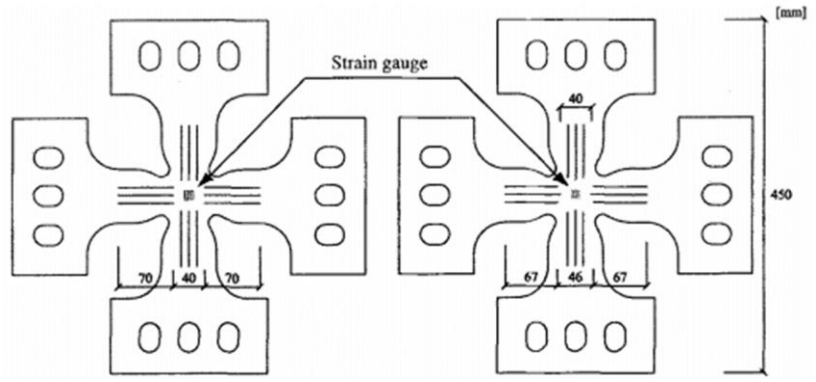

Fig. 1.18 Cruciform of the specimen for Gozzi. [93]

W. Liu et al. [94] identified the hardening behavior of AA5086 for large strain with the in-plane biaxial tensile test. In order to obtain the large strain, a dedicated shape of cruciform specimen with a thickness reduction at the center zone, slits along each arm and notches between two arms is proposed as shown in Fig. 1.19. With the numerical simulation for the dedicated shape of specimen, a strain concentration is observed in the center of specimen and the maximum equivalent plastic strain at the center point is up to 30% which is larger than the one from uniaxial tension (20%). The designed specimen is validated by a quasi-static equi-biaxial tensile test on AA5086. The strain in the central area of the specimen is measured by

Digital Image Correlation technique. The equivalent strain in the central zone of specimen reaches 30% as expected. The corresponding experimental forces along two arms and strains in the center point is used to identify the hardening behavior of material by inverse analyses. A modified type of Voce hardening law is combined with three yield criteria (Mises, Hill 48 and Bron and Besson). The identification results from different yield functions are compared with the experimental flow stress curve obtain from uniaxial tensile test (below 20%). The author concluded that the in-plane biaxial tensile test permits to identify the hardening behavior up to large strains with a dedicated cruciform specimen.

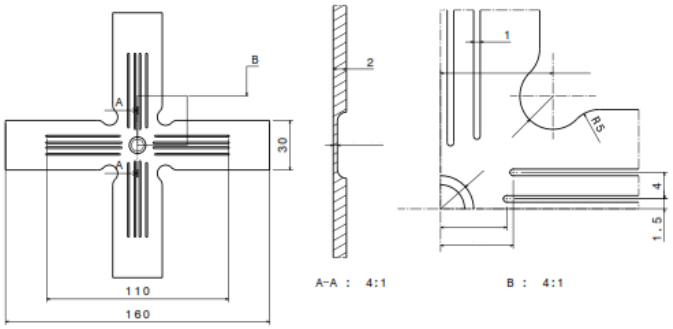

Fig. 1.19 Cruciform of specimen. [94]

1.4.1.3 Determination of forming limit curve

Xiao et al. [95] developed two shapes of cruciform specimen (Fig. 1.20) to investigate the forming limit of TA1 titanium alloy at three different temperatures (20, 400, and 600°C) and different stroke ratios of X:Y = 3:1, 3:2, 3:3, and 1:3 to cover the whole forming limit diagram. The tests are performed under quasi-static condition ($0.0025s^{-1}$). The shape of the specimen is validated with numerical simulation. The simulation show that, for the type-A specimen, the stress was concentrated at the border between the filleted corner and traditional straight surface, which resulted in a premature fracture in this region; for the type-B, the stress was concentrated at the center area of the arc surface. The forming limit curves obtained from the biaxial tension at different temperature are compared with the numerical simulation data and show a good agreement.

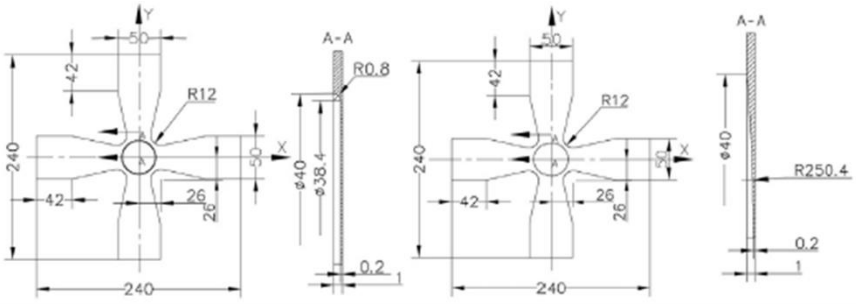

Fig. 1.20 Cruciform specimen with circular grooves. [95]

Zidane et al. [96] investigated the forming limit curve of AA5086 with in-plane biaxial

tensile test. A specific cruciform specimen, which includes a two-step thickness reduction at the center zone, is designed with the numerical simulation and validated in the biaxial tensile test for AA5086. The geometry of the specimen is shown in Fig. 1.21. Finally, the authors conclude that a single biaxial tensile test with the designed cruciform specimen is sufficient to characterize both the forming limit diagram and rheological behavior for the material. Based on this work, Song et al. [97] further investigated the forming limit curve at fracture (FLCF) for DP600 by optimizing the geometry of cruciform specimen (Fig. 1.22). With the FLCF obtained from the experiment, the fracture yield criteria is identified through numerical simulation and used to predict the FLCF for different strain path.

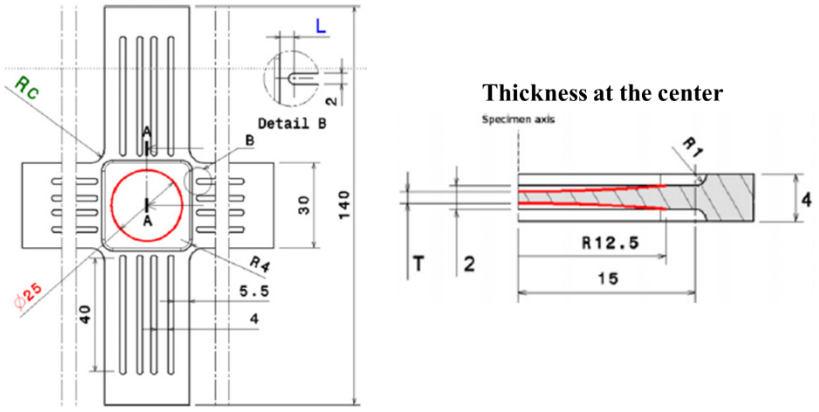

Fig. 1.21 Geometry of the cruciform specimen for Zidane. [96]

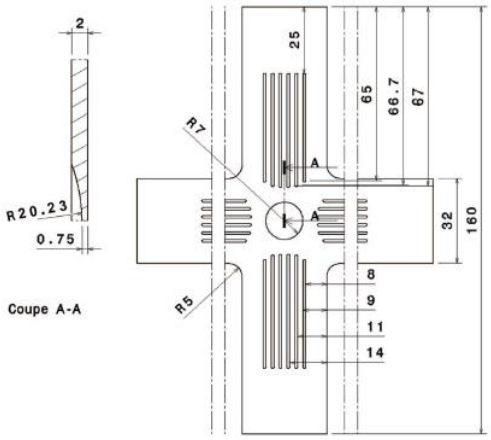

Fig. 1.22 Geometry of the cruciform specimen for Song. [97]

1.4.2 Heating device for biaxial testing machine

With the development of thermal sheet-forming technology, biaxial testing technologies using mature mechanical devices at ordinary temperatures must be validated for implementation at high temperatures. Thermal cruciform biaxial tensile systems have been developed greatly. With the help of apparatus used in high-temperature environments, many researchers have performed biaxial tensile testing of sheet metals at elevated temperatures [98].

Compared with ambient-temperature testing, biaxial tensile tests including temperature effects become more complex [99]. Specimens can be heated during the testing using laser

beams, heating guns or other methods [100].

Geiger et al. [101] designed an experimental setup to characterize the plastic yielding of sheet metal at elevated temperature with biaxial tension. A local heating was performed on the central zone of the cruciform specimen as shown in Fig. 1.23. A diode laser was elected to be the heating sources in the experiments because of several advantages compared to the other heating methods, the author claimed that:

1. Localization can be simply controlled by the size of laser spot (compared with conductive heating)
2. Integration of the laser source is not relevant since the laser beam can arbitrarily be manipulated with optical elements (compared with inductive heating).
3. Friction will not appear, because the laser is a contactless tool (compared with heating cartridge).
4. Power is abound (compared with infrared radiation).

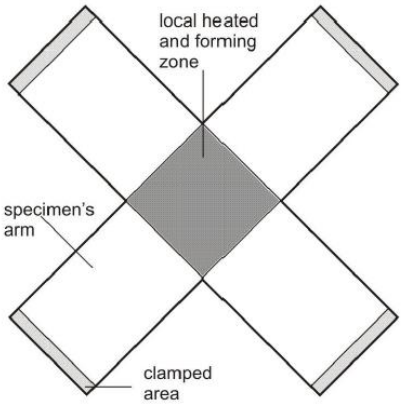

Fig. 1.23 Schematic design of the cruciform specimen. [101]

A scheme of the experimental setup is shown in Fig. 1.24 (a). Through a specially developed cylindrical optics, the horizontal integration of the laser source is beam-forming and leading into a vertical propagation with a mirror. A hollow construction of the punch (Fig. 1.24(b)) allows heating with the laser beam from bottom. Using the diode laser to heat the center section of a magnesium alloy specimen, a temperature of 250 °C is measured by pyrometer.

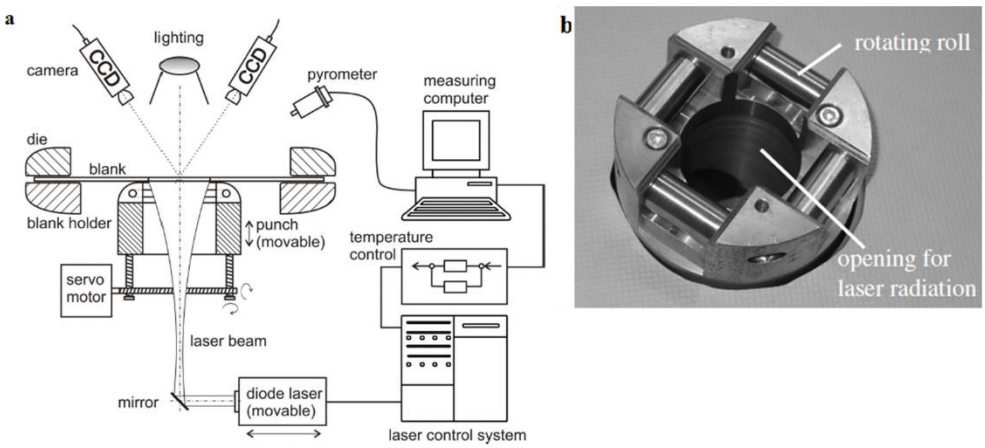

Fig. 1.24 (a) Experimental setup; (b) Special designed hollow punch. [101]

Abu-Farha et al. [102] evaluated quasi-static deformation behavior of AA5083, Mg AZ31B, and twinning induced plasticity (TWIP) steel at 300 °C under biaxial tension. The experiment device is shown in Fig. 1.25. High-temperature testing was facilitated by using a heat gun that capped a localized heating chamber surrounding the gauge area of the specimen. The maximum temperature of 350°C could be achieved within the specimen's gauge area. Two thermocouples were positioned inside the heating chamber for temperature measurement. The method used to heat the specimen center directly avoids damage to the test equipment parts such as the chuck, pull rod and related sensors.

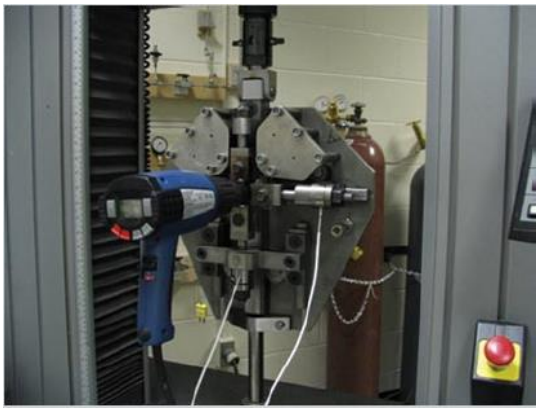

Fig. 1.25 Biaxial testing device and heating gun [102].

In order to meet the experimental temperature requirements for materials with high crystallization temperature, high-power equipment are used in some studies.

Kulawinski et al. [103] investigated the fatigue behavior of the forged nickel-base superalloy Waspaloy^{TM} at the temperature of 400°C and 650°C under uniaxial and biaxial tension with a constant strain rate of $10^{-3}s^{-1}$. For the biaxial testing, a servo-hydraulic biaxial planar tension–compression machine was adopted as shown in Fig. 1.26(a). In the test, the cruciform specimens were inductively heated by a cylindrical inductor coil which is placed in front of one side of the gauge area (Fig. 1.26(b)). The temperature was measured and controlled by a K-type thermocouple, and could reach 650 °C. Moreover, the specimen was instrumented with 13 thermocouples on the surface to measure the temperature field on the specimen (Fig. 1.28). Through the measurement, the temperature distribution at 650°C is given by a thermography image as shown in Fig. 1.28. A homogeneous, circular shape temperature field is observed in the gauge area, which is characteristic for the cylindrical inductor coil.

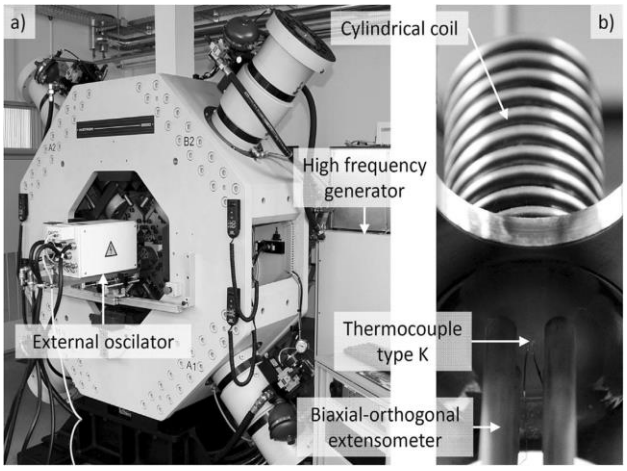

Fig. 1.26 (a) Servo-hydraulic biaxial-planar tension–compression machine with inductive heating device. (b) Arrangement of the applied extensometer and the thermocouple as well as the cylindrical induction coil at the cruciform specimen. [103]

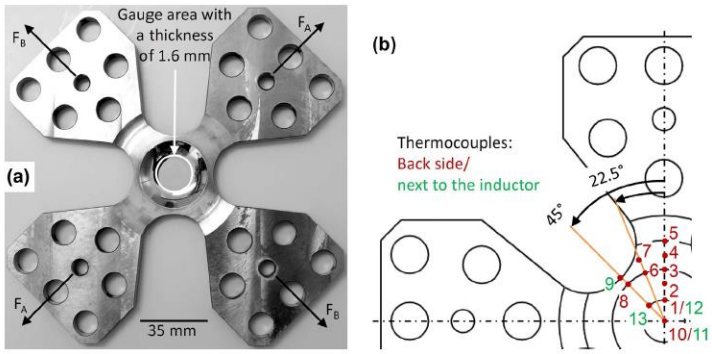

Fig. 1.27 (a) Cruciform specimen ;(b) Location of the K-type thermocouples. [103]

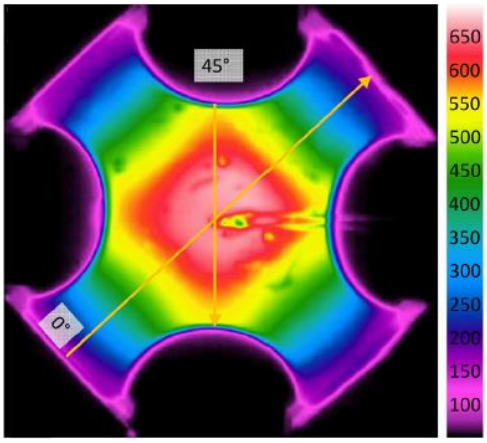

Fig. 1.28 Thermography image of the cruciform specimen taken at 650°C. [103]

Xiao et al. [104] studied the thermo-mechanical deformation behavior of a GH738 nickel-based superalloy at elevated temperatures under biaxial tension. The experiments were performed under three different temperatures (20, 300 and 500°C) and different tensile velocity ratios (0.02mm/s on each side; 0.03mm/s on the X-axis, and 0.02mm/s on the Y-axis). A heating device was developed and equipped with the biaxial tensile machine as shown in Fig. 1.29. The heating furnace maintained a constant temperature between room temperature and 800°C,

which was guaranteed by four communicating temperature zones that could be separately controlled. The heating wires were arranged in the walls and bottom of the heating furnace. Each temperature control zone controlled the heating wires of a furnace wall. Ceramic fiberboards were installed in the inner walls, bottom, and top of the heating furnace to maintain the temperature and insulate the heat to guarantee peripheral equipment temperature at 40°C or below.

A disadvantage of this equipment is that strokes are sacrificed and the dimensions of the tensile specimen have to be shorten in order to prevent the excessive deflection generated from the gravity of the clamping chuck and tensile bar, because of the inability to install linear bearings in the heating furnace.

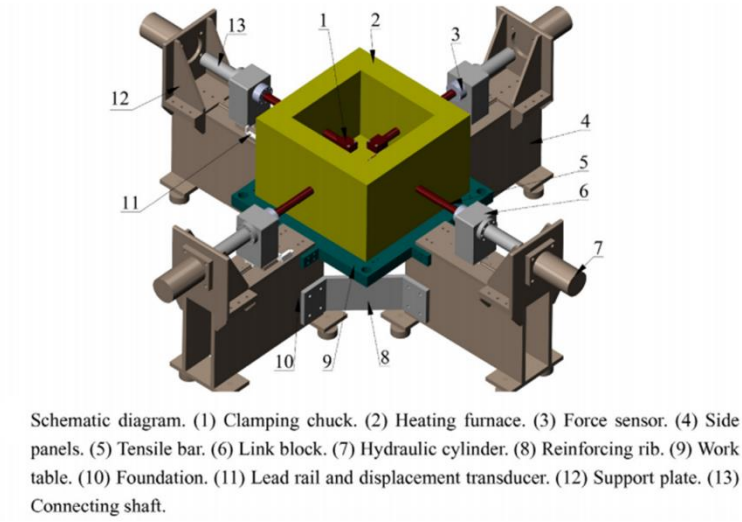

Schematic diagram. (1) Clamping chuck. (2) Heating furnace. (3) Force sensor. (4) Side panels. (5) Tensile bar. (6) Link block. (7) Hydraulic cylinder. (8) Reinforcing rib. (9) Work table. (10) Foundation. (11) Lead rail and displacement transducer. (12) Support plate. (13) Connecting shaft.

Fig. 1.29 Thermal plane biaxial tensile machine. [104]

Shao et al. [105] designed a novel biaxial testing system in a Gleeble testing machine to generate temperature forming limits of sheet metals. The heating system is based on the Joule effect, four clamping regions on the four arms of the cruciform specimen are contacted tightly with stainless steel top plates, which are electrodes for resistance heating. Three types of heating and cooling strategies for the cruciform specimen are proposed as shown in Fig. 1.30. For the Type-1 (Fig. 1.30(a)), one arm on the specimen is connect to the positive electrode and the opposite one to the negative electrode and two nozzles are used for cooling. The temperature on the specimen remains low and the distribution is not uniform on the specimen, since there is no electrical current flow in the other two arms of the specimen. For the Type-2 (Fig. 1.30(b)), two adjacent arms are attached to positive electrodes and the other two to negative electrodes. The electrical current can goes through the entire specimen to heat it and four nozzles are used for cooling. For the Type-3 (Fig. 1.30(c)), two opposite arms are attached to positive electrodes and the other two to negative one and the same cooling method as Type-2 is used. The target temperature is of 535°C and the heating system was tested for an AA6082 sheet. The location of thermocouples and the measurement temperature on the specimens are shown in Fig. 1.31. After, a further investigation for the heating system was performed by FE numerical simulations to obtain the temperature fields on specimens for the three types of strategies. Base on the above

analysis, the Type-2 is the most acceptable one since fractures could occur in the central region by consideration of temperature distribution on a specimen. Also, the biaxial tensile test were perform on this experimental system to investigate the forming limit curves for AA6082 at temperatures of 400 and 500°C and strain rate of 0.1/s. Finally, the author concluded that, this method can be used to determine the hot formability of many sheet metals with the maximum temperature up to 1000°C.

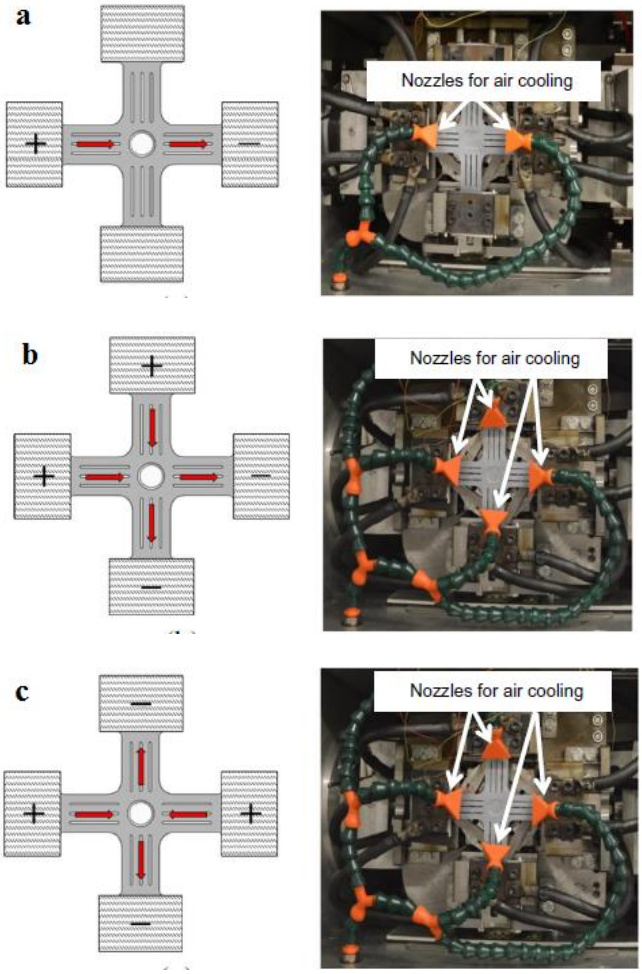

Fig. 1.30 Three strategies of specimen heating and cooling: (a) Type-1; (b) Type-2; (c) Type-3 (Arrows on specimens represent polarity of electrical potential). [105]

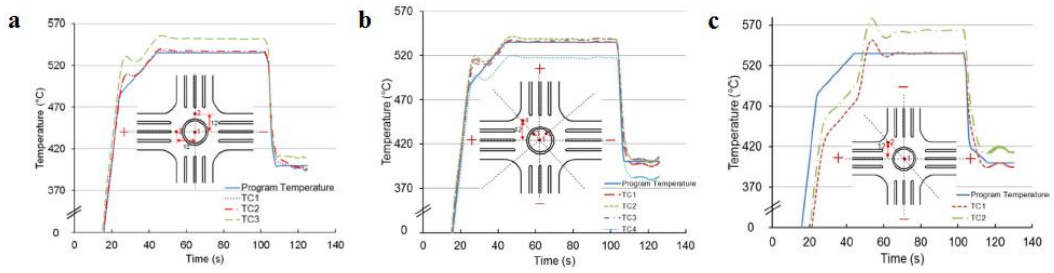

Fig. 1.31 Temperature profile and distribution for the three strategies: (a) Type-1; (b) Type-2; (c) Type-3; (Number dots on specimens are thermocouples location). [105] you either enlarge the figure or you remove it, we don't see the location of the thermocouples…

1.4.3 Conclusion

In the literatures above, the in-plane biaxial can be very efficient for the identification of yield locus, hardening model and determination of forming limit curves for different materials. By changing the deformation paths, the yield models and FLCs can be easily achieved with this test.

In order to study the temperature influence on the mechanical behavior of the materials, several heating devices have been proposed for the in-plane biaxial test. It can be seen that the cylindrical inductor in [103] (650°C) and the heating furnace (800°C) in [106] are more efficient to obtain high temperatures for the specimen than the other methods. Compared with the other heating methods, the temperature can be considered as constant and homogeneous in the specimen before the test.

It can be concluded that, for the in-plane biaxial tensile test at various temperatures, a heating system with insulated box is the best choice to equip the available biaxial tensile device.

1.5 Conclusion

In this chapter, a brief review of different constitutive models and experimental methods used for the characterization of mechanical behavior of metallic alloys have been presented.

In the FE simulation of sheet metal forming processes, an appropriate constitutive model is necessary to obtain a good prediction of the material behavior. To improve the accuracy of this constitutive model, temperature and strain rate sensitivities are critical issues to be considered. In the literature, influence of both temperature and strain rate on the material mechanical behavior is mainly focused on the flow stress. However, for the effect of temperature and strain-rate on the anisotropic behavior and the evolution of the yield surface, further explorations are still needed.

Many experimental methods have been developed for the material characterization. Compared with conventional methods, the in-plane biaxial tensile is interesting since it allows to reach large plastic strains under different strain paths and biaxial loadings closed to the ones encountered in forming processes

In the following work, in chapter 2, uniaxial tensile tests are performed in a temperature range from ambient to 200°C and strain rates ranging from 2.10^{-3} to $4s^{-1}$ for an aluminium alloy AA6061. Based on this experimental database, a temperature and strain rate dependent hardening model is chosen and calibrated. In chapter 3, equi-biaxial tensile tests are carried out for the same conditions of temperature and strain rate. Through an inverse analysis based on a FE model of the biaxial tensile test, the temperature and strain rate dependent hardening model, selected in chapter 2, is calibrated from the experimental biaxial tensile test database. Finally, in chapter 4, the identified hardening model will be coupled with the complex anisotropic yield criterion of Bron and Besson to discuss the temperature and strain rate influences on the anisotropic behavior of the material AA6061.

Chapter 2 Experimental investigation of hardening behavior of AA6061 under different temperatures and strain rates

2.1 Introduction

The Aluminum alloys 6xxx are widely used in the industry because of their high extrudability, good formability and excellent corrosion resistance [107]. The AA6061 is a typical alloy of this series which is used for the production of structural components in automotive and aircraft industry [108]. In the marine industry, this alloy is used to produce flat-bottomed watercraft due to its light weight, high strength, and good corrosion resistance even exposed to salt water [109]. Nevertheless, the aluminum alloy sheets generally exhibit low formability and large spring back at room temperature compare to the traditional steel sheets. Then the forming of aluminum alloy sheets at elevated temperatures is supposed to be one of the effective solutions to improve the formability and reduce spring back effects.

There have been various studies about temperature and strain rate influence on the mechanical properties of aluminum alloy 6xxx. For example, Fan et al. [110] investigated the dynamic mechanical behavior of AA6061 at different temperatures (293K to 673K) and different strain rates (10^{-3} to $10^{4}s^{-1}$) with the split Hopkinson pressure bar test. The result indicates a significant temperature effect on the strain hardening of this material, while the strain rate effect is more obvious at relatively high temperature (573K to 673K) than low temperature. Mohamed et al. [111] investigated the deformation and damage of AA6082 in hot stamping and cold die quenching. A set of viscoplastic damage constitutive equations were developed and calibrated for AA6082 over a range of strain rates (0.1 to $10s^{-1}$) and temperature (450 to 525°C) and used in the simulations of panel part manufacture. Chen et al. [58] evaluated the effect of temperature (ambient to 380°C) and strain rate (0.0005 to $0.05s^{-1}$) on the formability of AA6061-T6. The experimental results show that the forming limits of this material increased with the increasing temperature and the decreasing forming speed.

Therefore, the investigation of mechanical behavior for Aluminum alloy 6xxx at different temperatures and strain rates is necessary if we want to make reliable the optimization of forming processes for such conditions. In this chapter, a first study is proposed based on uniaxial tensile tests. The anisotropy behavior of AA6061 is evaluated thanks to tests along rolling, diagonal and transversal direction. Then, uniaxial tensile tests are performed along rolling direction in the strain rate range from $0.002s^{-1}$ to $4s^{-1}$ and for a range of temperature from ambient to $200^{\circ}C$. Several hardening models introduced in Chapter 1 are selected to identify the material hardening behavior under the tested temperatures and strain rates. The parameters are identified and the predicted flow stresses for all the hardening models are compared to experimental results and discussed.

2.2 Uniaxial tests of AA6061

2.2.1 Material

The material used in this work is AA6061-O. The chemical components for this material are shown in Table 2.1.

Table 2.1 Chemical components of AA6061-O in weight percent. [112]

Component	Wt. %	Component	Wt. %	Component	Wt. %
Al	95.8-98.6	**Mg**	0.8-1.2	**Si**	0.4-0.8
Cr	0.04-0.35	**Mn**	Max 0.15	**Ti**	Max 0.15
Cu	0.15-0.4	**Other, each**	Max 0.5	**Zn**	Max 0.25
Fe	Max 0.7	**Other, total**	Max 0.5		

2.2.2 Experiment setup

In this study, the conventional uniaxial tensile test was preliminary adopted to investigate the mechanical behavior of AA6061 at various temperatures and strain rates.

The specimen considered has a constant cross section with the following initial dimensions: gauge length (L_0) of 50mm, thickness (t_0) of 2 mm and a width (W_0) of 10 mm as shown in Fig. 2.1.

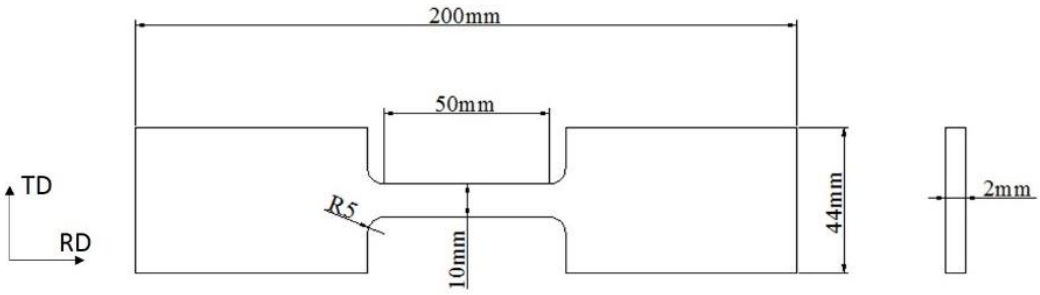

Fig. 2.1 Dimension of uniaxial tensile specimen.

The servo-hydraulic tensile machine equipped with a heating system was adopted in the test as shown in Fig. 2.2 (a). In order to ensure a constant and homogeneous temperature of the specimen at the beginning of the test, the specimen and the lower and upper grip devices are placed inside an insulated box (Fig. 2.2 (b)).

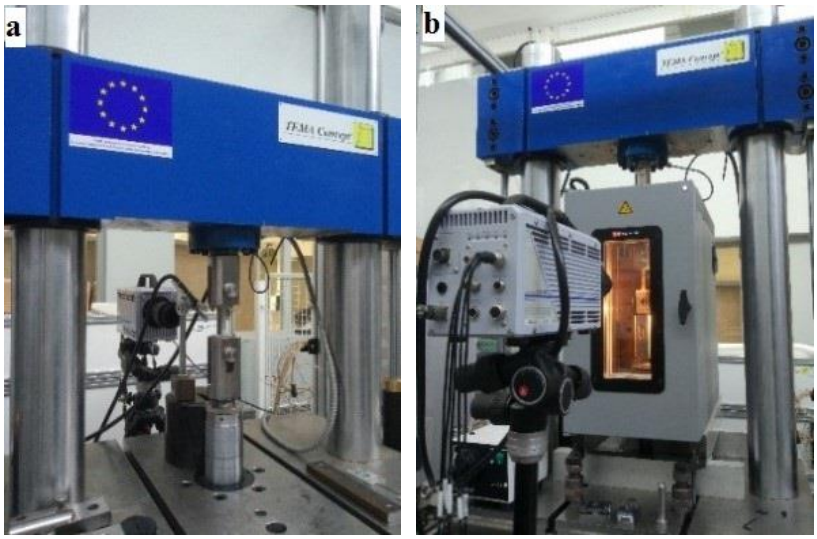

Fig. 2.2 (a) Servo-hydraulic tensile testing machine; (b) Insulated box.

The deformation of the specimen is filmed with a high speed camera (Photron FASTCAM-APX RS), through the insulated box door equipped with an optical quality window. Forces are measured by a strain gauge sensor mounted on the upper fixed crosshead. Main parameters of the video and load measurement systems are presented in Table 2.2.

Table 2.2 Main characteristics of acquisition.

Test velocity (mm/s)	Camera			Load sensor acquisition rate (Hz)
	Image resolution (pixel)	Acquisition rate (fps)	Shutter speed (s)	
0.1	256×960	50	1/1500	10
10	256×960	500	1/2000	1000
200	256×960	5000	1/15000	10000

The DIC (Digital image correlation) method is adopted to measure the deformation of the specimen during the tests. The sequence of images obtained from the camera is analyzed with the commercial software GOM Correlate 2017. Fig. 2.3 shows the analysis area on the surface of the specimen, within a dimension of 30mm along x and 10mm along y. With a facet size of 32 pixels and a point distance of 16 pixels, deformations are evaluated for 234 points for each specimen. In the following section, an average of both ε_{xx} and ε_{yy} is calculated with all the analyzed points for a given time. The reference image for the calculation of the strain field is the initial image.

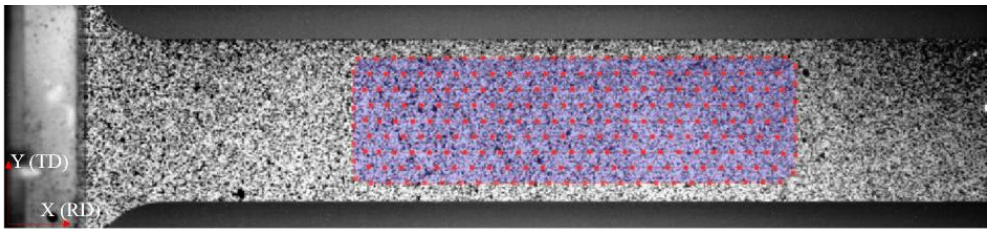

Fig. 2.3 Analyzed area of uniaxial tensile specimen.

The initial strain rate $\dot{\varepsilon}_{xx}$, true stress σ_{xx} during the tests can be calculated with Eq. 2.1:

$$\begin{cases} \dot{\varepsilon}_{xx} = v/L_0 \\ \sigma_{xx} = F \cdot (1+\varepsilon_{xx})/S_0 \end{cases} \tag{2.1}$$

where *v* is the tensile velocity, $S_0 = t_0 \cdot W_0$ is the initial cross section of the gauge area.

2.2.3 Anisotropy behavior of AA6061

Firstly, uniaxial tensile tests were carried out along $\theta = 0^\circ, 45^\circ, 90^\circ$ according to the rolling direction at ambient and quasi-static state (0.1mm/s) to investigate the anisotropic behavior of AA6061. Single test for each direction, respectively. The Young's modulus can be obtained from the stress-strain curve before plastic deformation takes place (longitudinal stress between 40 and 110 MPa). The true stress along the longitudinal direction is calculated with the Eq. 2.1, as presented above. The Young's modulus calculated for the three directions are

shown in Table 2.3. According to these values, the effect of orientation is not significant.

Table 2.3 Young's modulus values.

Direction	0°	45°	90°
E (MPa)	63240	62150	63884

Hence, the Young's modulus used in the following work is the value along the rolling direction at ambient temperature: *E*=63240 MPa. We will consider that the Young's modulus is independent on temperature for the studied range.

Fig. 2.4 gives the true stress-strain curves along three different directions in the test. . The true stress along $\theta = 90°$ is about 5MPa and 8MPa higher than the 0° and 45° directions respectively. While the true stress along 0° and 45° directions are rather close.

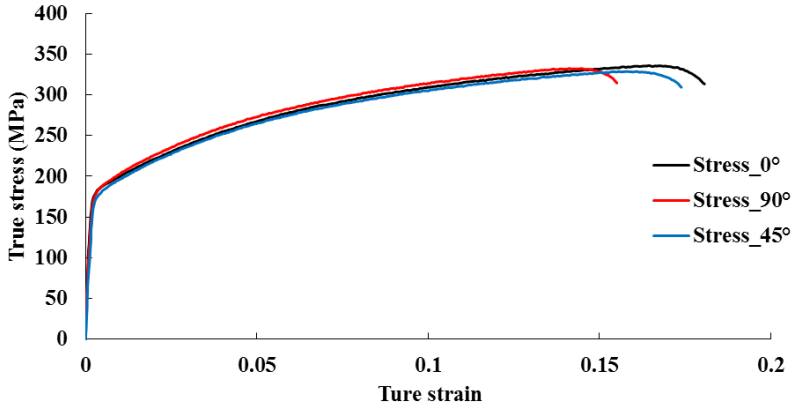

Fig. 2.4 True stress-strain curves along the three directions.

The plastic anisotropy coefficient (r_θ) is expressed by the ratio of width plastic strain rate ($\dot{\varepsilon}_{yy}^{p}$) to normal plastic strain rate ($\dot{\varepsilon}_{zz}^{p}$):

$$r_\theta = \frac{\dot{\varepsilon}_{yy}^{p}}{\dot{\varepsilon}_{zz}^{p}} \tag{2.2}$$

The assumption of the incompressibility of the material is assumed during the deformation: $\varepsilon_{xx}^{p} + \varepsilon_{yy}^{p} + \varepsilon_{zz}^{p} = 0$.

ε_{xx}^{p}, ε_{yy}^{p}, ε_{zz}^{p} are the plastic strains along longitudinal, width and normal directions of the uniaxial tensile specimen respectively which can be calculated as follows:

$$\begin{aligned} \varepsilon_{xx}^{p} &= \varepsilon_{xx} - \frac{\sigma_{xx}}{E} \\ \varepsilon_{yy}^{p} &= \varepsilon_{yy} + \upsilon \cdot \frac{\sigma_{xx}}{E} \end{aligned} \tag{2.3}$$

υ stands for Poisson's ratio. ε_{xx}, ε_{yy} are the strain components along longitudinal and width directions, which is obtained from DIC measurement.

The plastic anisotropy coefficient (r_θ) can be obtained from the evolution of width plastic strain to the thickness plastic strain in the equivalent plastic strain range of [0.02, 0.08]; [0.08, 0.14] and [0.02, 0.14] along three directions, and the *r*-values at different plastic ranges are given in Table 2.4 and presented in Fig. 2.5. The *r*-values trend to decrease with the equivalent plastic strain. The values obtained from the range 0.08 to 0.14 are nearly 25% lower than the ones obtained from 0.02 to 0.08. The *r*-value in 45° orientation is higher than 0° and 90° orientations to the rolling condition. This indicates the drawability is good in 45° orientation to the rolling direction for this material.

Table 2.4 r-values calculated at different plastic strain ranges.

$\bar{\varepsilon}^p$	r_0	r_{45}	r_{90}
0.02 to 0.08	0.3879	0.504	0.3704
0.08 to 0.14	0.2708	0.437	0.2259
0.02 to 0.14	0.3314	0.4532	0.311

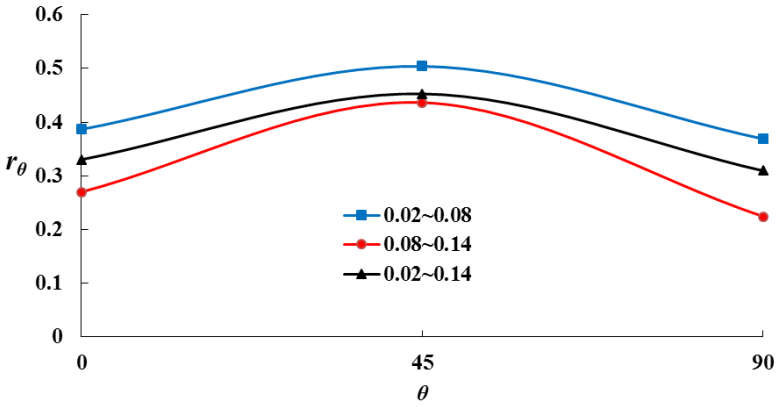

Fig. 2.5 r-value obtained for different plastic strain ranges.

2.2.4 Uniaxial tensile at different temperatures and strain rates

Uniaxial tensile (UT) tests are carried out at different temperatures (20, 150 and 200 °C) and with different constant tensile speeds: 0.1, 10 and 200 mm/s corresponding to an initial strain rate of respectively 0.002, 0.2 and 4 s^{-1} (Eq.2.1). Test results obtained from UT tests are performed along the sheet rolling direction.

With the displacement calculated from the velocities of the different tests, the force-displacement curves for different temperatures and strain rates are given in Fig. 2.6. For the different tensile velocities, the maximum force decreases with the increase of temperature.

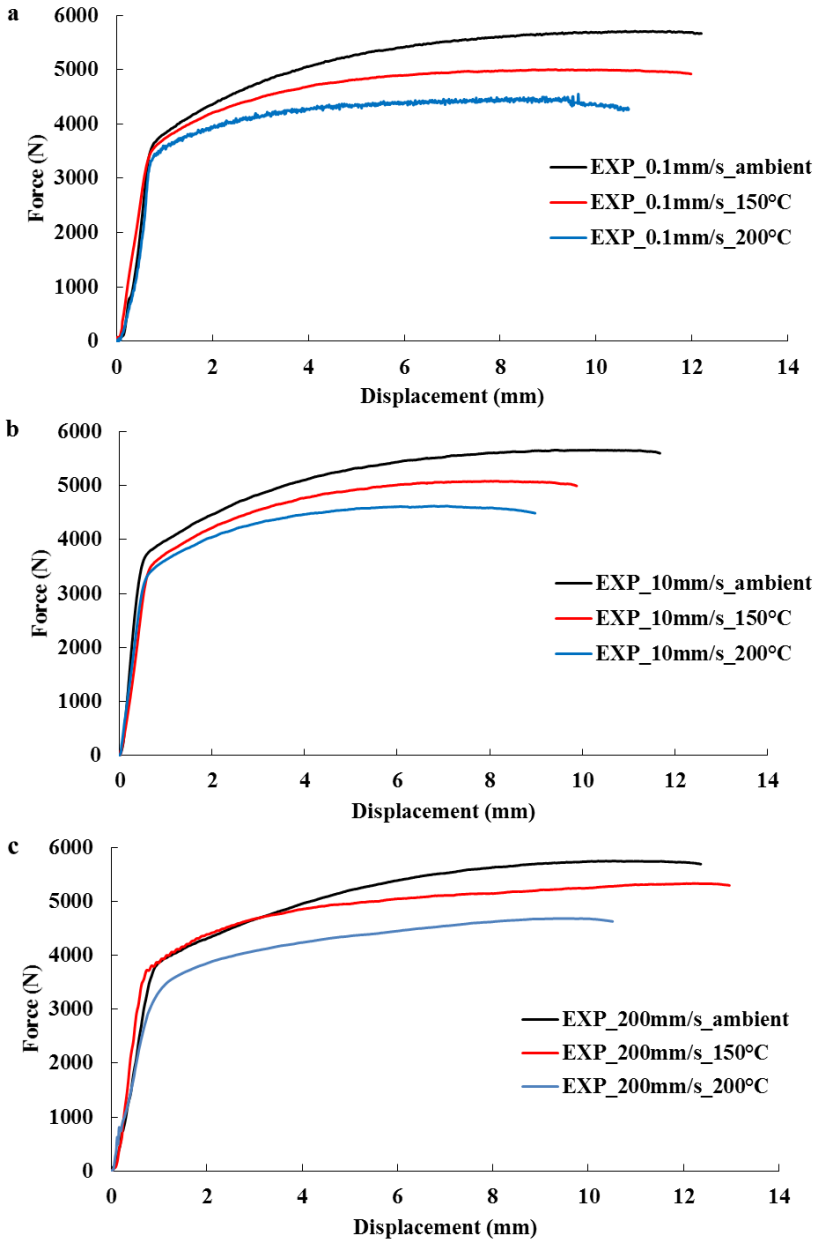

Fig. 2.6 Force versus displacement curves at different temperatures for each tensile speed.

The true stress and strain curves at different tensile speeds and temperatures are determined and plotted as shown in Fig. 2.7 and Fig. 2.8.

The strain rate influence on the flow stress is presented in Fig. 2.7. A slight positive strain rate influence on the flow stresses at ambient temperature can be observed. At 150°C, the flow stresses for the tensile velocities of 0.1mm/s and 10mm/s are almost the same, while the flow stress for 200 mm/s is 20MPa higher than for the other conditions, for an equivalent strain of 18%. A significant strain rate influence is showed at 200°C, the flow stress increases with the temperature. In addition, the elongation at rupture is significantly decreased with the increase of tensile velocity at 200°C (Fig. 2.7c). Indicating a high elongation can be obtained at low strain rate, because this material have intrinsically high strain rate sensitivity, especially at elevated temperature [113,114].

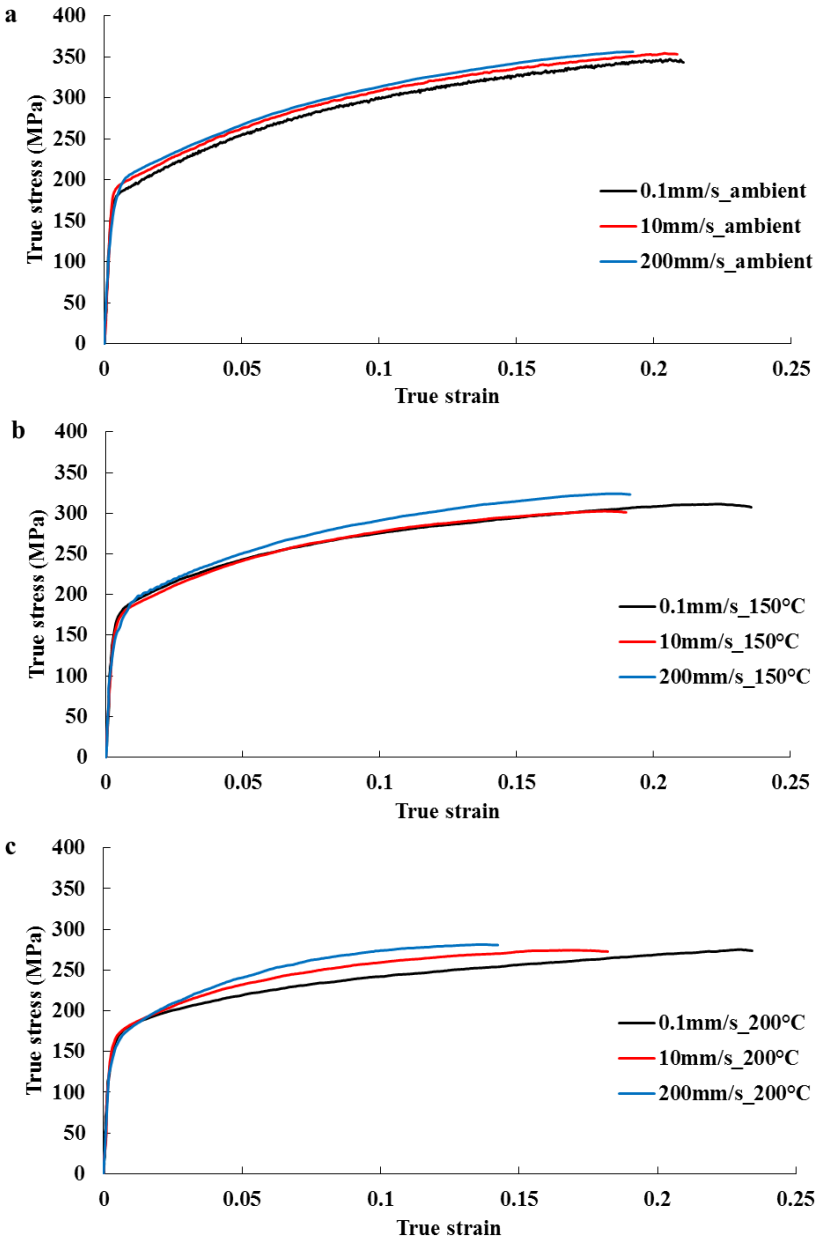

Fig. 2.7 Strain rate influence on the flow stress at different temperatures.

The temperature influence on the flow stress is presented in Fig 2.8. For a given tensile velocity, the temperature has a negative influence on the flow stress. The flow stress curves increase monotonically with the evolution of strain at the temperature below 150°C. When the temperature is 200°C, the flow stress curves of 10mm/s and 200mm/s show a saturated state with increasing strain, as shown in Fig 2.8(b) and 2.8(c). The flow stress temperature sensitivity is more pronounced at low tensile speed than at high tensile speed. It can be explained by the strain rate compensation to the flow stress at high temperature.

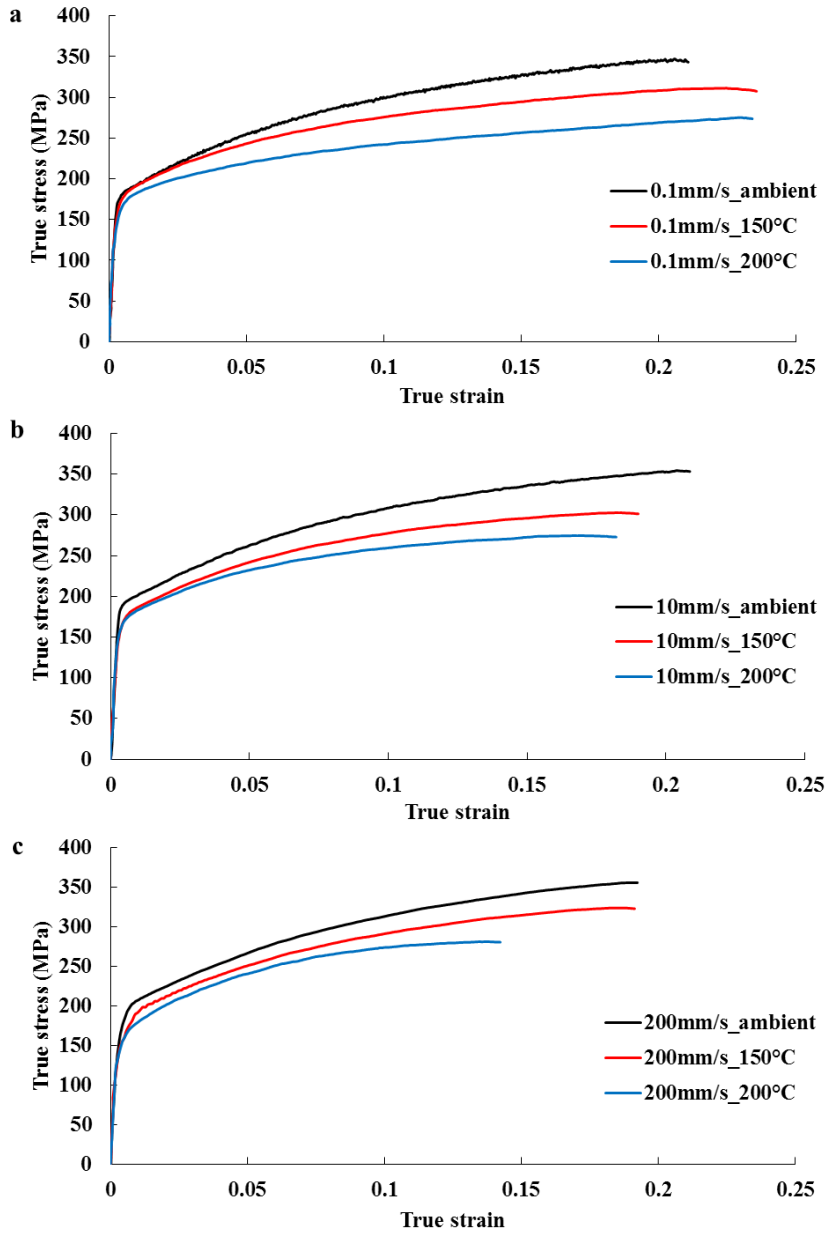

Fig. 2.8 Temperature influence on the flow stress at different tensile speeds.

It can be also seen that, for a given temperature, this material has a better ductility for low strain rates (Fig. 2.7). And for the same tensile velocity, the ductility is reduced with the increase of temperature (Fig. 2.8).

2.3 Calibration method for different hardening models

The analytical method and numerical method by inverse analysis are two commonly used methods for the calibration of hardening models. The procedure of calibration consists in minimizing the cost function between experimental data and the result obtained from analytical models or numerical models.

In the uniaxial tensile tests, the deformation in the gauge section of the specimen is supposed to be homogeneous, then the values of equivalent stress $\bar{\sigma}^{\exp}$ and strain $\bar{\varepsilon}^{\exp}$ can be calculated from the experimental data. Also, with a set of parameter values, the analytical

stress $\bar{\sigma}^{cal}$ can be calculated through the analytical model for a given strain value. The cost function δ, which means the absolute error can be expressed as follows:

$$\delta = \frac{\sum_{i=1}^{N} \left| \left(\bar{\sigma}_i^{\exp} - \bar{\sigma}_i^{cal} \right) / \bar{\sigma}_i^{\exp} \right|}{N} \tag{2.4}$$

$\bar{\sigma}_i^{\exp}$ and $\bar{\sigma}_i^{cal}$ are the stresses obtained by experiment and calculated from analytical model at the i^{th} increment respectively. N is the number of strain measurement points from experiment. In this method, the best parameters can be achieved by minimizing the cost function E.

The advantage of this method is that the time consumption is relatively small, but the temperature and strain rate are considered as constants during the tests.

2.4 Hardening models

In the literature, FCC structures, including aluminum alloys, exhibit large strain hardening due to the amount of dislocation interactions with increasing strain [39]. The strain hardening tends to be highly temperature and strain rate dependent [34].

Chu et al. [27] investigated the hardening behavior of AA5086 in a range of temperatures (ambient to 200°C) and strain rates (0.01 to $1s^{-1}$) with different kinds of hardening models, which included the physical-based Zerilli-Armstrong (ZA) mode and phenomenological models such as Ludwick and Voce model.

Compared to the physical-based models, the phenomenological models have fewer parameters and are easier to integrate in commercial numerical simulation software. The Ludwick and Voce hardening model which have been proposed in [27] are selected in this work to predict the hardening behavior of AA6061 at different temperatures and tensile speeds.

2.4.1 Ludwick model

Generally, the Ludwick model incorporates the strain rate influence by means of multiplicative formulation as shown in Eq. 2.5. The parameters *K*, *n* and *m* can be identified under different temperatures and strain rates, respectively. The evolution of these parameters with temperature permits to postulate a temperature function for each rheological parameter. In the work of Chu [27], the parameters are expressed as $K(T) = K_1 - K_2 T$, $n(T) = n_1 - n_2 T$, and $m(T) = m_0 e^{m_1 T}$. The final Ludwick model incorporating temperature and strain rate influence has been presented in Eq. 1.34 and given as Eq. 2.6 here.

$$\bar{\sigma} = \sigma_0 + k \bar{\varepsilon}_p^{\,n} \dot{\varepsilon}^{m} \tag{2.5}$$

$$\bar{\sigma} = \sigma_0(T) + (K_1 - K_2 T) \bar{\varepsilon}_p^{\,(n_0 - n_1 T)} \dot{\bar{\varepsilon}}_p^{\,m_0 \exp(m_1 T)} \tag{2.6}$$

In Eq. 2.6, K_1, K_2, n_0, n_1, m_0 and m_1 are the parameters which should be identified. In [27], the Ludwick model describes well the flow stress for AA5086 for low strain levels, while an overestimation is observed for high strains. This is caused by the monotonic strain hardening

character of the power law type.

2.4.2 Voce models

The Voce-type models are commonly used to describe the mechanical behaviors of aluminum alloys due to their saturation character at high strains. Three types of Voce model were presented as follows.

- ***V*₁ model.**

The original formula of V_1 model is shown in Eq. 2.7. The parameters C_1, C_2 and m are expressed through an exponential term. The final formulation of V_1 model shown in Eq. 1.35 and written as Eq. 2.8 here.

$$\bar{\sigma} = \sigma_0 + C_1\sqrt{1-\exp\left(-C_2\bar{\varepsilon}_p\right)}\dot{\varepsilon}^m \tag{2.7}$$

$$\bar{\sigma}=\sigma_0\left(T\right)+K_1\exp\left(-K_2T\right)\sqrt{1-\exp\left[-K_3\exp\left(K_4T\right)\bar{\varepsilon}_p\right]}\dot{\bar{\varepsilon}}_p^{m_0\exp\left(m_1T\right)} \tag{2.8}$$

- ***V*₂ model.**

Aretz et al. [115] have introduced a Voce-type model to describe the strain hardening behavior of AA5182-O (Eq. 2.9). The final V_2 model is given by Eq. 2.10.

$$\bar{\sigma}=\sigma_0+C_1\left(1-\exp\left(-C_2\bar{\varepsilon}_p\right)\right)\dot{\varepsilon}^m \tag{2.9}$$

$$\bar{\sigma}=\sigma_0\left(T\right)+\left(K_1-K_2T\right)\left(1-\exp\left(-K_3\exp\left(K_4T\right)\bar{\varepsilon}_p\right)\right)\dot{\bar{\varepsilon}}_p^{m_0\exp\left(m_1T\right)} \tag{2.10}$$

- ***V*₃ model.**

Based on the V_2 model, the V_3 model includes an additional power law strain term $\bar{\varepsilon}_p^{C_3}$, as shown in Eq.2.11. The final V_3 model is given by Eq.2.12.

$$\bar{\sigma}=\sigma_0+C_1\left(1-\exp\left(-C_2\bar{\varepsilon}_p^{C_3}\right)\right)\dot{\varepsilon}^m \tag{2.11}$$

$$\bar{\sigma}=\sigma_0\left(T\right)+\left(K_1-K_2T\right)\left(1-\exp\left(-K_3\exp\left(K_4T\right)\bar{\varepsilon}_p^{n}\right)\right)\dot{\bar{\varepsilon}}_p^{m_0\exp\left(m_1T\right)} \tag{2.12}$$

Where K_i, n_i, and m_i are parameters to be identified for the three Voce-type models.

The calibration of the aforementioned hardening laws for AA6061 at different temperatures and strain rates under uniaxial tension is performed in the following section.

2.5 Identification of rheological parameters for different hardening models

2.5.1 Initial yield stresses of AA6061

Zhang et al. [116] proposed an analytical method to determine the initial yield stress by

extrapolating a mathematical model that describes the uniaxial tensile stress along the rolling direction under small strain conditions. If the hardening is described by a Voce model (Eq.2.13), it can be approximated at the first order Taylor expansion (Eq.2.14) to describe the flow stress for a small plastic strain.

$$\sigma_0 = \sigma_s + Q\left(1 - e^{-B\bar{\varepsilon}^p}\right) \tag{2.13}$$

$$\sigma_0 = \sigma_s + Q\left(1 - \left(1 - B\bar{\varepsilon}^p\right)\right) = \sigma_s + QB\bar{\varepsilon}^p \tag{2.14}$$

It leads to a linear variation of the stress with the equivalent plastic strain close to zero. With a linear trend curve defined from the equivalent plastic strain range of 0.001 to 0.002 (Fig. 2.9), the initial yield stress was taken as the intersection of the stress axis and the trend curve. This method is introduced to determine the initial yield stress in this study, and the obtained initial yield stresses for each test of uniaxial tension are listed in Table 2.5.

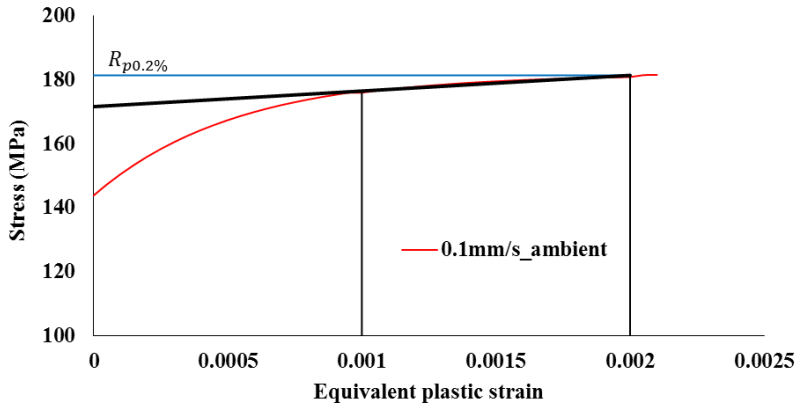

Fig. 2.9 Determination of initial yield stress.

Table 2.5 Initial yield stress for different condition

Tensile velocity and temperature	Yield stress (MPa)	Average
0.1mm/s_ambient	171.62	
10mm/s_ambient	175.50	166.16
200mm/s_ambient	151.37	
0.1mm/s_150°C	161.99	
10mm/s_150°C	143.05	145.19
200mm/s_150°C	130.52	
0.1mm/s_200°C	138.87	
10mm/s_200°C	134.0	133.84
200mm/s_200°C	128.66	

Experimental results show that the initial yield stress decreases with the increase of temperature, while the strain rate influence is generally not significant. Hence, in this work, only the temperature effect is considered for the initial yield stress. The evolution of initial yield stress in the range of temperatures can be described with the model given in Eq. 2.15 [34].

$$\sigma_0(T)=\left\{1-\frac{T}{T_m}\exp\left[K_0\left(1-\frac{T_m}{T}\right)\right]\right\}\sigma_0(T_0) \tag{2.15}$$

Where T is the current temperature, $T_m=617^{\circ}C$ is the melting temperature of the considered material and $\sigma_0(T_0)=166.16\,\text{MPa}$ is the initial yield stress at ambient temperature. K_0=0.2295 is obtained by fitting the initial yield stress in function of temperature with Eq. 2.15. The fitting curve is presented as follows:

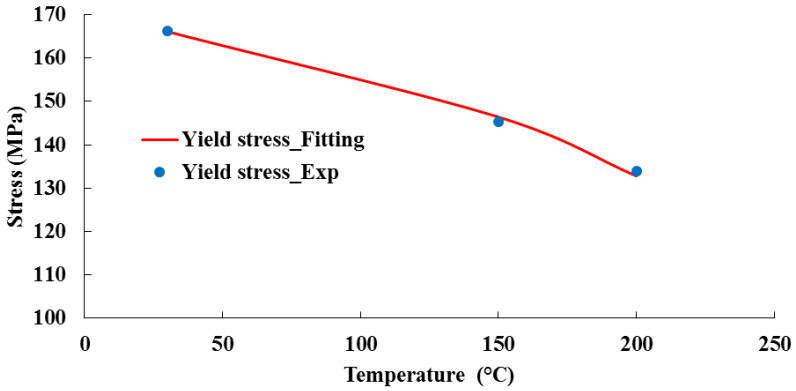

Fig. 2.10 Evolution of initial yield stress for AA6061.

2.5.2 Identified the hardening models

The analytical method is adopted for the calibration of hardening models under uniaxial tension. The temperature and strain rate are considered as constants in the identified procedure, indicating the plastic work on heating transfer is neglected here. The initial values are selected from the work of [30]. The calibration process is realized by using the modeFRONTIER software [117], which is an integration platform for multi-objective optimization, integrated with the MATLAB. To optimize the initial set of parameters, the SIMPLEX algorithm is selected here. The SIMPLX algorithm is a classical method for solving linear programming in optimization. This algorithm method has high efficiency for local optimization [118].

The parameters of each hardening models for AA6061 have been calibrated with experimental data along rolling direction and presented below.

- **Ludwick model**

Table 2.6 gives the parameters for the Ludwick model and the cost function between experimental and analytical data.

Table 2.6 Optimized parameters for the final Ludwick model

K_1 (MPa)	K_2 (MPa/°C)	n_0	n_1 (1/°C)	m_0	m_1 (1/°C)	Cost function δ
477.03	0.814	0.502	0.000653	0.0091	0.00643	0.023

The predictive results compared with experimental data under different tensile conditions are shown in Fig. 2.11. In the range of temperatures and tensile speeds, the Ludwick model

gives a good correlation at low strain. When the equivalent plastic strain is above 15%, the predicted flow stress tends to be overestimated compared to the experimental data due to the power law strain term of the hardening model.

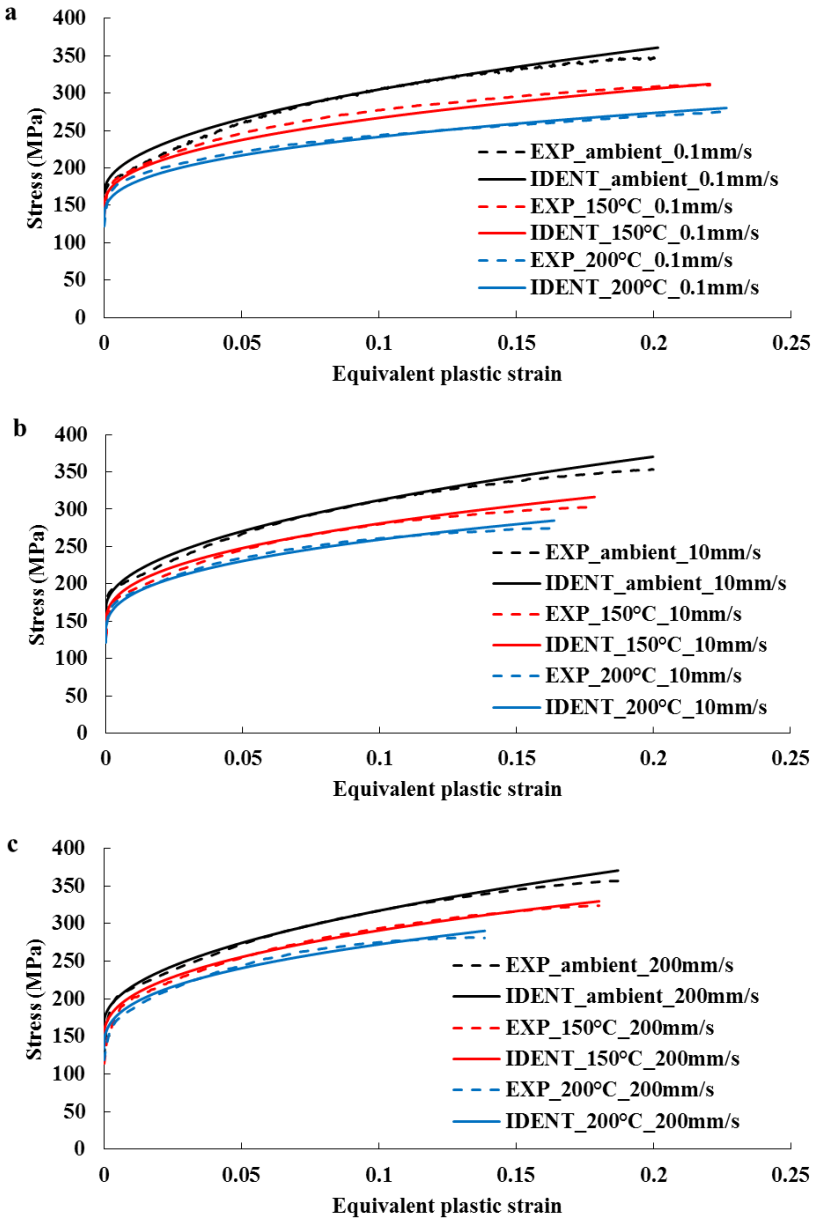

Fig. 2.11 Predictive results of Ludwick model under different temperatures and tensile speeds.

- **V_1 model**

The identified parameters for the V_1 model are presented in Table 2.7 and the predictive flow stresses are shown in Fig. 2.12.

Table 2.7 Optimized parameters for V_1 model.

K_1 *(MPa)*	K_2 *(1/°C)*	K_3	K_4 *(1/°C)*	m_0	m_1 *(1/°C)*	*Cost function* δ
334.2	0.00307	2.293	0.00633	0.00564	0.00811	0.018

The V_1 model presents a good correlation with the experimental data both for low and high strains. As confirmed by the value of the cost function, the predictions of this model are better than the ones from the Ludwick model.

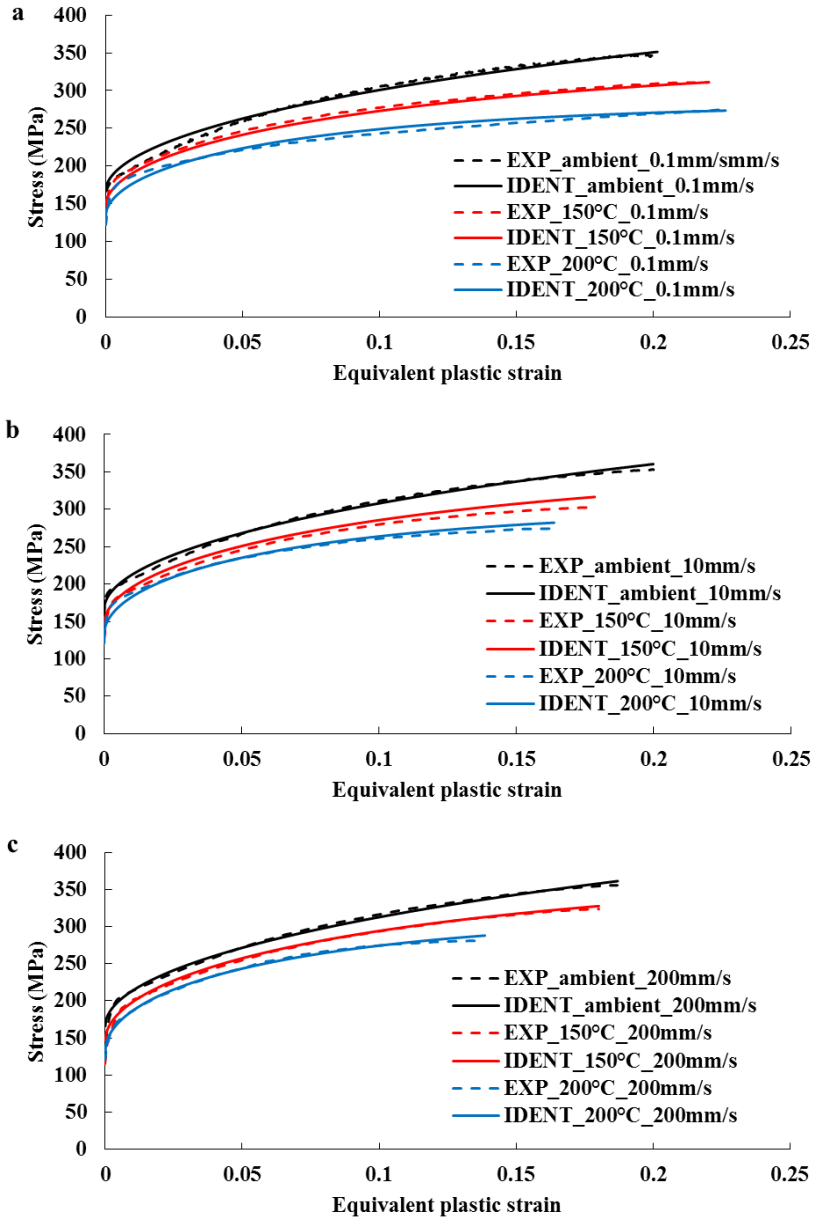

Fig. 2.12 Predictive results of V_1 model under different temperatures and tensile speeds.

- **V_2 model**

The identified parameters for the V_2 model are presented in Table 2.8 and the predictive flow stresses are shown in Fig. 2.13.

Table 2.8 Optimized parameters for V_2 model

K_1 (MPa)	K_2 (MPa/°C)	K_3	K_4 (1/°C)	m_0	m_1 (1/°C)	Cost function δ
200.8	0.0603	13.037	0.002	0.0064	0.0074	0.043

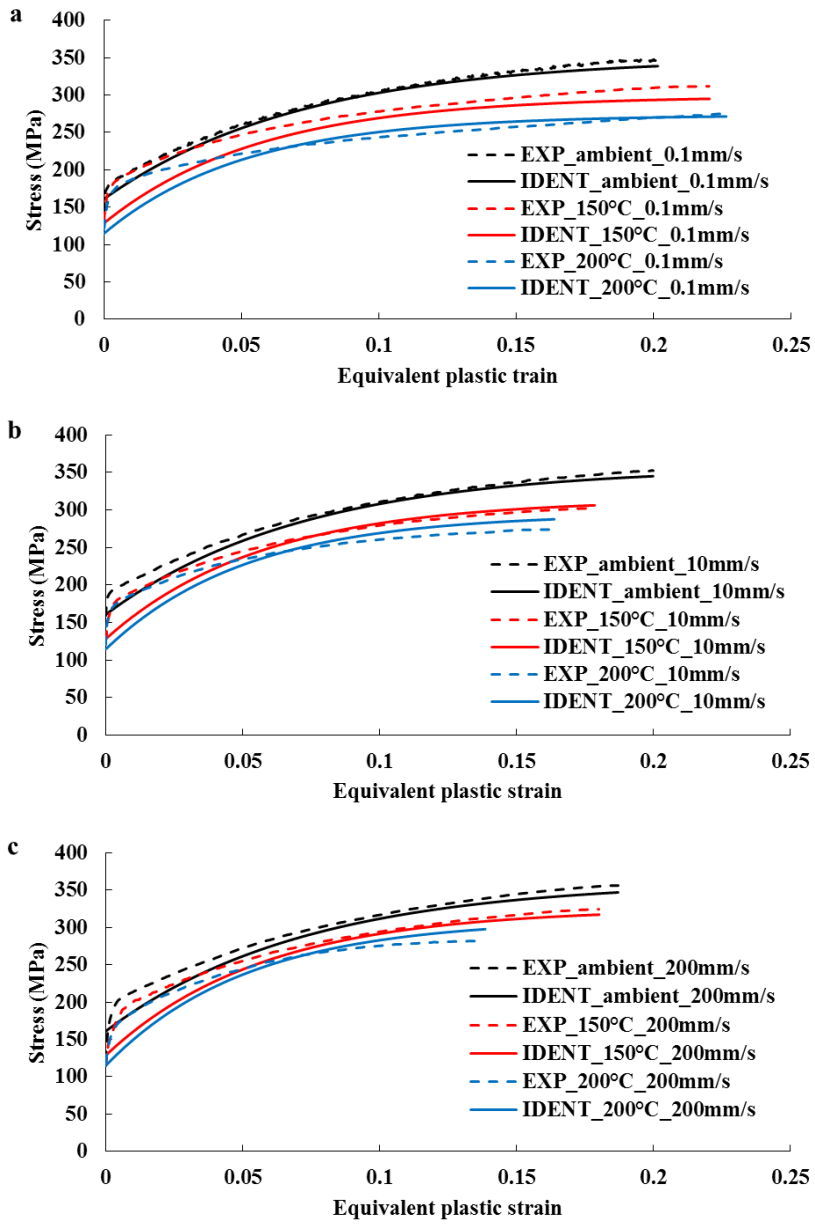

Fig. 2.13 Predictive results of V_2 model under different temperatures and tensile speeds.

The V_2 model gives a significant underestimation of the experimental stresses at the beginning of the plastic stage. Also, the saturation character appears with the equivalent plastic strain up to 18%. The cost function for this model is larger than for the other models, which indicates that the V_2 model is not appropriate to describe the hardening behavior of AA6061 at different temperatures and strain rates.

- ***V*3 model**

The V_3 model has been also identified in this work. Compared to the V_2 model, the V_3 model includes a power law strain term that will lead to a flow stress increase with the strain level while V_2 model exhibits a more pronounced saturated stress state for high strains [4].

The identified parameters for the V_3 model are presented in Table 2.9 and the predictive results of flow stresses are shown in Fig. 2.14.

Table 2.9 Optimized parameters for V_3 model

K_1 (MPa)	K_2 (MPa/°C)	K_3	K_4 (1/°C)	n_0	m_0	m_1 (1/°C)	Cost function δ
236.54	0.256	5.303	0.00121	0.701	0.00164	0.0148	0.028

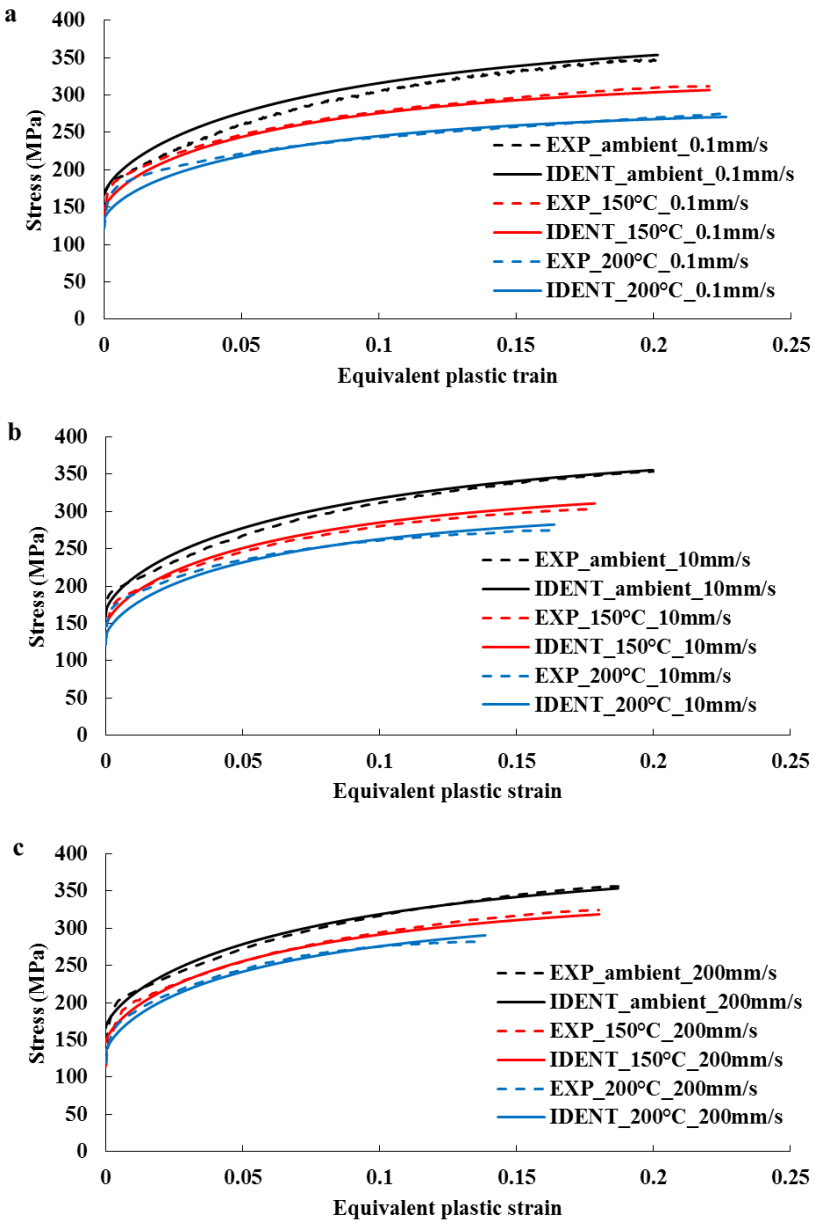

Fig. 2.14 Predictive results of V_3 model under different temperatures and tensile speeds.

Compared to the V_2 model, the V_3 model gives a better prediction of experimental data at the beginning of the plastic stage.

Fig. 2.15 gives the comparison of flow stresses for the four hardening models with a strain level up to 40%. For the equivalent strain below 18%, the predictions of Ludwick, V_1 and V_3 models are very close for the different conditions, while the V_2 model gives an underestimation at 200mm/s and 200°C (Fig. 2.15c). For the equivalent plastic strain above 18%, the Ludwick model shows a monotonic character of strain hardening for each temperature and tensile speed, while a pronounced steady flow stress is observed for the V_2 model for all the forming

conditions. An intermediate flow stress between the Ludwick model and the V_2 model is given by the V_1 and V_3 models. This two models give a similar saturation stress state at high strain level under 200°C and different tensile speeds (Fig. 2.15b, c).

Based on the results presented above, the selected models all give a reasonable description of strain hardening for AA6061 in a range of temperatures and strain rates. With the evolution of strain, the saturation type models tend to give better predictive results. Due to the minimum cost function value obtained for the V_1 model, this model will be selected to predict the strain hardening for different temperatures and strain rates under biaxial tensile conditions.

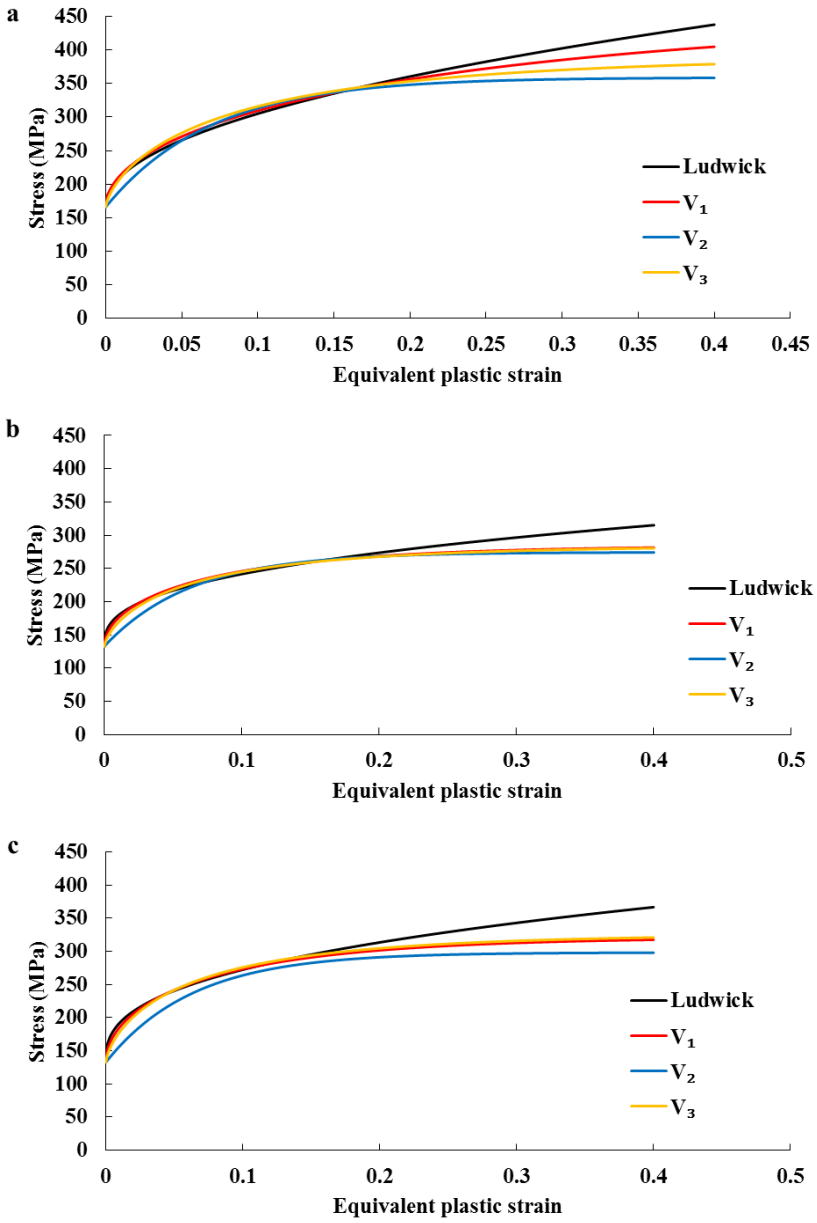

Fig. 2.15 Predictive results for Ludwick, V_1, V_2, and V_3 models with strain levels up to 40%: (a) ambient, 0.1mm/s; (b) 200°C, 0.1mm/s; (c) 200°C, 200mm/s.

2.6 Conclusion

In this chapter, a first characterization of the elasto-viscoplastic behavior of AA6061 is proposed thanks to the conventional uniaxial tensile test. The flow stresses at different temperatures and strain rates were directly obtained from the experimental results. The DIC technique was introduced to measure the strain evolution during the tests. From the experimental results, it can be found that the strain rate sensitivity at ambient temperature is negligible, while it becomes more and more significant with the increase of temperature. For a given strain rate, the temperature has a negative effect on the flow stresses.

The identification of parameters for Ludwick and Voce-type hardening models was performed in the same range of temperatures and strain rates. The four selected models give a good description of flow stresses for the different conditions with a strain level below 20%. The V_1 model seems to be the more suitable model, it is selected to study elasto-viscoplastic behavior of AA6061 under in-plane biaxial conditions in the following chapter.

Chapter 3 Investigation on the thermo-viscoplastic behavior of AA6061 by biaxial tests

3.1 Introduction

In the previous chapter, the thermo-viscoplastic hardening model for AA6061 has been identified based on uniaxial tension tests. Experimental results have shown that a maximum strain at rupture of approximately 20% is reached with such tests. To predict the hardening behavior at larger strains, biaxial tensile tests performed on a dedicated cruciform specimen are introduced in this work. This biaxial tensile machine also enables dynamic tensile tests to be carried out, allowing characterization in a strain rate range from quasi-static to the so-called "intermediate" strain rate (up to few s^{-1}). A specific heating device associated with this biaxial machine is used to carry out the temperature dependent characterizations.

The strain field on the surface of specimens for each test is determined by means of DIC technique. Through the comparison between experimental and numerical principal strains at the central point of the cruciform specimen, the material constants of the thermo-viscoplastic hardening model which has been discussed in chapter 2 are identified. This calibration stage is based on an inverse procedure coupling a FE simulation of the biaxial tensile test with an optimization platform.

3.2 Biaxial tensile tests of AA6061

3.2.1 Experimental setup

In the last decade, a specific in-plane biaxial tensile device in LGCGM (Fig. 3.1) has been used to investigate different mechanical behaviors (forming limits, failure criterion, viscoplastic hardening, plastic criterion…) for metallic materials under biaxial loadings [116,94,119,97]. This machine consists of two orthogonal axes in a horizontal configuration. Four independent hydraulic cylinders and four accumulators (two per axis) are fitted on this machine. The maximum loading capacity is 50KN for each axis while a maximum tensile speed of 2m/s on each cylinder can be reach, allowing quasi-static and dynamic tests. By imposing different tensile velocities on each direction, different strain paths can be imposed at the central point of the cruciform specimen. The forces along the two perpendicular directions are measured by two load sensors which link the grip system of the specimen and the sliding bar.

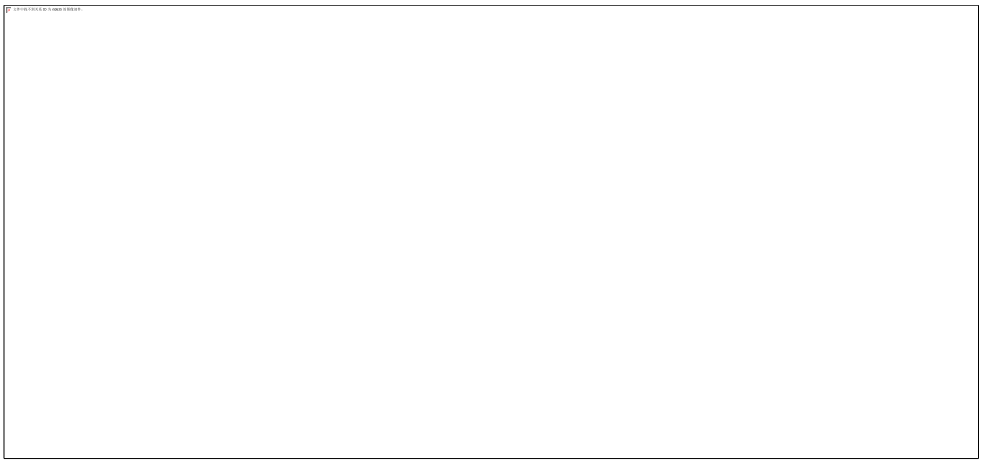

Fig. 3.1 Biaxial tensile device in LGCGM. [116,118]

Fig. 3.2 Mechanical part of one specimen arm loading device. [118]

For the dynamic tensile tests, the additional masses are accelerated along the sliding bars to obtain the required velocity before the specimen is loaded, then the specimen is impacted suddenly and the velocity is maintained during the test due to the inertia effect of the additional mass. It has been shown in [118] that when the sliding bars are suddenly impacted by additional masses, the load sensors ring at one of their eigen frequencies, leading to temporal force signals with many oscillations. Since only the specimen is modeled in the numerical simulations of the biaxial tensile test used later in this chapter (for the calibration of the thermo-viscoplastic hardening models by inverse procedure), the measured experimental force signals are the combination of both the dynamic elastic response of the load sensor and the material behavior of the specimen. Hence, the less vibration measurement forces is expected to be used in the numerical simulations. In this purpose, a damping layer is added between the sliding bar and the additional mass, as shown in Fig. 3.2, to reduce the level of vibration. This method has been used in [118] for dynamic biaxial tests on AA5086. Compared with the dynamic test without damping, the oscillation on the measured forces has been greatly reduced with a damping layer between the sliding bar and the impactor.

The heating device which has been developed here consists of an airflow generator and an insulated box as shown in Fig. 3.3a. The generated hot air is flowed into the insulated box through an inlet pipe and then return to the airflow generator through an outlet pipe. For a given set-point temperature, the temperature of the hot air sent by the air generator is regulated from the temperature measured inside the chamber by a remote probe. The temperature of the specimen is measured by thermocouples placed on the sample inner the insulation box. The allowed temperature range of the air flow generator is from -75°C to 200°C.

As shown in Fig. 3.3, a high-speed camera is placed on the central vertical axis of the biaxial bench to capture successive images of the specimen during the tensile stage through the glass pane on the top of the insulated box. The specimen is lighted from the outside, at the level of the glass window, by four strands of light directed towards the central area of the specimen (Fig. 3.3b).

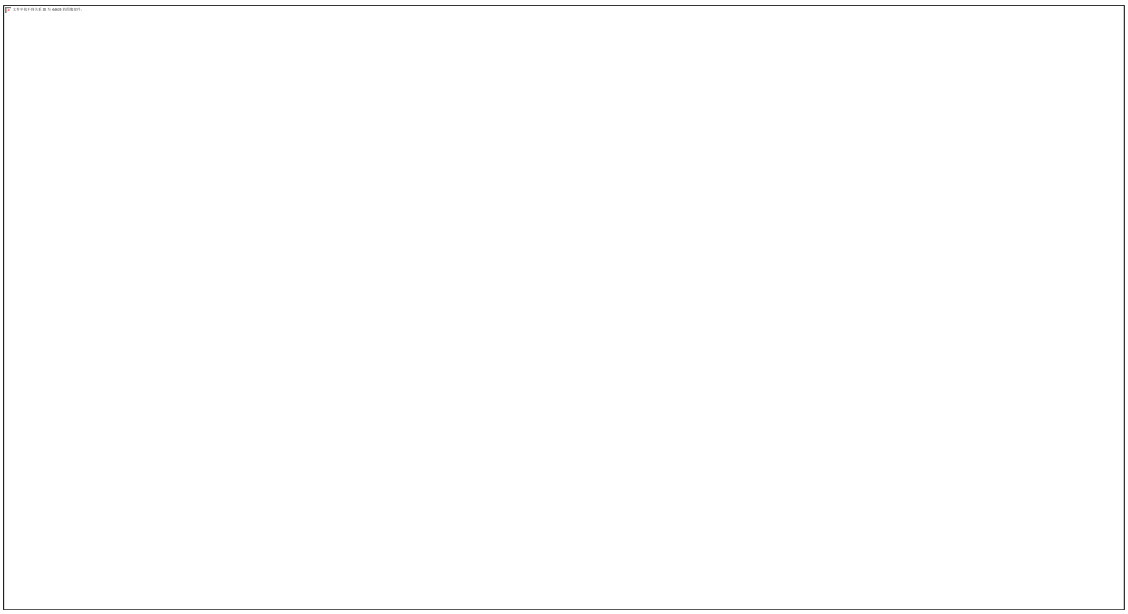

Fig. 3.3 Biaxial tensile machine equipped with heating device.

3.2.2 Cruciform specimen shape

The shape of the cruciform specimen used in this study (Fig. 3.4) has been proposed by W. Liu et al.[120]. With this shape, large equivalent plastic strains (up to 30% of equivalent plastic strain) in the central zone under equi-biaxial tensile loadings, for quasi-static or dynamic conditions, are obtained. In this study, the x axis corresponds to the transverse direction and y axis corresponds to the rolling direction.

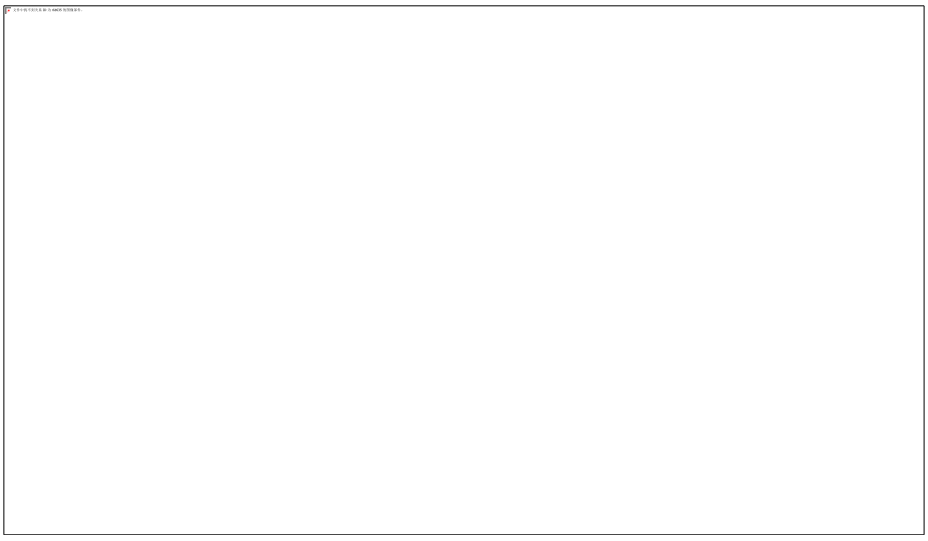

Fig. 3.4 Cruciform specimen shape for biaxial tensile test

3.2.3 Experimental operating conditions

Equi-biaxial tensile tests are performed at temperatures of 20°C, 100°C and 160°C for tensile speeds of 0.02mm/s, 2mm/s and 200mm/s (velocities applied on each arm).

Taking into account the heat losses (connecting pipes between the air flow generator and

the insulated box, thermal conduction between grips and specimen arm, …), a maximum temperature of 160°C can be reached at the level of the cruciform specimen placed on the test bench. It takes about 50 minutes to heat the specimen from ambient temperature to 160°C. Also, considering this heating time, the specimen temperature is assumed homogeneous before the test.

Main parameters of the camera and load measurement sensors are presented in Table 3.1.

Table 3.1 Main characteristics of acquisition

Test velocity (mm/s)	**Camera**			**Load sensor acquisition rate (Hz)**
	Image resolution (pixel)	**Acquisition rate (fps)**	**Shutter speed (s)**	
0.02	384×384	50	1/1000	50
2	768×720	500	1/500	500
200	384×368	15000	1/15000	50000

The specimens are not symmetrical in thickness as it can be seen in Fig. 3.4, so the random speckle pattern is generated on the flat side of the specimen before the tests (Fig. 3.5a). In the correlation stage, the subsets are defined on the images with a size of 32 pixels × 32 pixels and a distance of 16 pixels × 16 pixels to calculate the deformation. The magnification factor is 0.037mm/pixel. The gauge area treated by DIC is around 15mm square area with 720 analysis points as the blue area in Fig. 3.5b. The black circle of diameter 7.25mm corresponds to the central zone of constant thickness of the specimen. As will be seen later, the identification of strain-hardening is based on the experimental evaluation of the equivalent plastic strain at the central point of the specimen, the strain at this point is obtained by the average value as follows:

$$\varepsilon(t) = \frac{1}{m \times n} \sum_{j=1}^{m} \sum_{i=1}^{n} \varepsilon(i, j, t) \tag{3.1}$$

where *m* and *n* are number of points to be averaged along respectively X and Y directions and *t* is the time. In this work, the average strains are calculated over the 2×2 points on a 0.5mm square zone at the center of the specimen as the red square in Fig 3.5b.

(a) 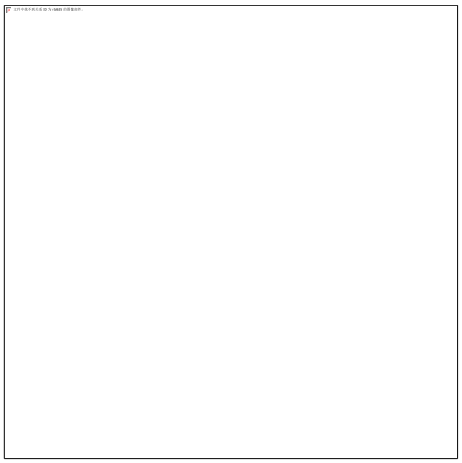 (b) 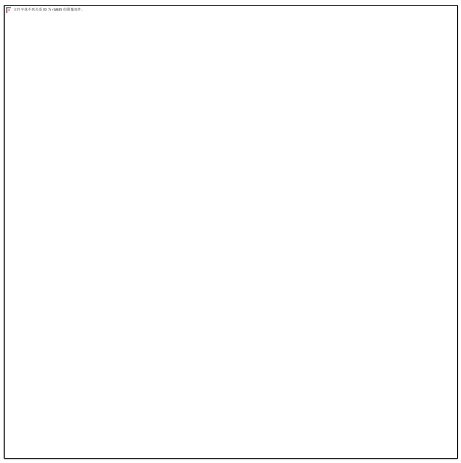

Fig. 3.5 Central zone of the specimen: (a) Speckle pattern; (b) Area processed by image correlation (purple square area), area of constant thickness (black circle) and averaged area (red square).

3.2.4 Experimental results of equi-biaxial tensile tests on AA6061

Biaxial tensile tests are performed at tensile speeds of 0.02mm/s, 2mm/s, 200mm/s and temperatures of 20°C, 100°C and 160°C. The experimental data needed for the identification stage of the thermo-viscoplastic strain-hardening model are: the principal strains at the center of the cruciform specimen and the tensile forces measured along the two axes (X and Y directions) of the specimen. Obviously, these temporal evolutions are synchronized before their use. Raw experimental data and post-processed data which will be used in the inverse identification procedure for the different operating conditions are presented below.

3.2.4.1 Equi-biaxial tensile test at 0.02mm/s and 20°C.

For the quasi-static biaxial tensile with a tensile speed of 0.02mm/s at room temperature, 634 images before the rupture are recorded, corresponding to a total time of 63.3s. The equivalent, major and minor strain fields at t = 55s in the gauge area are presented in Fig. 3.6a, b and c, respectively. The red circle corresponding to the thickness reduction zone (diameter of 10*mm*). Axis-x corresponds to the transversal direction, axis-y corresponds to the rolling direction. As explained above, the Von-mises equivalent and principal strains at the central point are calculated by the strain average on four points defined in a square area of 0.5mm side (Fig. 3.6a). This figure shows that the equivalent and principal strains are concentrated and nearly homogeneous in the central zone of the specimen. The red and blue arrows in Fig. 3.6b, c represented the directions of major and minor strains at the center of the specimen.

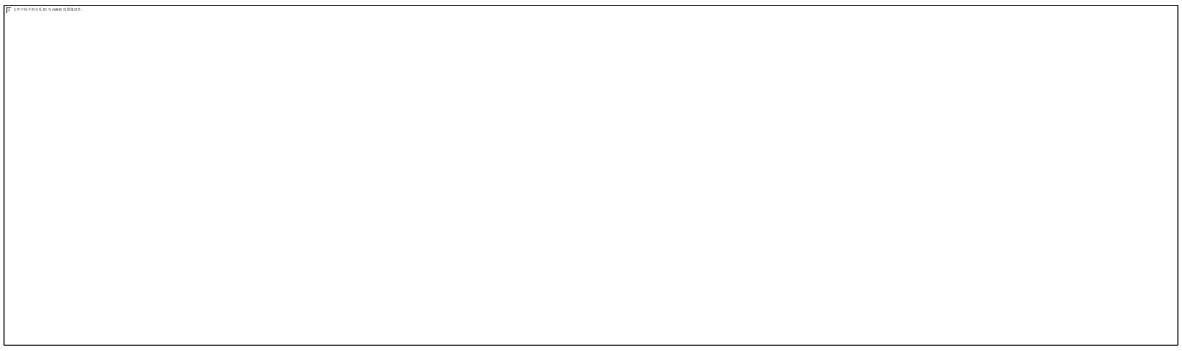

Fig. 3.6 Strain fields at 0.02mm/s and 20°C temperature: (a) Equivalent strain; (b) Major strain; (c) Minor strain.

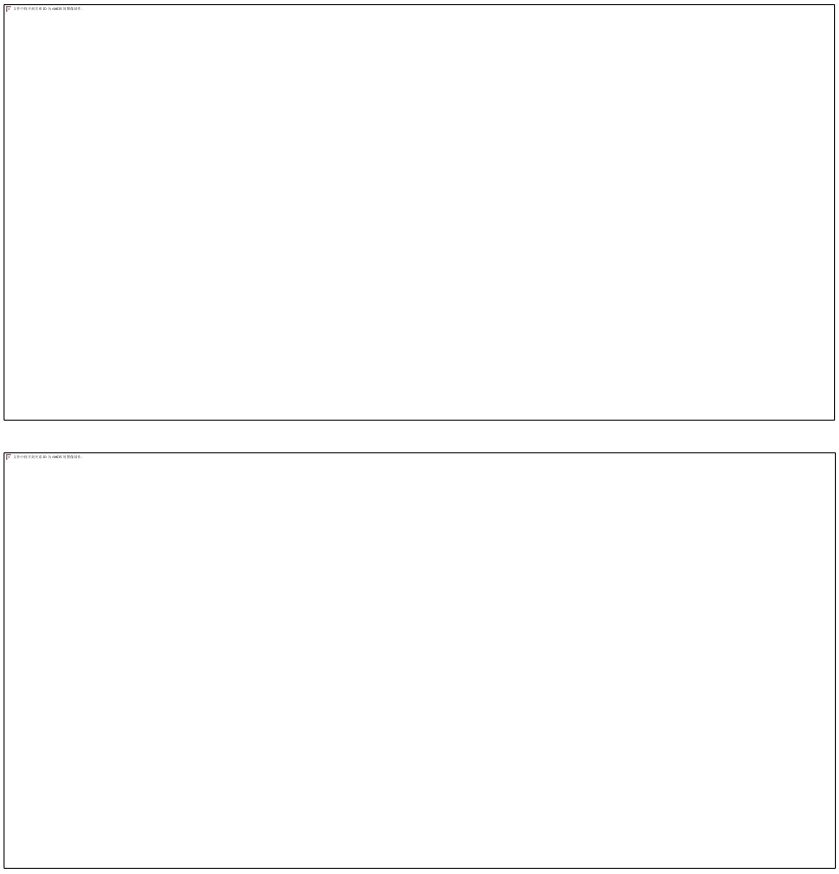

Fig. 3.7 (a) Experimental forces; (b) Equivalent and principal strains evolutions at the central point

The evolution of experimental forces versus time are shown in Fig. 3.7a. The maximum equivalent strain at the central point is about 25%, while the maximum major and minor principal strain at the central point are about 13% and 11%, respectively (Fig. 3.7b). Due to a slight asynchronization between the two axes, a small discrepancy is observed between the major and the minor principal strains. The influence of this slight desynchronization and of the possible anisotropy of the material is also visible on the curves showing the temporal evolution of the experimental forces according to the X and Y directions of the specimen (Fig. 3.7a). Portevin-Le Chatelier (PLC) effect [121], which are plastic instabilities, can be observed on the evolution of strain curves which present steps especially for large strains. This phenomenon is also clearly observed on the loads versus time curves which exhibit fluctuations. It can be noted

that the phenomenon of serration is clearly more pronounced on the effort measured according to X direction than according to Y direction. These fluctuations are the signature of PLC bands whose appearance is classically governed by the strain level, the strain rate and the temperature. However, the PLC effect has not taken into consideration in the identification procedure.

The curves of strain path and strain rate at the central point are shown in Fig. 3.8. As shown in this figure, the low strain levels at the beginning of the test (up to about 28s for this test) lead to two very noisy signals (strain path and strain rate). The strain path at the central point is about 0.9 after t = 35s which is nearly an equi-biaxial tensile strain state. The equivalent strain rate at the central point is fluctuating around $0.005s^{-1}$ from t = 30s to t = 55s. The strain rate is calculated as follows:

$$\dot{\bar{\varepsilon}} = \frac{\bar{\varepsilon}\left(t_{i+m}\right) - \bar{\varepsilon}\left(t_i\right)}{t_{i+m} - t_i}, \text{ when } t = \frac{t_{i+m} + t_i}{2} \tag{3.2}$$

where m is the time interval.

Fig. 3.8 Strain path and strain rate evolution at the central point

Due to PLC effects which appear especially at low tensile test velocities, both temporal force and strain curves must be smoothed before to be use in the inverse procedure of identification. For the considered operating condition (0.02mm/s; 20°C), the smoothed force and strain curves (using the moving average filter method in MATLAB) are shown in Fig. 3.9. Since the necking is not taken into account in this work, the time for the identification is considered up to t = 55s.

Fig. 3.9 Experimental forces and principal strains versus time curves for the hardening identification stage at 0.02mm/s, 20°C.

3.2.4.2 Equi-biaxial tensile test at 0.02mm/s and 160°C

For the tensile speed of 0.02mm/s at 160°C, there are 641 images before the rupture corresponding to t = 64s. The equivalent, major and minor strain fields at the gauge area at t = 64s are presented in Fig 3.10a, b, and c, respectively. Because we are close to the rupture and that the strain localization has already appeared at the edge of thickness reduction area (Fig. 3.10a), the strain distribution on this area is not uniform. Despite a slight desynchronization observed on the force versus time curves, Fig. 3.11a, of about 0.1mm, the strain evolutions at the central point are almost the same. Evolutions of equivalent and principle strains at the central point are shown in Fig. 3.11b. The maximum force for this condition is about 10% lower than the one at ambient due to the increase of temperature. The maximum equivalent strain for the central point is about 29%. The maximum major and minor principal strain at the central point are about 16.5% and 13%, respectively. PLC effects are greatly reduced at this level of temperature of 160°C. The increasing of temperature at low strain rate leads to a clear reduction of the serration amplitude for AA6061.

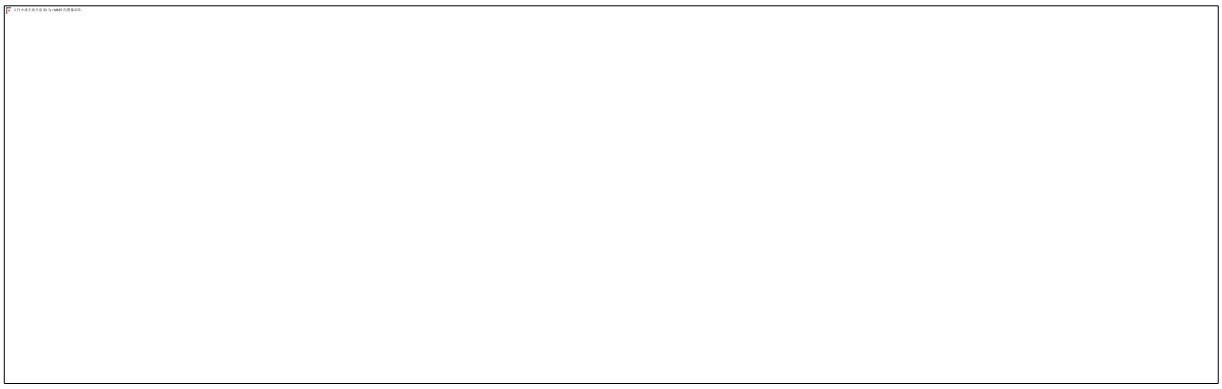

Fig. 3.10 Strain fields at 0.02mm/s and 160°C temperature: (a) Equivalent strain; (b) Major strain; (c) Minor strain

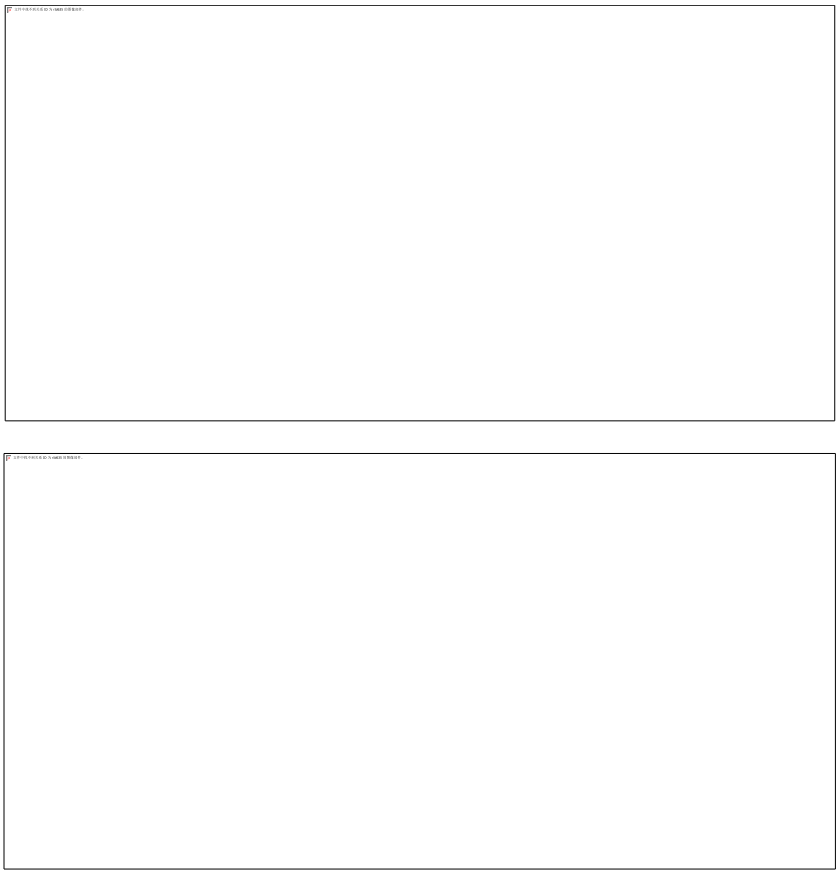

Fig. 3.11 (a) Experimental forces; (b) Equivalent and principal strains evolutions at the central point

The strain path and strain rate evolution at the central zone of the specimen is shown in Fig. 3.12. The strain path at the central point is about 0.93 after t = 40s which is nearly an equi-biaxial tensile strain state. The equivalent strain rate at the central point varied from $0.005s^{-1}$ to $0.01s^{-1}$ from t = 40s to t = 55s.

Fig. 3.12 Strain path and strain rate evolution at the central point

The experimental forces along the two specimen arms and principal strains at the central point have also been pre-processed for the identification, as shown in Fig. 3.13. The selected time for identification is up to t = 55s.

Fig. 3.13 Experimental forces and principal strains versus time curves for the hardening identification stage at 0.02mm/; 160°C.

3.2.4.3 Equi-biaxial tensile test at 2mm/s and temperatures of 20°C, 100°C and 160°C.

For the tensile speed of 2mm/s at ambient temperature, there are 348 images before the rupture corresponding to $t = 0.694s$. The equivalent, major and minor strain fields at the gauge area at $t = 0.6s$ are presented in Fig. 3.14a, b, and c, respectively.

The evolution of experimental forces and equivalent and principle strains at the central point are shown in Fig. 3.15. The maximum equivalent strain for the central point is about 25%. The maximum major and minor principal strains at this point are about 14% and 12%, respectively. A slight PLC effect is also observed, however this is much less pronounced at this speed of 2mm/s than at a speed of 0.02mm/s for the same 20°C temperature.

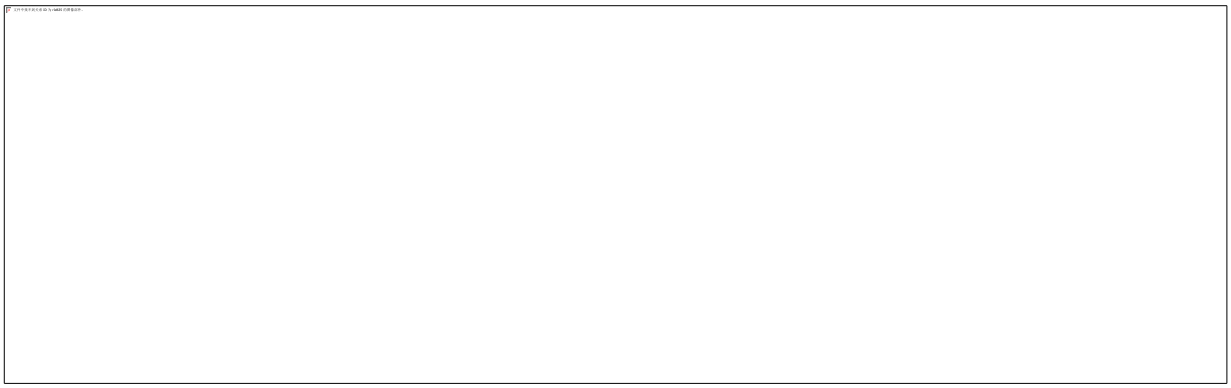

Fig. 3.14 Strain fields at 2mm/s and 20°C temperature: (a) Equivalent strain; (b) Major strain; (c) Minor strain.

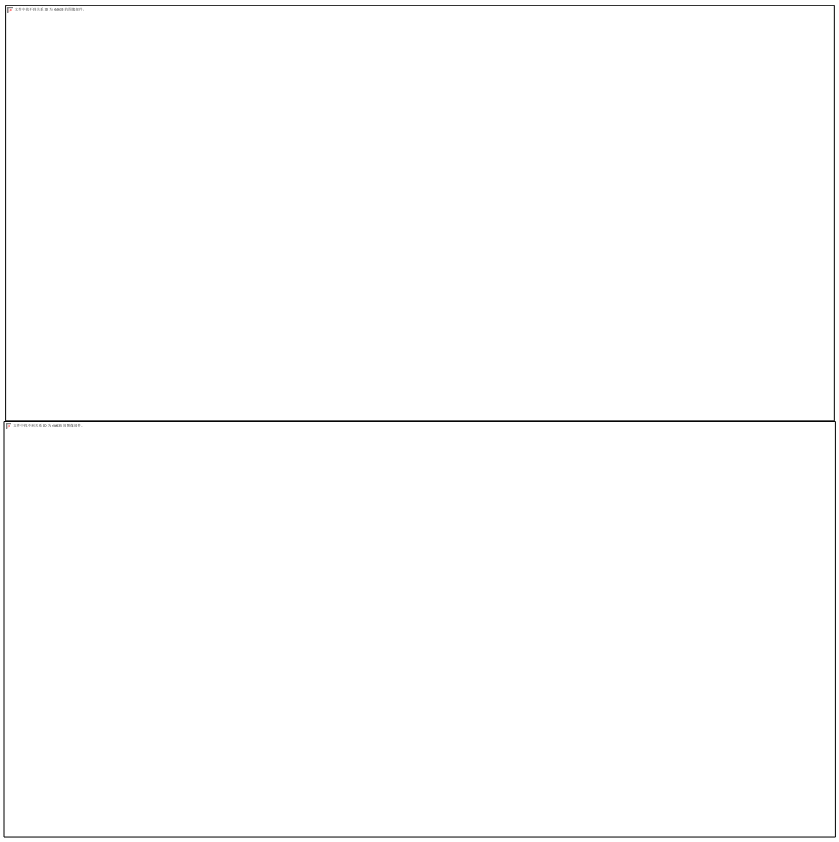

Fig. 3.15 (a) Experimental forces; (b) Equivalent and principal strains evolutions at the central point

Strain path and strain rate evolutions at the central point of the specimen are shown in Fig. 3.16. Due to the desynchronization of experimental forces at different directions, the strain path is nearly proportional of 0.8 after t = 0.4s. The equivalent strain rate at the central point is fluctuating around $0.5s^{-1}$ from t = 0.3s to t = 0.6s.

Fig. 3.16 Strain path and strain rate evolution at the central point.

The post-treated experimental forces along the two specimen arms and principal strains at the central point of the specimen are presented in Fig. 3.17 with those corresponding to operating conditions (2mm/s ; 100°C) and (2mm/s ; 160°C).

2mm/s ; 20°C	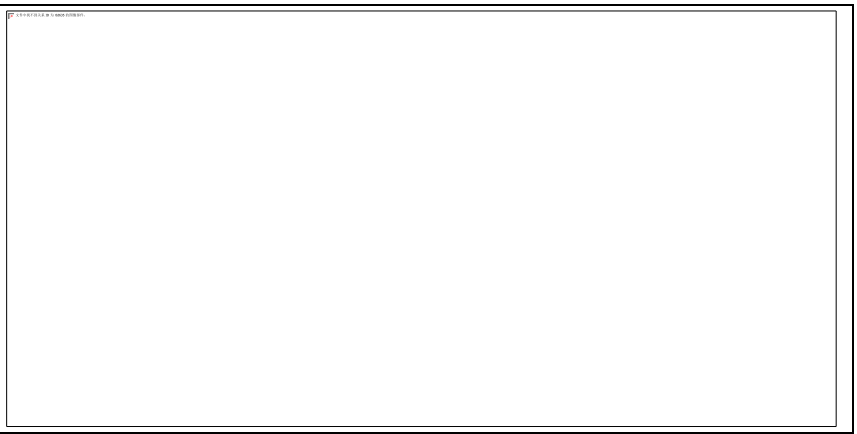
2mm/s ; 100°C	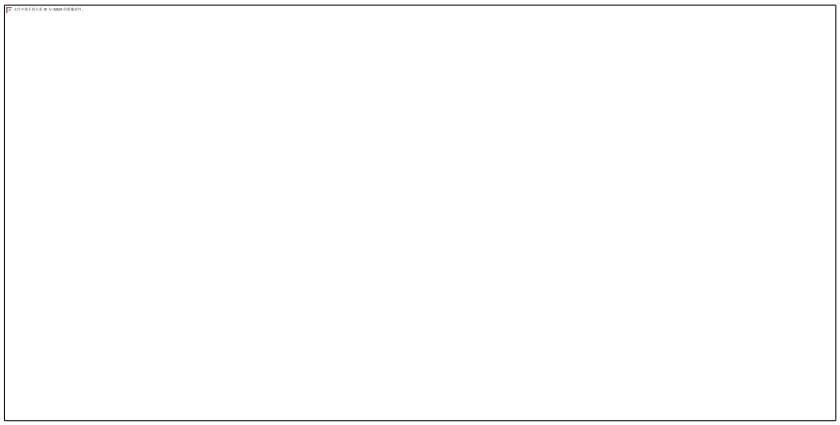
2mm/s ; 160°C	

Fig. 3.17 Experimental forces and principal strains versus time curves for the hardening identification stage at 2mm/s for temperatures 20°C, 100°C and 160°C.

3.2.4.4 Equi-biaxial tensile test at 200mm/s and temperatures of 20°C, 100°C and 160°C

In order to avoid oscillations induced on the force measurement by the excitation of the eigen frequencies of the mechanical parts of the specimen clamping system during tests at high speeds (such as the speed of 200mm/s), a damping element is introduced into the experimental set-up as explained in paragraph 3.2.1 and detailed in [118]. The experimental results for those dynamic tests at 200mm/s are presented as follows.

For the tensile speed of 200mm/s at ambient temperature (20°C), the equivalent, major and minor strain fields at the gauge area at $t = 0.01s$ are presented in Fig. 3.18a, b, and c,

respectively. Evolutions of experimental forces and the average of equivalent and principle strains for the central point are shown in Fig. 3.19. The maximum equivalent strain for the central point can reach about 30%, which is larger than the one under quasi-static condition (about 25%). Because of the forces along two directions are desynchronized , the major principal at the central point is reach up to 20%, while the minor principal strain is just about 9% at rupture. Compared with the quasi-static tensile test at room temperature, the PLC effect is not observed at such a tensile velocity.

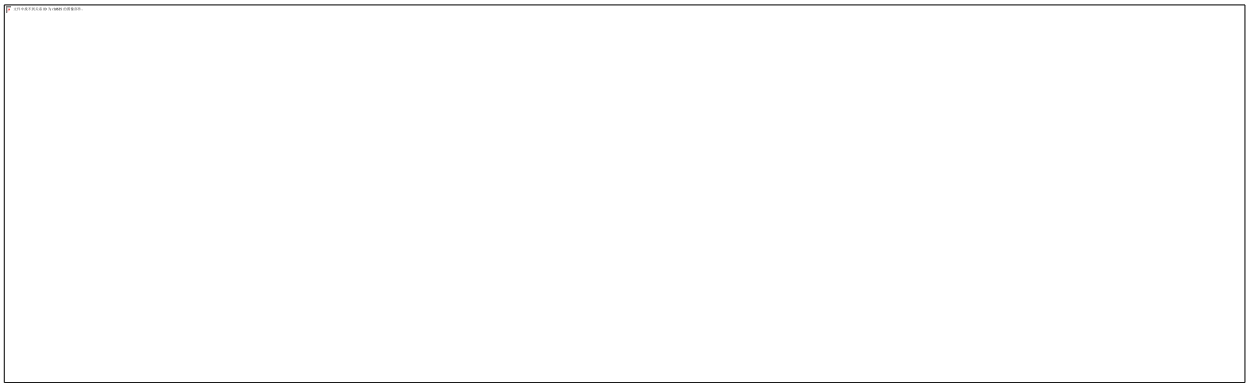

Fig. 3.18 Strain fields at 200mm/s and 20°C temperature: (a) Equivalent strain; (b) Major strain; (c) Minor strain.

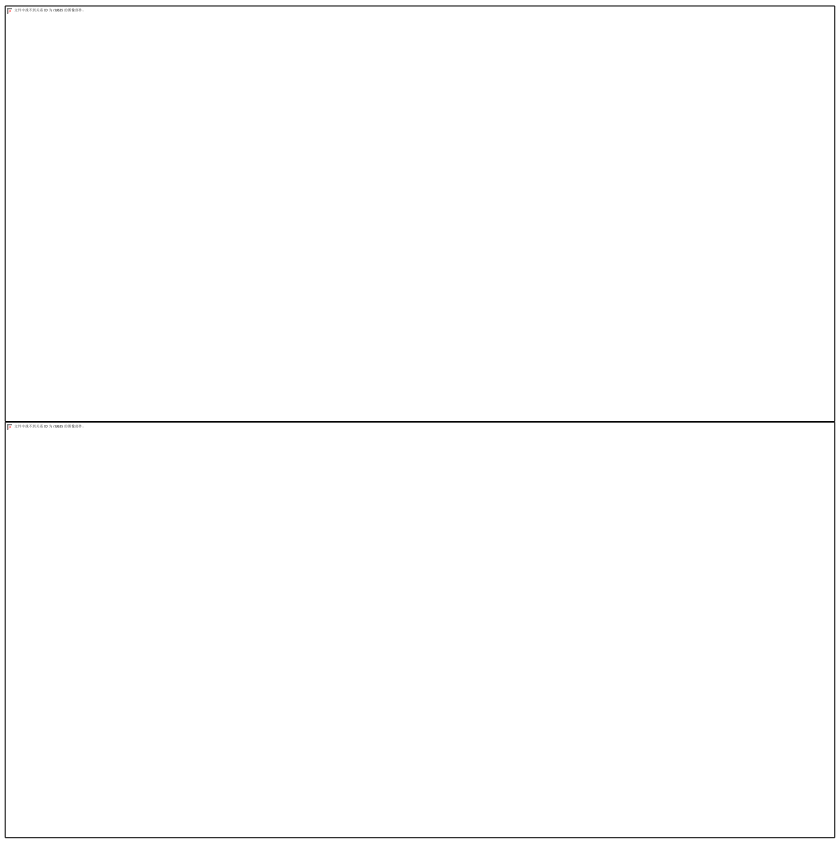

Fig. 3.19 (a) Experimental forces; (b) Equivalent and principal strains evolutions at the central point.

Strain path and strain rate evolutions at the central point of the specimen is shown in

Fig. 3.20. The strain path is between 0.5 and 0.7 during the plastic strain stage. The equivalent strain rate at the central point is around $40s^{-1}$ between $t = 0.007$s and $t = 0.011$s.

Fig. 3.20 Strain path and strain rate evolution at the central point

The post-treated data for all the operating conditions at 200mm/s (it means at temperatures 20°C, 100°C and 160°C) are presented in Fig. 3.21.

3.2.5 Discussion

The 8 designs of equi-biaxial tensile test for AA6061 performed in this study are recalled in Table 3.2. According to the strain fields presented above, the maximum strains localized in the central zone of reduced thickness show a relatively uniform distribution as expected. The experimental strain path at the central point varies around a mean value of 0.8 for the 0.02mm/s and 2mm/s conditions and shows more dispersion for the 200mm/s tests. Depending on the tensile test, the equivalent strain rate varies within a range from $0.005s^{-1}$ to $40s^{-1}$.

Table 3.2 Experimental designs for AA6061

	Ambient	100°C	160°C
0.02mm/s	☑		☑
2mm/s	☑	☑	☑
200mm/s	☑	☑	☑

In order to visualize the influence of the different operating conditions (temperature and speeds), the evolution of the tensile forces according to the rolling direction (Y direction) is represented as a function of the equivalent deformation at the central point of the specimen (Fig. 3.22 and 3.23).

200mm/s, 20°C	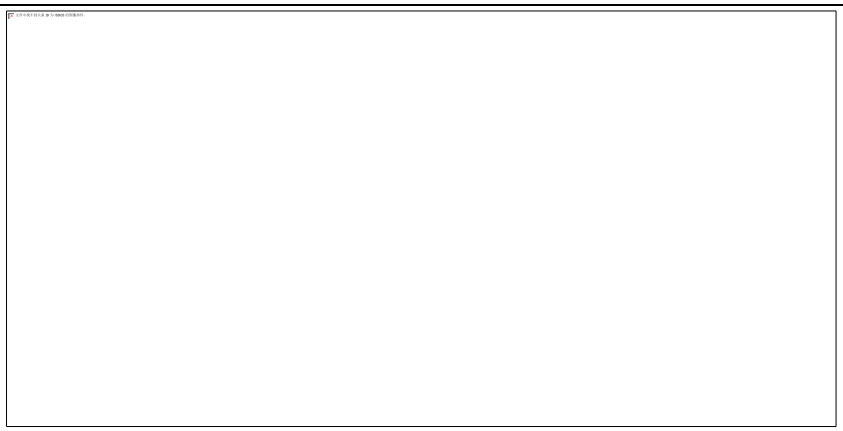
200mm/s, 100°C	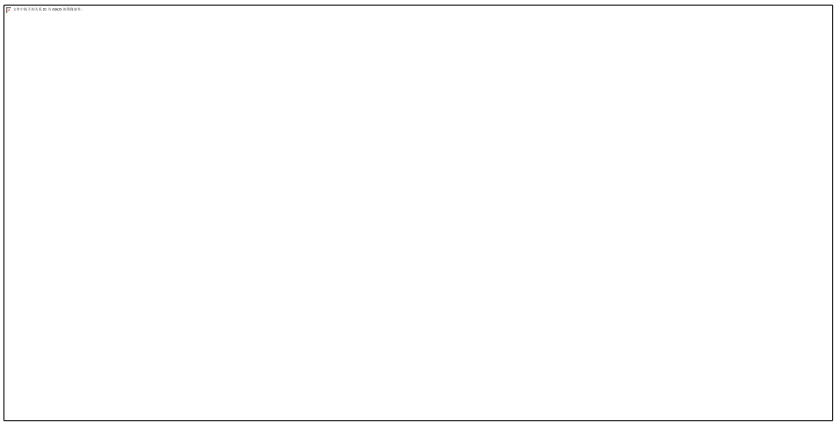
200mm/s, 160°C	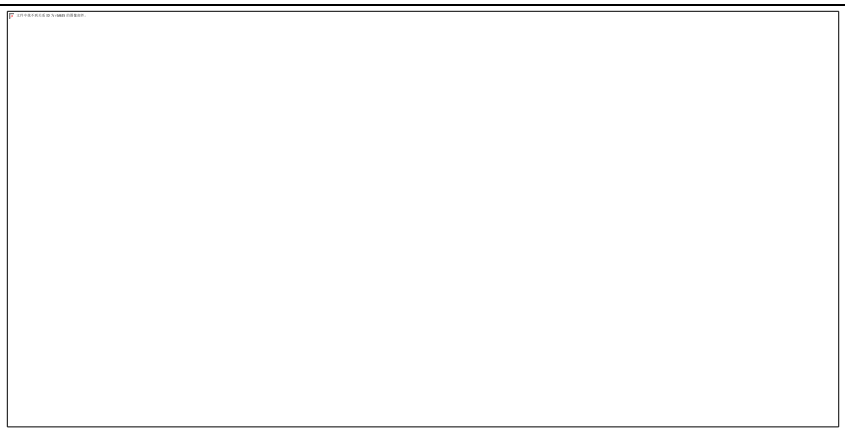

Fig. 3.21 Pre-processed experimental force and principal strain curves at 200mm/s

Compared the forces along y-axis (rolling direction) for the quasi-static condition, the tensile strengths decrease with the increasing of temperature (Fig. 3.22). The forces at 160°C between the tensile speeds of 0.02mm/s and 2mm/s are quite similar, indicating the strain rate effect is negligible at the low tensile speeds in a certain range of temperatures (20 to 160°C). The force at 2mm/s and ambient temperature is a little larger than the one at 0.02mm/s, which may be led by the geometry of the specimen for this condition is not totally the same to the others.

Fig. 3.22 Evolution of forces versus equivalent strain for quasi-static condition.

The forces along the rolling direction (y-axis) for dynamic condition are also compared in Fig. 3.23. A negative temperature effect on the tensile strength can be observed. For the high tensile speed, the ductility of AA6061 increases with increasing temperature.

Fig. 3.23 Evolution of forces versus equivalent strain for dynamic condition.

The maximum forces along the rolling direction (Y-direction) for all the experimental tested conditions are presented in Fig. 3.24. At the same tensile speed, the tensile strength decreases with the increasing of temperature for both quasi-static and dynamic conditions. Within the range of the tested strain rates, no clear trend can be seen at room temperature, so negligible strain rate can be assumed at this temperature. A small positive strain rate sensitivity can be observed at 160°C between the conditions 0.02mm/s, 2mm/s and 200mm/s and the same trend seems to be found at 100°C between the two conditions tested.

The maximum equivalent strains are obtained at the image just before rupture. The maximum equivalent strains are quite similar between different temperatures under low speed tension. While in the tensile speed of 200mm/s, the maximum equivalent strain increases gradually with increasing temperature (up to 40%). It can be supposed that the ductile ability for AA6061 is dependent on the temperature at a high strain rate. The strain rate effect is negligible when the temperature is below 100°C. Therefore, in order to reduce the time consuming in optimization, the case at 100°C with the tensile speed of 0.02mm/s is not

considered in the test.

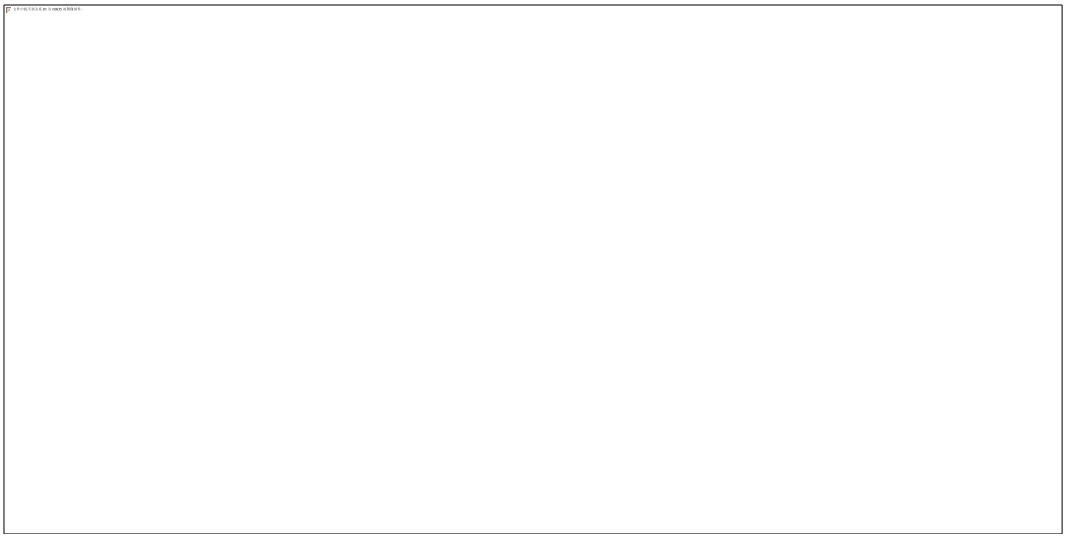

Fig. 3.24 Comparison of the maximum force and equivalent strain for the 8 different operating conditions.

Based on the aforementioned analysis, the temperature and tensile speed have an influence on the mechanical behavior of AA6061 under biaxial tension. The experimental results obtained from the biaxial tensile tests at different temperatures and strain rates can be introduced in the identification of hardening behavior for AA6061 at a large strain (25% to 30%).

3.3 Identification of thermo-viscoplastic hardening model under in-plane biaxial loadings

The thermo-viscoplastic hardening model (Eq. 2.7) calibrated under uniaxial tension in chapter 2 is identified in this section by means of inverse procedure since the assumed homogeneity of the uniaxial tensile test cannot be retained for the in-plane biaxial tensile test which is highly heterogeneous.

3.3.1 Procedure of inverse analysis

The inverse procedure of parameter identification is presented in Fig. 3.25. This procedure is based on a finite element (FE) model of the in-plane biaxial tensile test applied on the cruciform specimen defined in section 3.2.2. Temporal evolutions of experimental forces along the two axes of the specimen are introduced as boundary conditions in the FE model to simulate the biaxial tension of AA6061. At the end of the simulation, the numerical observable quantities are the principal strains at the central point of the specimen whereas the experimental observables are the principal strains calculated by DIC technic.

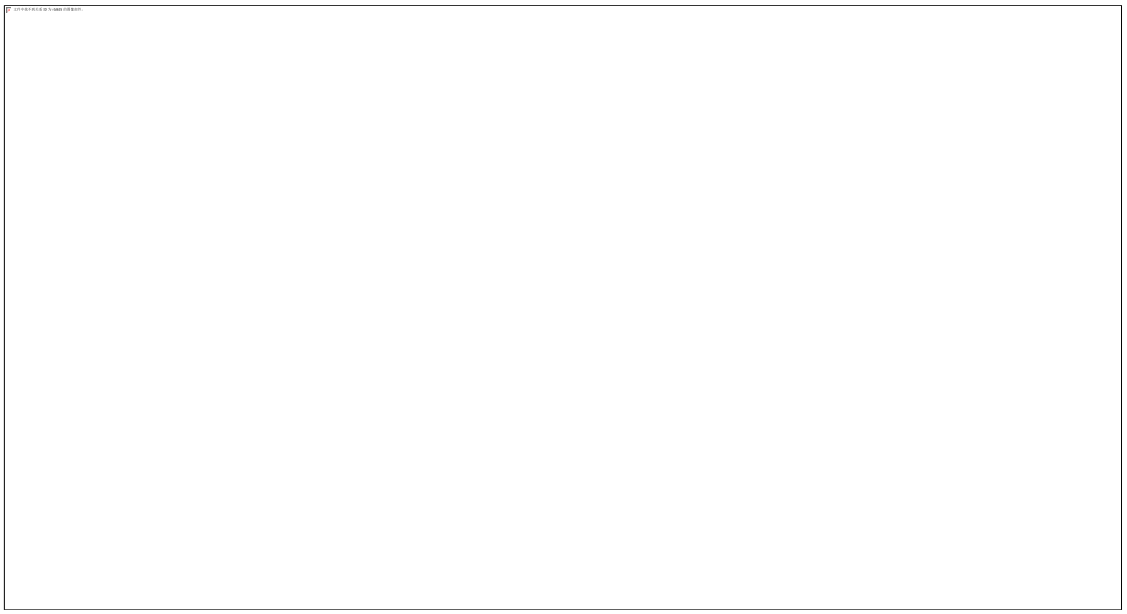

Fig. 3.25 Flowchart of parameters identification.

By comparing the temporal evolutions of the experimental and numerical principal strains at the central point of the specimen, the cost function δ is calculated as follows:

$$Q = \frac{1}{p}\sum_{k=1}^{p} Q_k \quad \text{with} \quad Q_k = \frac{1}{2}\sum_{i=1}^{2}\sqrt{\left(\sum_{j=1}^{q}\left(\varepsilon_i^{sim}\left(t_j\right)-\varepsilon_i^{\exp}\left(t_j\right)\right)^2 \Big/ \sum_{j=1}^{q}\left(\varepsilon_i^{\exp}\left(t_j\right)\right)^2\right)} \tag{3.3}$$

Where p is the number of design in the identification; q is the total number of time points during simulation; ε_1^{sim} and ε_2^{sim} are the major and minor numerical strains at the central point of the specimen; $\varepsilon_1^{\exp}$ and $\varepsilon_2^{\exp}$ are the experimental principal strains at the central point of the specimen.

The best set of parameters of the hardening model is obtained by minimizing the gap between experiment and numerical simulation strain versus time curves. To do this, the multi-disciplinary and multi-objective optimization platform modeFRONTIER is used. This software allows the coupling between FE simulation codes, such as Abaqus used in this study, and optimization algorithms. The convergence for Simplex method is less efficient than that for many other algorithms when the parameter number is increased. A best approach could consist in a hybrid method to localize approximately the global minimum of the cost function and then converge efficiently with a first-order optimization algorithm. In this work, the MOGA and Simplex were chosen for parameter identification. MOGA (Multi-objectives Genetic Algorithm) is adopted as guided random search method. This method is suitable for solving multi-objective optimization related problems with the capability to explore the diverse regions of solution space. In the early stages of optimization, this method is used to roughly determine the value area of parameters. Thereafter, the Simplex method is applied for looking for the local minimum solution.

3.3.2 Finite element model

Based on a coupled temperature-displacement analysis with implicit solver, FE simulations of the biaxial tensile test at different loading conditions (temperatures: 20, 100 and 160 °C and tensile speeds: 0.02, 2, and 200 mm/s) are led. The model is based on a shell element mesh of the in-plane cross specimen. To keep reasonable simulation time, shell element mesh is preferred rather than 3D element mesh. This point is of paramount importance since this model is integrated next in an inverse procedure for the identification of material parameters. This procedure requires an important number of FE simulations to determine the best set of material parameters of the thermo-viscoplastic model. The mesh of the specimen is shown in Fig. 3.26 (only one quarter due to symmetry). From a parametric study, W. Liu et al. [118] have defined the equivalent thicknesses of the different regions of the shell element mesh giving the same strain evolution in the central zone of the specimen than the one given by the 3D solid mesh. Zone A is the central flat thickness-reduced zone with the thickness of 0.625 mm, zone B is the transition zone with a thickness of 1.3125 mm, while zone C has the initial sheet thickness of 2 mm. Four node shell element (S4RT) are used for this model. For boundary conditions, sides 1 and 2 are symmetry axes. Experimental forces F_x and F_y are applied on sides 3 and 4 along axis X and Y, respectively. Since the central zone is the zone of interest under biaxial tensile state, a refined mesh with a dimension of 0.25mm, is defined in this area. Adiabatic assumption is assumed for all simulated conditions.

Fig. 3.26 FE mesh of the cruciform specimen

The Young's modulus (E = 63240 MPa) for AA6061 obtained in chapter 2 is assumed independent on the temperature and the strain rate. The Poisson ratio for this material is ν = 0.33 [112] is also considered a constant for different conditions. The hardening law identified in section 2.3 is programmed through the user subroutine UHARD in the environment software ABAQUS. The thermal properties of AA6061 adopted in simulations are presented in Table 3.3 [38].

Table 3.3 Material properties of AA6061

Temperature ($°C$)	Thermal conductivity ($W.m^{-1}.K^{-1}$)	Heat capacity ($J.kg^{-1}.K^{-1}$)	Density ($kg.m^{-3}$)	Melting point ($°C$)
0	162	917		
98	177	978	2703	582-652
201	192	1028		

The thermo-viscoplastic model to be identified is recalled below (Eq. 2.8 and 2.15):

$$\bar{\sigma}=\sigma_0\left(T\right)+K_1\exp\left(-K_2T\right)\sqrt{1-\exp\left[-K_3\exp\left(K_4T\right)\bar{\varepsilon}_p\right]}\dot{\bar{\varepsilon}}_p^{m_0\exp\left(m_1T\right)}$$

$$\sigma_0\left(T\right)=\left\{1-\frac{T}{T_m}\exp\left[K_0\left(1-\frac{T_m}{T}\right)\right]\right\}\sigma_0\left(T_0\right)$$

In these numerical simulations, adiabatic conditions are assumed and no heat exchanges are considered between the specimen and the environment of the insulated box and specimen grips. At the beginning of the simulation, a constant temperature (the set-point one) is assumed in the specimen.

3.3.3 Parameter identification

In Chapter 2, an analytical regression method has been used to calibrate the parameters of the hardening model at different temperatures and strain rates under uniaxial tension. In this analytical model (where stress and strain fields are considered as homogeneous), the adiabatic deformation-induced thermal effect is neglected. In contrary to the uniaxial tensile test, the biaxial tensile test performed on the specific specimen shape defined in this study is strongly inhomogeneous and do not allow experimental determination of the initial yield stress under biaxial strain state. Hence, the initial yield stress at ambient temperature (20°C) is identified with the others hardening parameters for the different biaxial tensile conditions experimentally tested. The initial yield stress parameter K_0 = 0.2295 (section 2.5.1) determined from uniaxial tensile conditions is always considered here for the identification stage under biaxial loadings since the temperature effect on the initial yield stress is assumed to be the same whatever the strain state.

The parameters of the thermo-viscoplastic hardening model identified are shown in Table 3.4. The prediction of principal strains for the different conditions are compared with experimental data, as shown in Fig. 3.27.

Table 3.4 Identified parameters for the hardening model.

σ_0 (MPa)	K_1 (MPa)	K_2 (1/°C)	K_3	K_4 (1/°C)	m_0	m_1 (1/°C)
148.55	351.87	0.0036	1.039	0.0087	0.0024	0.013

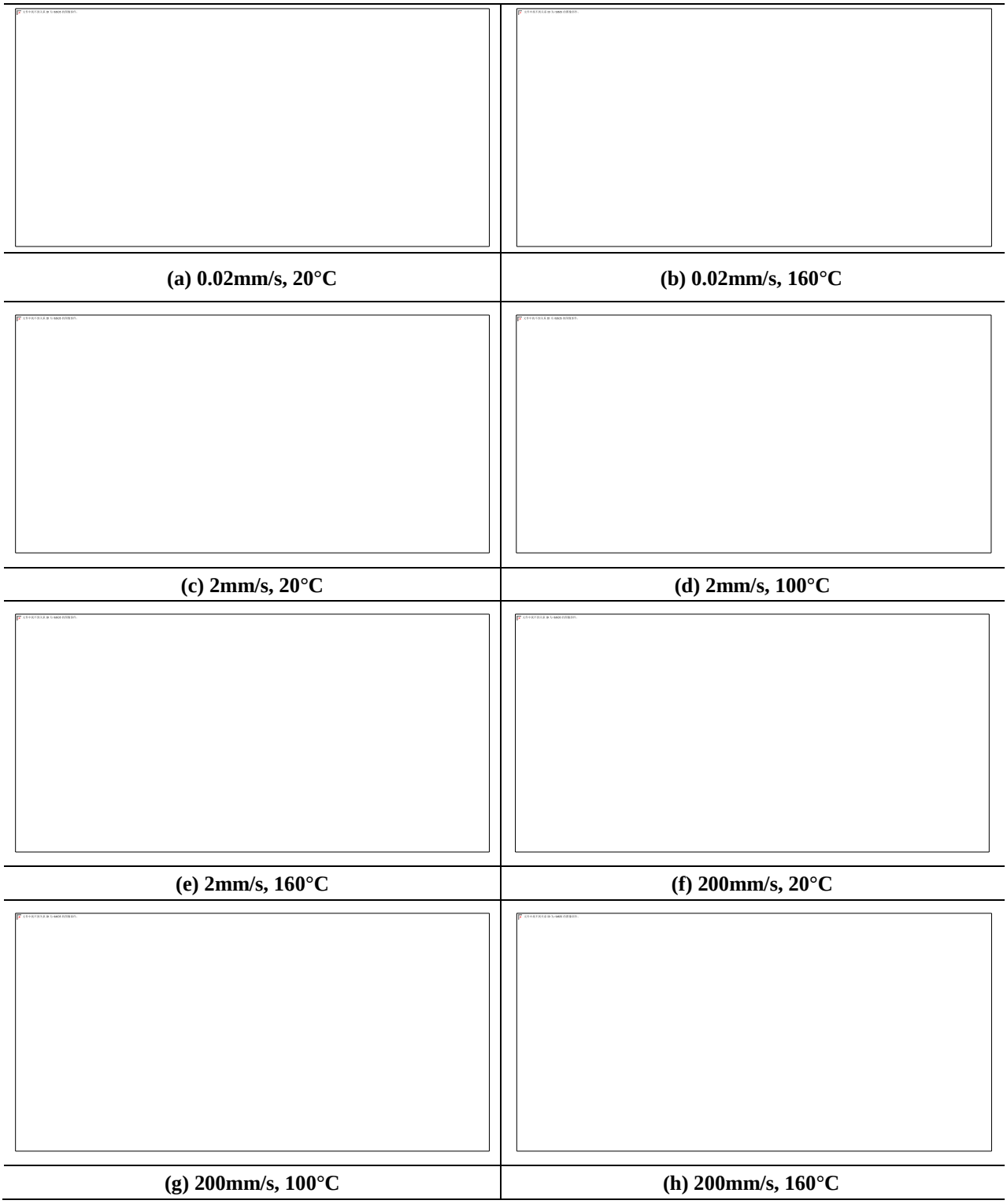

(a) 0.02mm/s, 20°C | **(b) 0.02mm/s, 160°C**

(c) 2mm/s, 20°C | **(d) 2mm/s, 100°C**

(e) 2mm/s, 160°C | **(f) 200mm/s, 20°C**

(g) 200mm/s, 100°C | **(h) 200mm/s, 160°C**

Fig. 3.27 Comparison of experimental and numerical temporal strain evolutions at the central point for different conditions.

Fig. 3.27 shows that the identified hardening model based on biaxial tensile tests can well describe the evolution of principal strains in the range of temperatures and strain rates tested. The initial yield stress under biaxial tension at room temperature is lower than the one obtained from uniaxial tension ($\sigma_{0\_uniaxial} = 166.16 MPa$). For the tensile velocity of 2mm/s at 100°C and 160°C (Fig. 3.27d, e), the prediction of principal strains give an underestimation compared to

the experimental data mainly at the end of the test for larger strains. That maybe due to the adiabatic in the simulation and the softening effect dominate the hardening behavior. For the tensile velocity of 200mm/s at 100°C and 160°C (Fig. 3.27 g. h), this phenomenon have not been observed in terms of the strain rate compensation. For the tensile velocity of 2mm/s at ambient temperature (Fig. 3.27c), the prediction of strains are higher than the experimental results with the increasing of time, we suppose there is a difference of size or thickness at the central area of this specimen than the others.

The predictions of the flow stresses at a large strain by the identified hardening model for different temperatures (ambient, 100°C, and 160°C) and strain rates ($0.001s^{-1}$, $0.1s^{-1}$, and $10s^{-1}$) are shown in Fig. 3.28. Constant temperatures and strain rates are introduced in these models and the equivalent stress is plotted up to an equivalent plastic strain of 40%. It can be seen that the predicted flow stresses decrease with the increase of temperature. A positive strain rate influence on the flow stress curves can be observed at each temperature, and with the increase of temperature, the strain rate effect becomes more and more significant in a large strain.

Fig. 3.28 Prediction of the identified hardening models from biaxial tensile tests at a large strain.

3.4 Conclusion

In this Chapter, a heating system has been developed for a specific dynamic biaxial tensile device and biaxial tensile tests on AA6061 have been performed in a range of temperature (ambient to 160°C) and strain rates (10^{-3} to $10s^{-1}$). With a dedicated cruciform specimen proposed by Liu W. et al. [120], the temperature and strain rate sensitive hardening behavior of AA6061 has been identified for large strains.

With the aforementioned analysis, we can draw several conclusions:

(1). With the developed heating system, the specimen can be precisely controlled and kept at a homogeneous temperature before the test. The limitations are the maximal achievable temperature and the heating time from ambient to this maximal temperature.

(2). Experimental results show that the temperature has a negative effect on the tensile strength. The influence of strain rate is negligible with the temperature below 100°C, while a positive effect on the tensile strength can be observed at 160°C.

(3). The predicted strains at the cruciform specimen center by the identified thermo-viscoplastic hardening model under biaxial tension in a range of temperatures (ambient to 160°C) and strain rates (10^{-3} to $10s^{-1}$) presents good agreement with experimental data. The biaxial flow stresses at different tensile speeds are very similar at temperatures below 100°C, while at 160°C a positive strain rate is observed. This is basically the same as the conclusion drawn from the experimental data.

In the following Chapter, the thermo-viscoplastic hardening model identified under biaxial tension will be coupled with an anisotropic yield criterion to study the temperature and strain rate sensitivity of the anisotropic response of AA6061.

Chapter 4 Investigation of anisotropic behavior of AA6061 under biaxial tensile state

4.1 Introduction

The heterogeneous strain field measured by digital image correlation in the central gauge area of a cruciform specimen can permit to characterize the plastic anisotropic behavior of metallic sheets with a unique specimen [15]. Indeed, minor and major strains measured along several paths exhibit a wide range of strain states, from uniaxial to equi-biaxial stress state. Thanks to the recording of forces along the two loading directions and to the strain field measurement, an identification of complex anisotropic yield criteria with several parameters is possible by inverse procedure. Then, a unique test is sufficient to characterize the anisotropic behavior of the sheet.

The first aim of this study is to verify that the method can be applied when the in-plane biaxial tensile test is performed under different conditions of temperature and strain rate. Then the effect of temperature and strain rate on the anisotropic behavior of AA6061 sheet will be discussed. For this purpose, the biaxial device equipped with the air flow generator is used to perform in-plane biaxial tensile tests at different tensile velocities (1mm/s and 200mm/s) and temperatures (-40°C, ambient, and 160°C) . With the user's subroutine UMAT on Abaqus, the parameters of the Bron and Besson criterion are identified at room temperature and for quasi-static conditions. The biaxial tensile tests for the different tested conditions are simulated by the FE method, the identified hardening behavior of the material, including the effect of strain rate and temperature, is introduced. Then, with the anisotropic parameters identified at room temperature and for quasi-static condition, the predictive evolution of principal strains and strain path ratios for the different tested conditions are presented and compared to the experimental ones.

4.2 Calibration method for anisotropic yield criterion

4.2.1 Presentation of the method

Recently, Zhang et al. [15] proposed a new methodology to identify the parameters of anisotropic yield criteria for metal sheets. This method has been validated both on an aluminum alloy (AA5086) and on a dual phase steel (DP980). Two anisotropic yield criteria, Hill48 [6] and Bron and Besson [14], have been identified by the proposed methodology. In the study, conventional homogeneous tests (uniaxial tension, hydraulic bulging and simple shear) are firstly used to identify the parameters of each yield criterion. Then, in order to evaluate the efficiency of the method, the results are compared with the ones obtained with only one equi-biaxial tensile test performed on a cruciform sample. It was shown that the yield surfaces identified by the conventional method and by the proposed method are very close.

The finite element simulation of the cruciform specimen was carried out with the experimental forces of biaxial test imposed as boundary conditions (Fig. 4.1b). Due to the symmetry of the specimen, only a quarter of the specimen is modeled. The experimental forces $F_x/2$ and $F_y/2$ are imposed on the two arms. The inverse analysis methodology consists of minimizing the gap between the experimental and numerical distributions of the major and minor strains along the diagonal direction of the sample central area as shown in Fig. 4.1a, at

an instant before the rupture. The flowchart of the identification process with equi-biaxial tensile test is given in Fig. 4.2.

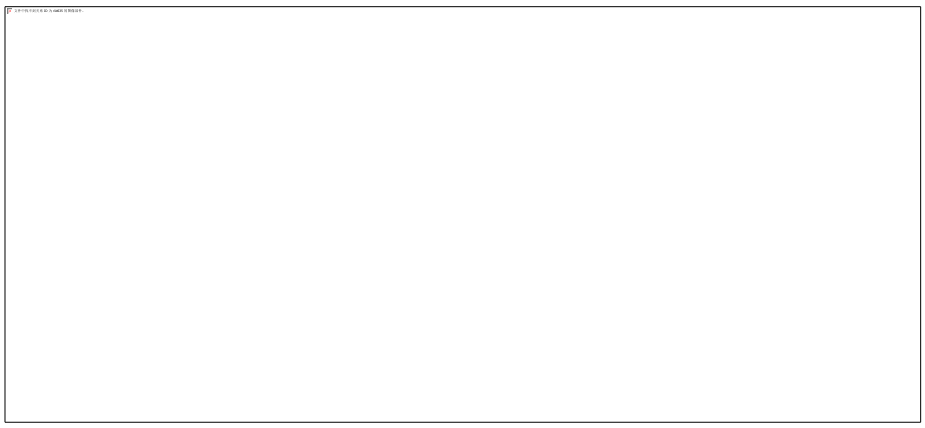

Fig. 4.1 (a) Specific strain path for the identification; (b) FE boundary conditions with imposed force

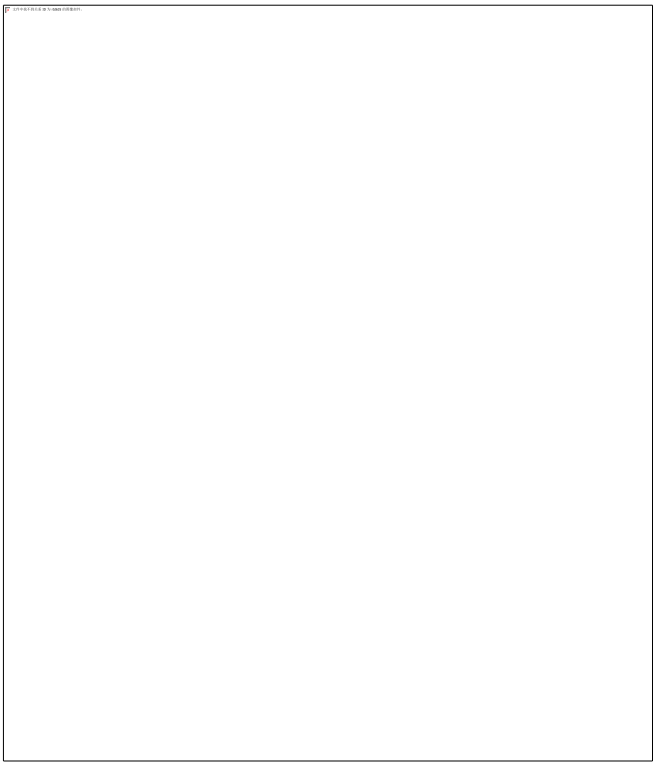

Fig. 4.2 Flowchart of the identification process with the biaxial test. [116]

For AA5086, with the identification strategy presented above, the Bron and Besson yield criterion can well describe the evolution of principal strains along the diagonal path as shown in Fig. 4.3c, but for the longitudinal and transversal path (x and y direction), predictions show significant differences compared to the experimental data as shown in Fig. 4.3a and Fig. 4.3b.

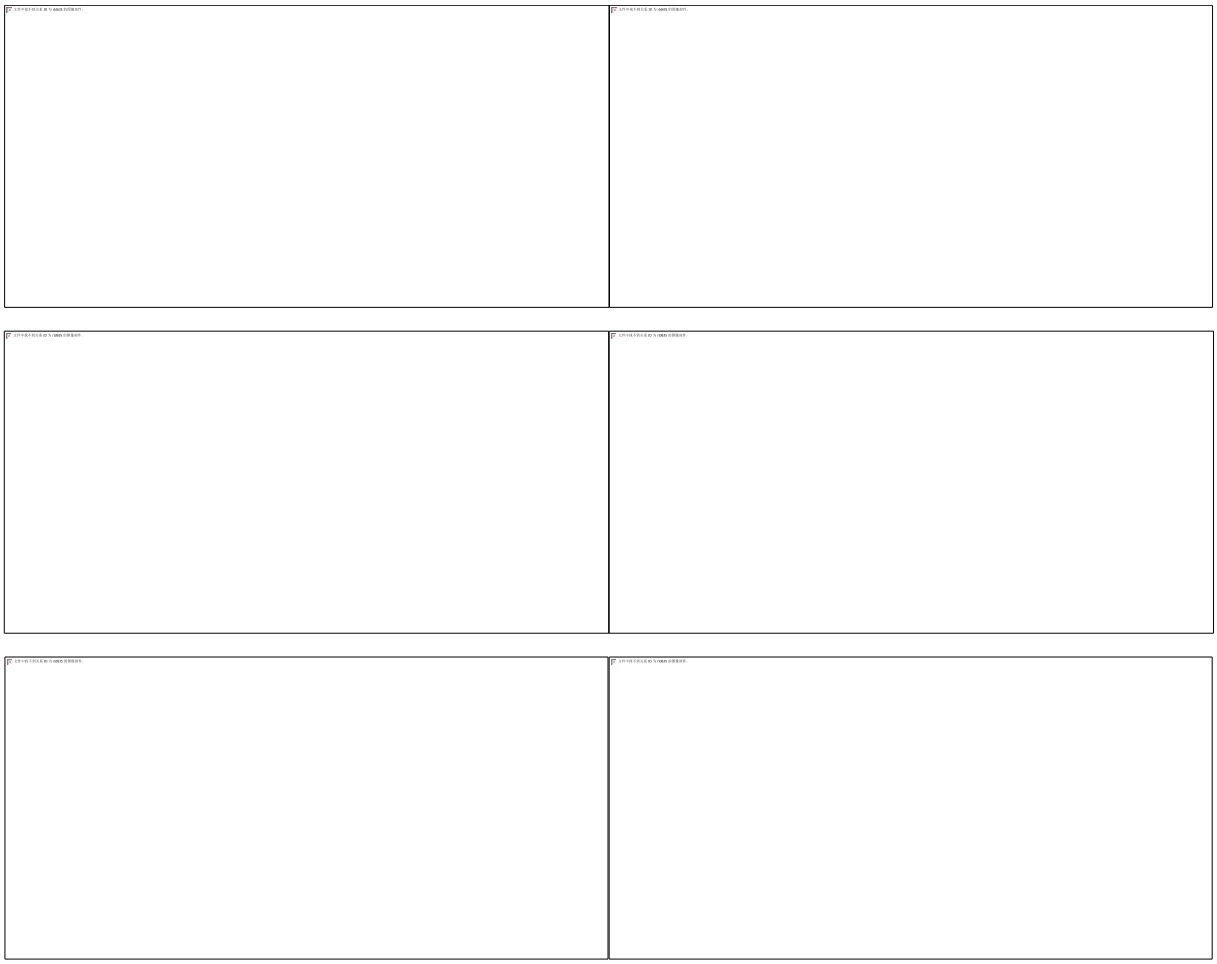

Fig. 4.3 Evolution of principal strain and strain path ratio along different directions: (a) diagonal path; (b) longitudinal path; (c) transversal path.

The method based on the single equi-biaxial tensile test is considered to be adequate to get the parameters for both yield criterion (such as Hill48) with few parameters but also for more complex yield criterion such as Bron & Besson (with 12 parameters). However, some discrepancies can be observed when predicted and experimental principal strains are compared along transversal and longitudinal (rolling direction) paths in the central area of the cross specimen.

4.2.2 Improvement of the method

4.2.2.1 Identification strategy

In order to improve the accuracy of the predictive results, a modification of the identification strategy is proposed in this section. Based on the same method, additional experimental data have been integrated in the calibration procedure. The parameters of the yield criterion are now identified by comparing experimental and predictive principal strains along longitudinal (x direction), transversal (y direction) and diagonal directions at the same time. The identification process is still realized with the software modeFRONTIER.

A cost function is defined to calculate the difference between the experimental and

numerical principal strains to identify the 12 parameters of Bron and Besson yield model:

$$\begin{aligned}
\delta_x &= \sum_i^p \left(\frac{\varepsilon_{1,x}^{numi} - \varepsilon_{1,x}^{\exp i}}{\varepsilon_{1,x}^{\exp i}} \right)^2 + \sum_i^p \left(\frac{\varepsilon_{2,x}^{numi} - \varepsilon_{2,x}^{\exp i}}{\varepsilon_{2,x}^{\exp i}} \right)^2 \\
\delta_y &= \sum_i^p \left(\frac{\varepsilon_{1,\mathrm{y}}^{numi} - \varepsilon_{1,\mathrm{y}}^{\exp i}}{\varepsilon_{1,\mathrm{y}}^{\exp i}} \right)^2 + \sum_i^p \left(\frac{\varepsilon_{2,\mathrm{y}}^{numi} - \varepsilon_{2,\mathrm{y}}^{\exp i}}{\varepsilon_{2,\mathrm{y}}^{\exp i}} \right)^2 \\
\delta_{diag} &= \sum_i^p \left(\frac{\varepsilon_{1,\mathrm{diag}}^{numi} - \varepsilon_{1,\mathrm{diag}}^{\exp i}}{\varepsilon_{1,\mathrm{diag}}^{\exp i}} \right)^2 + \sum_i^p \left(\frac{\varepsilon_{2,\mathrm{diag}}^{numi} - \varepsilon_{2,\mathrm{diag}}^{\exp i}}{\varepsilon_{2,\mathrm{diag}}^{\exp i}} \right)^2 \\
\delta_b &= \delta_x + \delta_y + \delta_{diag}
\end{aligned} \tag{4.1}$$

where $\varepsilon_1^{\exp i}(\varepsilon_{1,x}^{\exp i}, \varepsilon_{1,y}^{\exp i}, \varepsilon_{1,diag}^{\exp i})$ and $\varepsilon_2^{\exp i}(\varepsilon_{2,x}^{\exp i}, \varepsilon_{2,\,y}^{\exp i}, \varepsilon_{2,diag}^{\exp i})$ are the experimental values for the major and minor strains respectively; $\varepsilon_1^{numj}(\varepsilon_{1,x}^{numj}, \varepsilon_{1,y}^{numj}, \varepsilon_{1,diag}^{numj})$ and $\varepsilon_2^{numj}(\varepsilon_{2,x}^{numj}, \varepsilon_{2,y}^{numj}, \varepsilon_{2,diag}^{numj})$ are the numerical principal strains respectively; p is the number of strain calculation points. As shown in Fig. 4.4, for a given distance from the center $d^{\exp\_i}$, the corresponding numerical principal strain $\varepsilon_1^{numi}(\varepsilon_{1,x}^{numi}, \varepsilon_{1,y}^{numi}, \varepsilon_{1,diag}^{numi})$ and $\varepsilon_2^{numi}(\varepsilon_{2,x}^{numi}, \varepsilon_{2,y}^{numi}, \varepsilon_{2,diag}^{numi})$ are interpolated from the principal values calculated at the adjacent nodes.

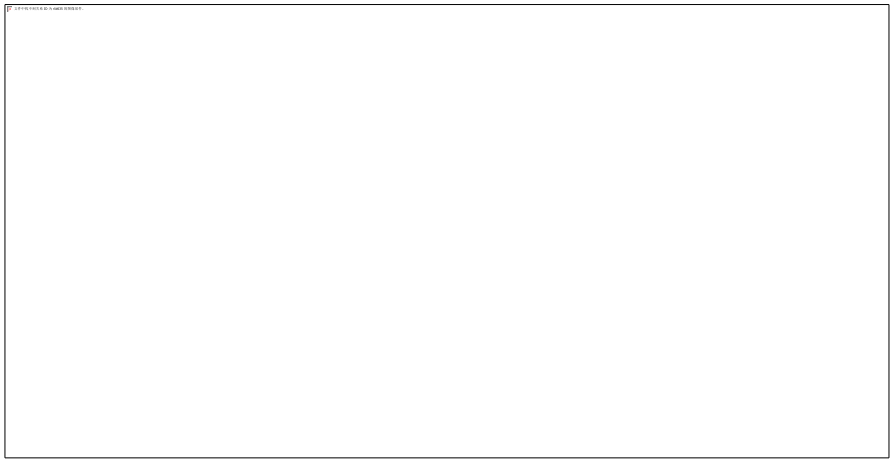

Fig. 4.4 Interpolation of the numerical strain field to calculate values at the position given by experiments.

4.2.2.2 Identification result

Based on the results of the previous identification on AA5086 [116], the variation range of each parameter is determined for this material (Table 4.1). Table 4.2 gives the optimized parameters of B&B yield model obtained from the improved calibration method. The Y_0 corresponding to the reference stress under biaxial tension (Eq. 4.2). η is a constant which depends on the parameters of yield model (Eq. 4.3). σ_0 is the yield stress under uniaxial tension.

$$Y_0 = \eta \cdot \sigma_0 \tag{4.2}$$

$$\begin{cases} \eta = \left(\alpha_1 \psi_1^a + \alpha_2 \psi_2^a\right)^{1/a} \\ \psi_1 = \dfrac{1}{2}\left(\left|\dfrac{c_2^1 - c_3^1}{3}\right|^{b_1} + \left|\dfrac{2c_2^1 + c_3^1}{3}\right|^{b_1} + \left|\dfrac{c_2^1 + 2c_3^1}{3}\right|^{b_1}\right)^{1/b_1} \\ \psi_2 = \dfrac{3^{b_2}}{2^{b_2}+2}\left(\left|\dfrac{c_2^2 + c_3^2}{3}\right|^{b_2} + \left|\dfrac{c_3^2}{3}\right|^{b_2} + \left|\dfrac{c_2^2}{3}\right|^{b_2}\right)^{1/b_2} \\ \alpha_1 + \alpha_2 = 1 \end{cases} \tag{4.3}$$

Table 4.1 Central values and variation ranges for each parameter.

α_1	a	b_1	b_2	c_1^1	c_2^1
0.72(0~1)	0.16(0~0.5)	13.00(10~16)	8.41(5~15)	1.06(0~1.5)	1.10(0~1.5)
c_3^1	c_4^1	c_1^2	c_2^2	c_3^2	c_4^2
0.82(0~1.5)	0.95(0~1.5)	0.75(0~1.5)	0.47(0~1.5)	0.78(0~1.5)	0.62(0~1.5)

Table 4.2 Identified B&B parameters.

$Y_0\,(MPa)$	α_1	a	b_1	b_2	c_1^1	c_2^1
109.8	0.886	0.255	13.558	10.195	0.924	0.892
η	c_3^1	c_4^1	c_1^2	c_2^2	c_3^2	c_4^2
0.745	0.533	0.6	0.42	0.291	1.27	0.785

The prediction of principal strains and strain path ratios for the different directions are shown in Fig. 4.5 and compared with the experimental data. According to these figures, there is a good agreement between experiments and numerical simulations for the three directions.

Fig. 4.6 gives a comparison between the two yield contours plotted in the in-plane principal stresses $(\sigma_{11}, \sigma_{22})$ plane with parameters of B&B model obtained from the first method, and with the new parameters obtained from the above method. There is a small difference between these two contours. For the equi-biaxial tensile state, the values for these two contours are very close, indicating a similar yield stress under biaxial stretching.

According to the aforementioned analysis, the parameters of the yield criterion obtained from the improved identification method permit a better prediction of principal strains along the different strain paths. This method will be used hereafter to investigate the anisotropic behavior of AA6061 under different temperatures and strain rates.

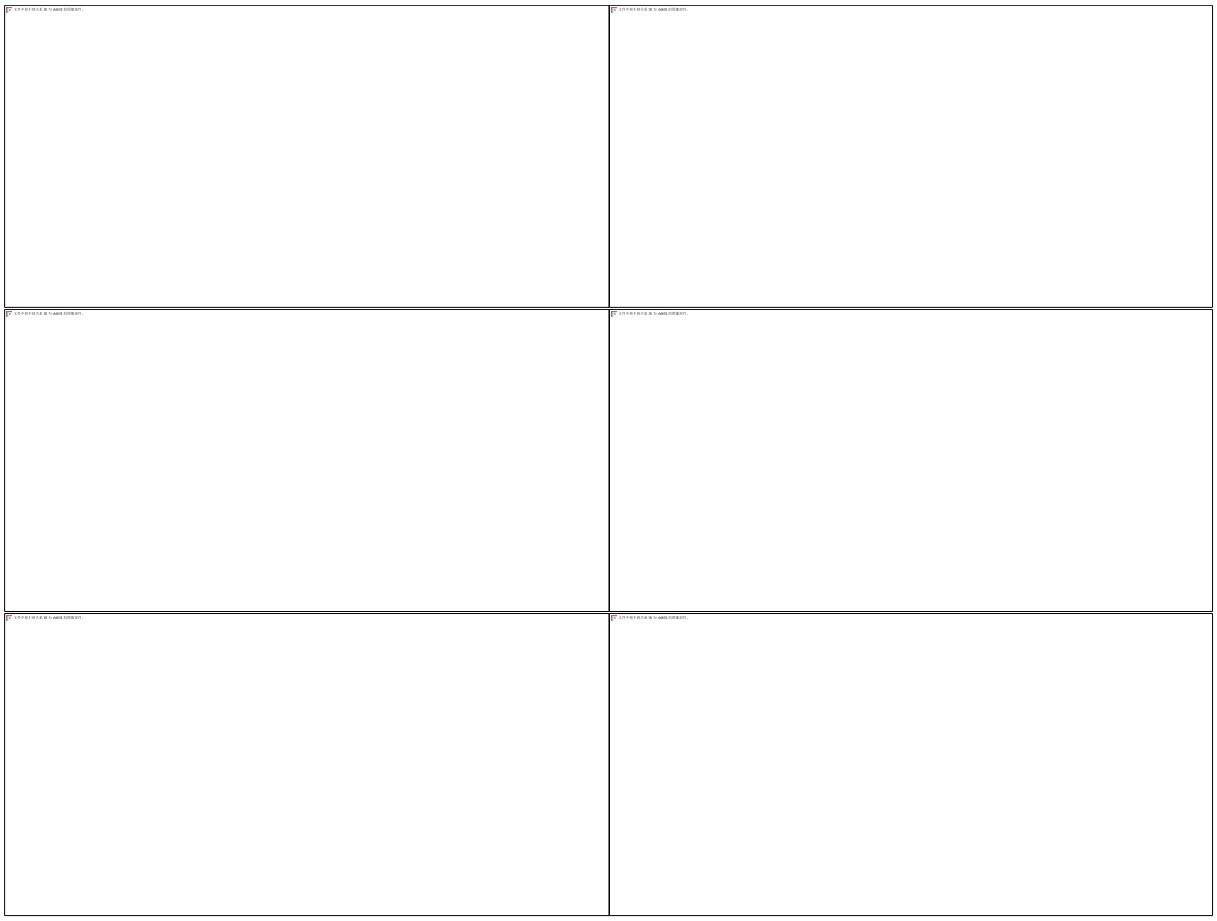

Fig. 4.5 Prediction of principal strains and strain path ratios along different directions: (a) longitudinal; (b) transversal; (c) diagonal.

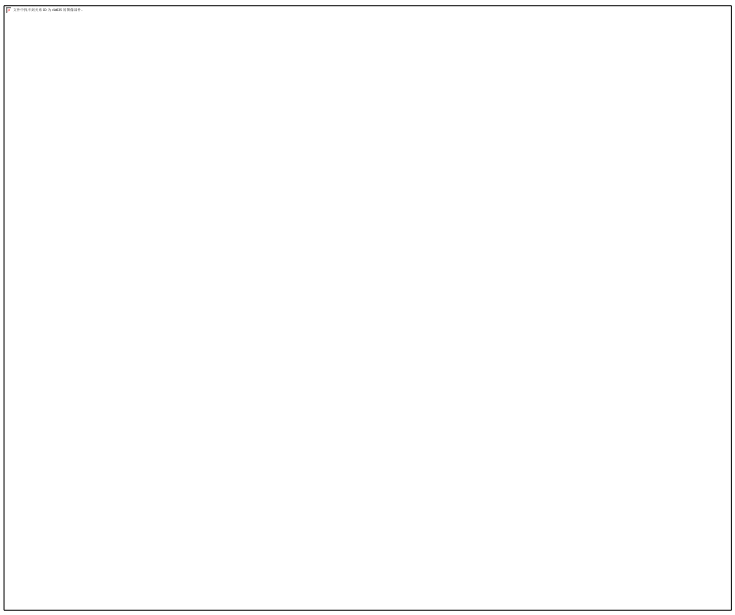

Fig. 4.6 Comparison of the two yield contours for AA5086 with the two different parameter sets: previous and improved method

4.3 Anisotropic plastic behavior of AA6061

4.3.1 Experimental database

The cruciform specimen used in this study required a concentrated strain field at the central gauge area. As shown in Fig. 4.7, a cruciform specimen with a radius of 5 mm between arms was chosen. This specimen doesn't have a reduced thickness at the central area, which permits to apply the method to all the sheets, regardless of the value of the thickness.

Fig. 4.7 Geometry of the cruciform specimen. [116]

4.3.1.1 Experimental data

The biaxial tensile tests for AA6061 with the cut type shape of specimen have been carried out at different tensile velocities (1mm/s and 200mm/s) and different temperatures (-40°C, ambient and 160°C). A constant velocity ratio $v_x/v_y = 1$ is applied for each arm of the cruciform specimen. The rolling direction of the sheet is associated to the y direction of the biaxial tensile device.

The main acquisition parameters of the camera and load sensors (strain-gauge load cells) are given in Table. 4.3.

Table 4.3 Main characteristics of acquisition

Test velocity (mm/s)	Camera			Load sensor acquisition rate (Hz)
	Image resolution (pixel)	Acquisition rate (fps)	Shutter speed (s)	
1	1024×1024	250	1/800	250
200	1024×1024	3000	1/3000	5000

Fig. 4.8 shows the measurement of forces along each axis of the specimen for the different conditions. It can be seen that the tensile forces along the longitudinal and transversal directions are well synchronized for all the conditions. The difference between ultimate forces at ambient temperature and -40°C is less than 3% for both quasi-static (1mm/s) and dynamic conditions

(200mm/s). However, the ultimate forces at 160°C are about 24% lower than the ones at ambient temperature for quasi-static condition (Fig. 4.8a) and 12% lower for dynamic conditions (Fig. 4.8b).

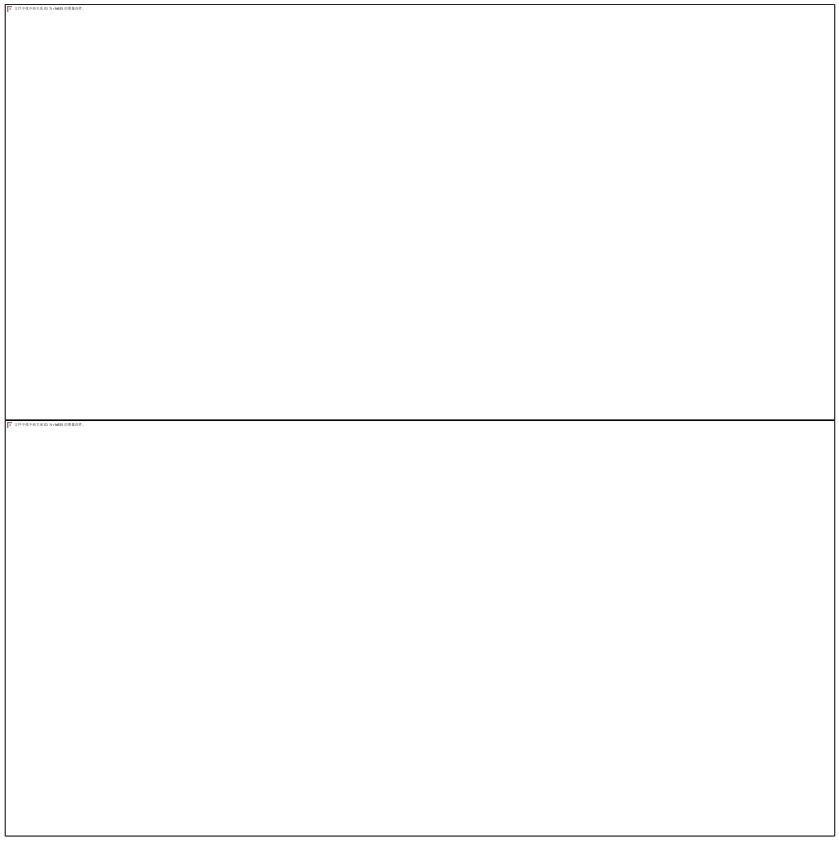

Fig. 4.8 Evolution of loads along the two directions for each condition

The evolution of principal strains of AA6061 along longitudinal, transversal and diagonal direction for the different conditions are calculated with the GOM digital image correlation software.

Fig. 4.9 shows an image of the cruciform specimen at the initial state. The square area in blue with a size of approximately 25×25 mm^2 at the central gauge of the specimen is selected to calculate the principal strains. The size of the subsets for correlation is 32×32 pixels and the distance between each point is 16 pixels (scale of 0.038mm/pixel), leading to a number of about 2200 points for the calculation of the strain field.

The lines x1 and x2 correspond to the longitudinal path, y1 and y2 correspond to the transversal path (rolling direction). The lines 1 to 4 are associated to the diagonal path. The experimental data used during the parameter identification stage correspond to the average of principal strains along the different paths, respectively. Experimental results for all the conditions are presented below.

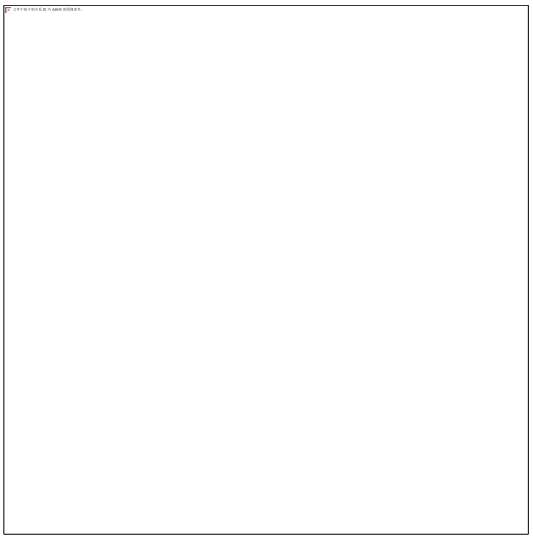

Fig. 4.9 Measurement area and visualization of specified paths.

4.3.1.2 Principal strains at the central gauge area

- **Tensile speed of 1mm/s at ambient temperature.**

For a tensile speed of 1mm/s (strain rate around $0.1s^{-1}$) along each axis at ambient temperature, 1540 images were recorded before the rupture (total time of 6.16s). The values of the principal strains at the time corresponding to 80% of the total time are selected for the identification process. The selection of this time, far enough from the rupture, avoids strain localizations due to the onset of necking. The evolution of the principal strains is shown in Fig. 4.10.

For all the directions, the evolution of strain values along the different paths shows a very good repeatability of the results. The selection of the average of these strain values for the identification procedure is consistent.

The evolution of strain path ratios for each direction, defined as the ratio $\varepsilon_2/\varepsilon_1$, is calculated with the average principal strains and presented in Fig. 4.11. It can be clearly seen that the strain state varies from nearly equi-biaxial tensile strain state (about 0.98) in the center of the specimen to a plane strain state (about 0.07) along longitudinal and transversal direction. For the diagonal direction, a near tensile strain state is reached with the farthest point from the center (strain path ratio of -0.2).

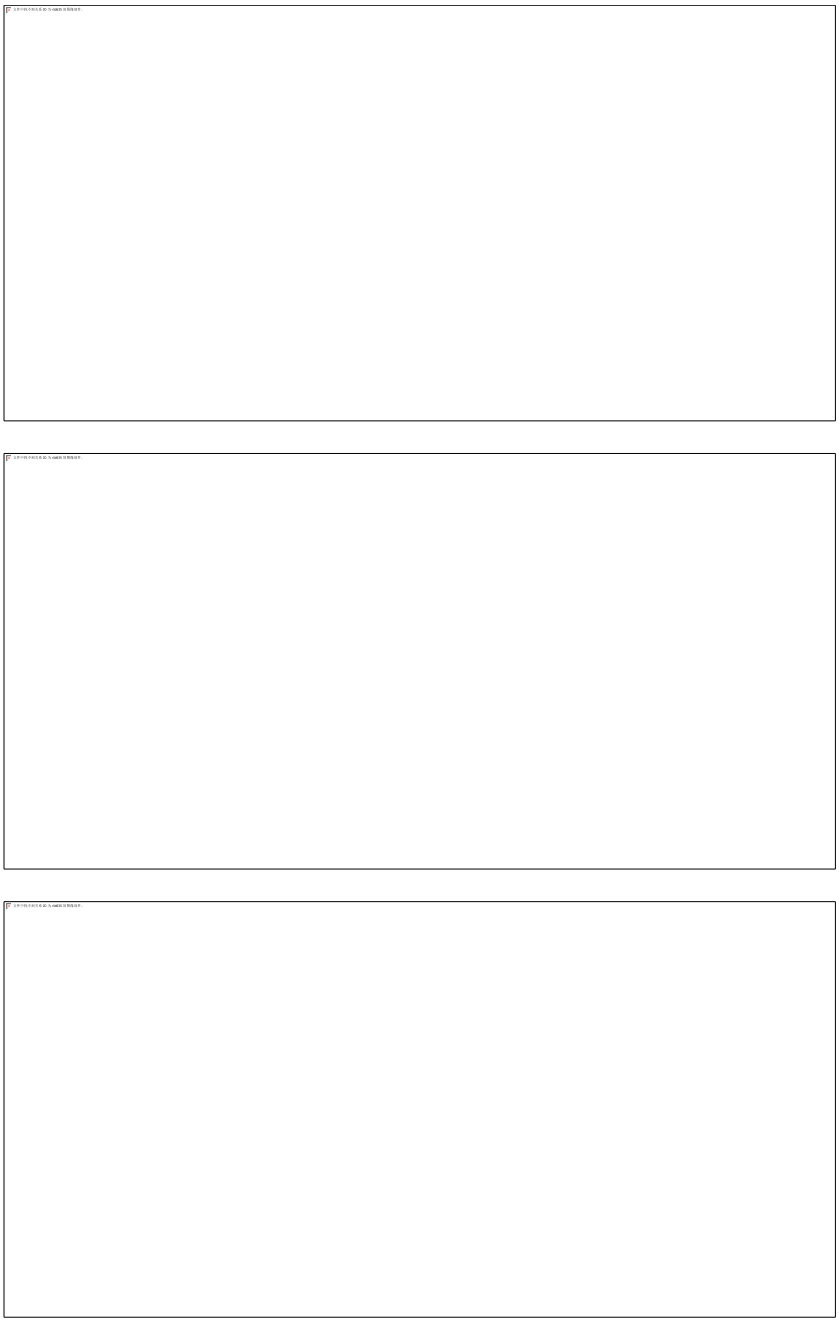

Fig. 4.10 Evolution of principal strains along the three directions: (a) longitudinal; (b) transversal; (c) diagonal.

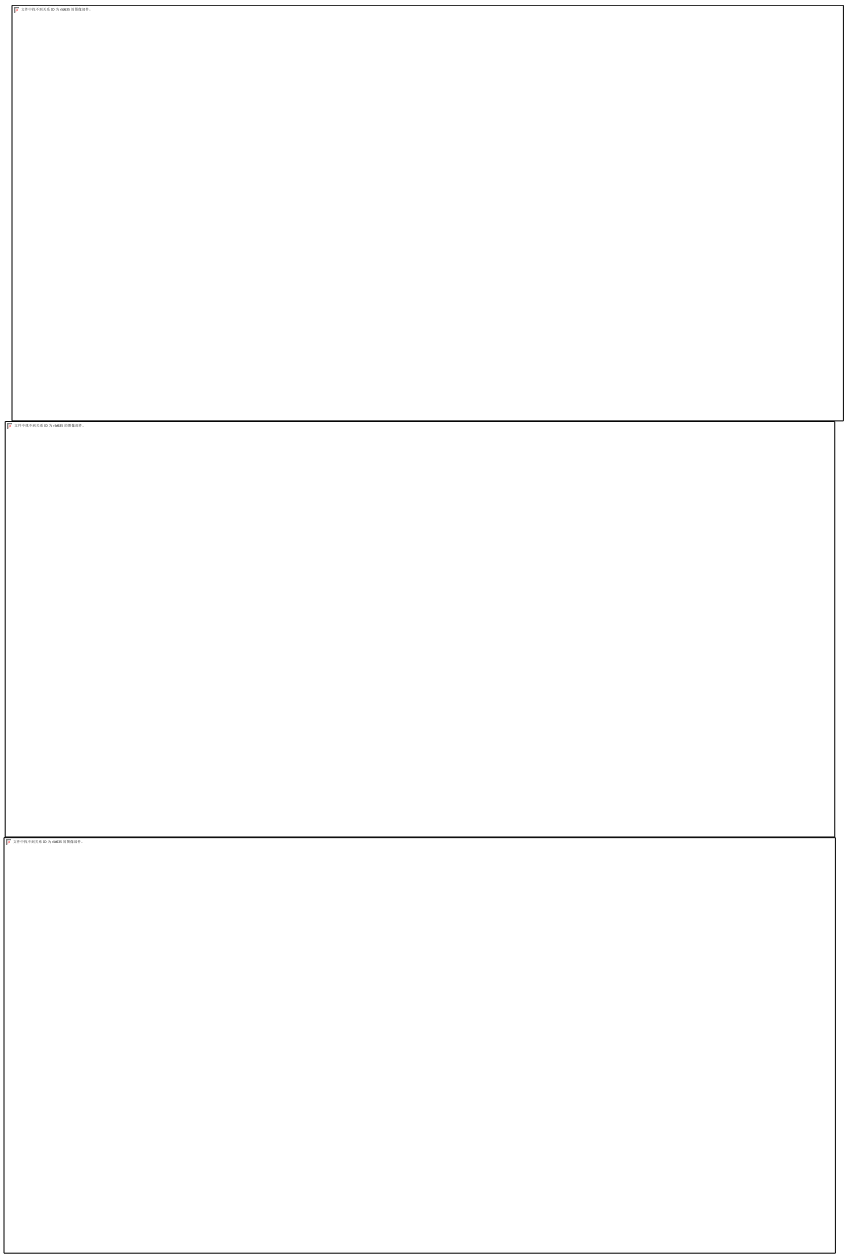

Fig. 4.11 Evolution of strain path ratios along the three directions: (a) longitudinal; (b) transversal; (c) diagonal.

The experimental forces and principal strains along the three specific paths for this condition constitute the experimental database for the parameter identification process.

Also, with the same calculation method presented above, the experimental data for the other temperatures and tensile velocities are obtained.

- **Tensile speed of 1mm/s at -40°C**

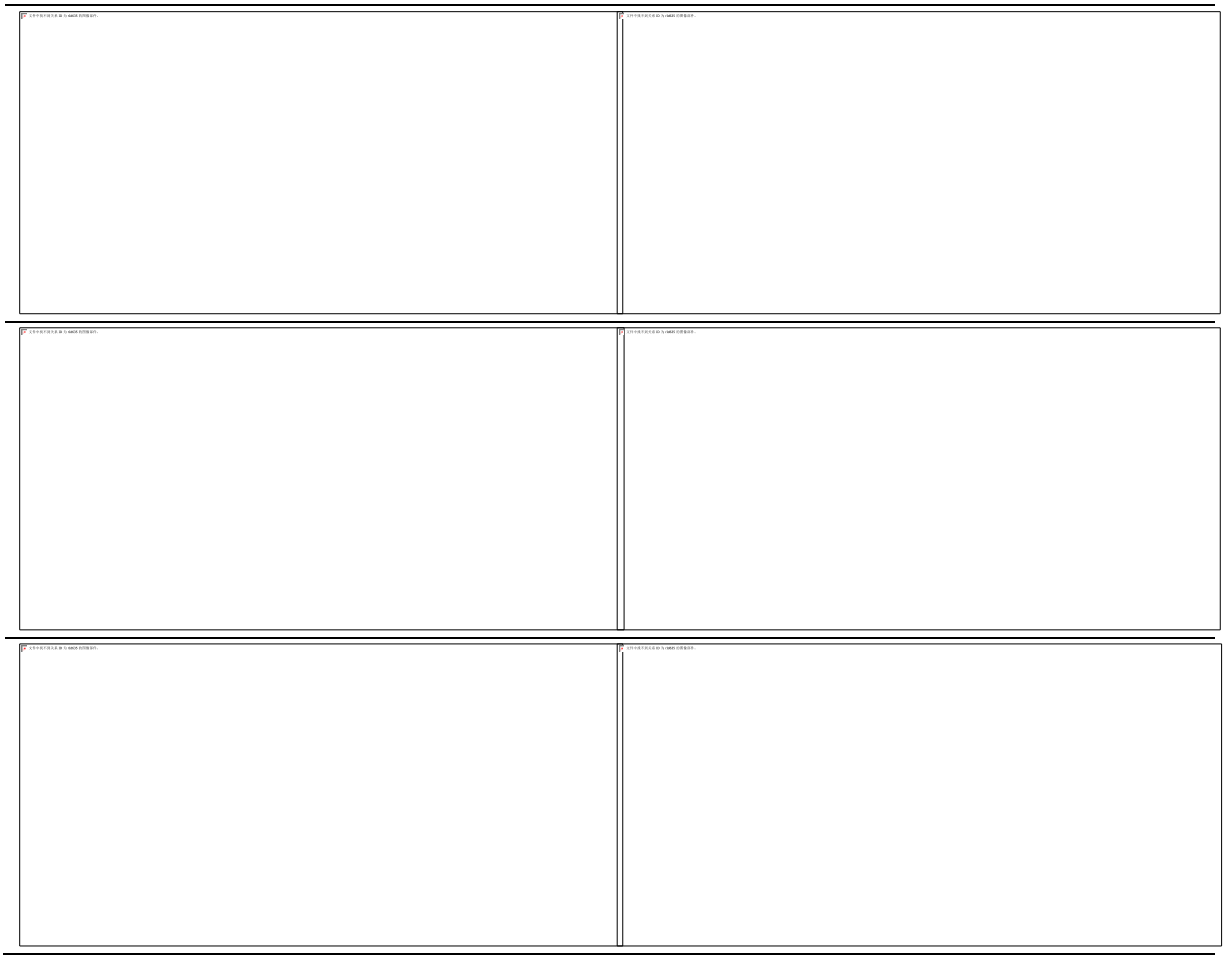

Fig. 4.12 Evolution of principal strains and strain path ratios along the three directions: (a) longitudinal; (b) transversal; (c) diagonal.Tensile speed of 1mm/s at 160°C

The evolutions of principal strains for the different paths are quite similar along the three directions, indicating a symmetrical strain field distribution on the gauge area of the specimen, regardless of the condition of strain rate or temperature. The selected strain values at the center point are between 0.013 and 0.02. The total time and the selected time for the different conditions are summarized in Table 4.4.

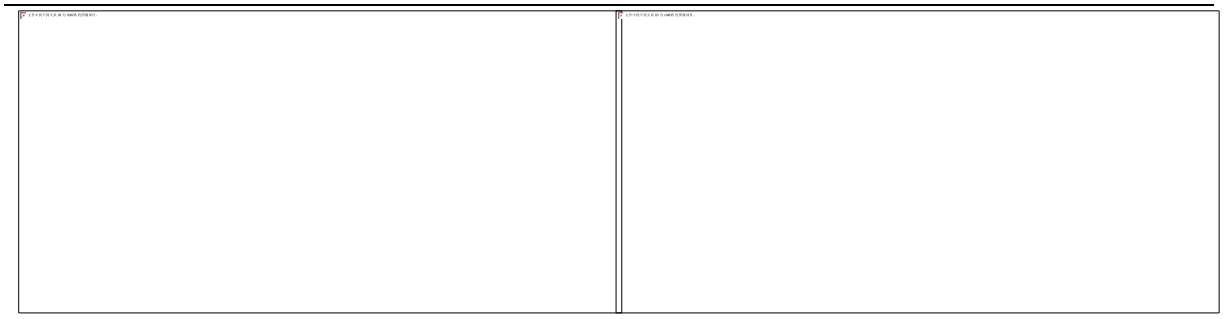

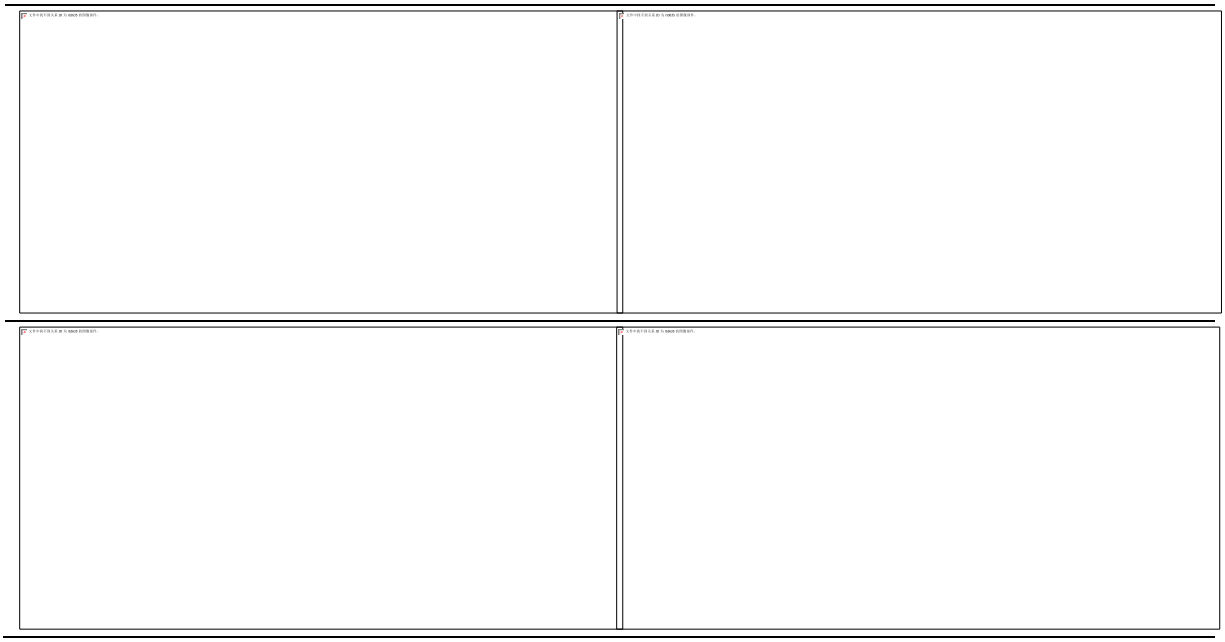

Fig. 4.13 Evolution of principal strains and strain path ratios along the three directions: (a) longitudinal; (b) transversal; (c) diagonal.

- **Tensile speed of 200mm/s at -40°C**

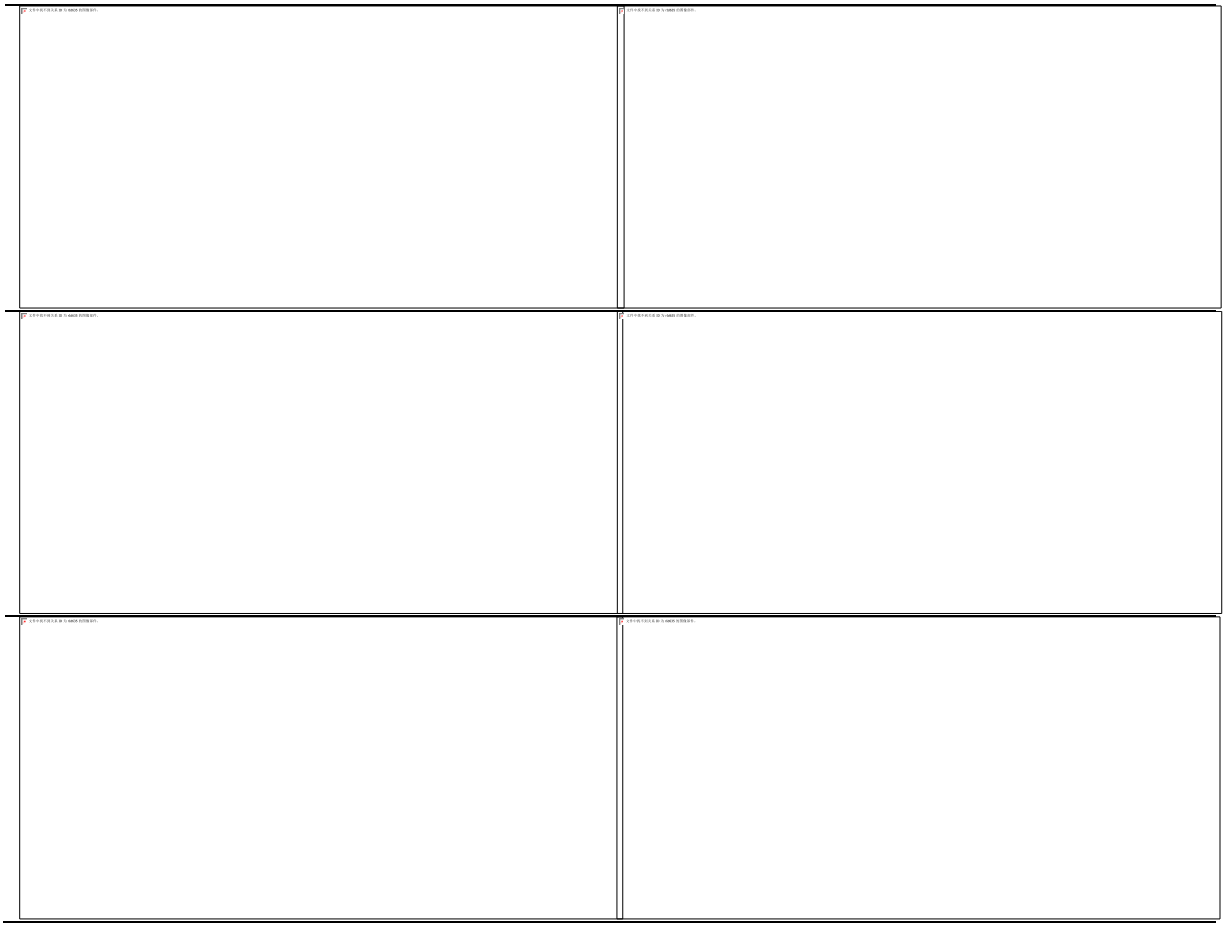

Fig. 4.14 Evolution of principal strains and strain path ratios along the three directions: (a) longitudinal; (b) transversal; (c) diagonal.

- **Tensile speed of 200mm/s at ambient temperature**

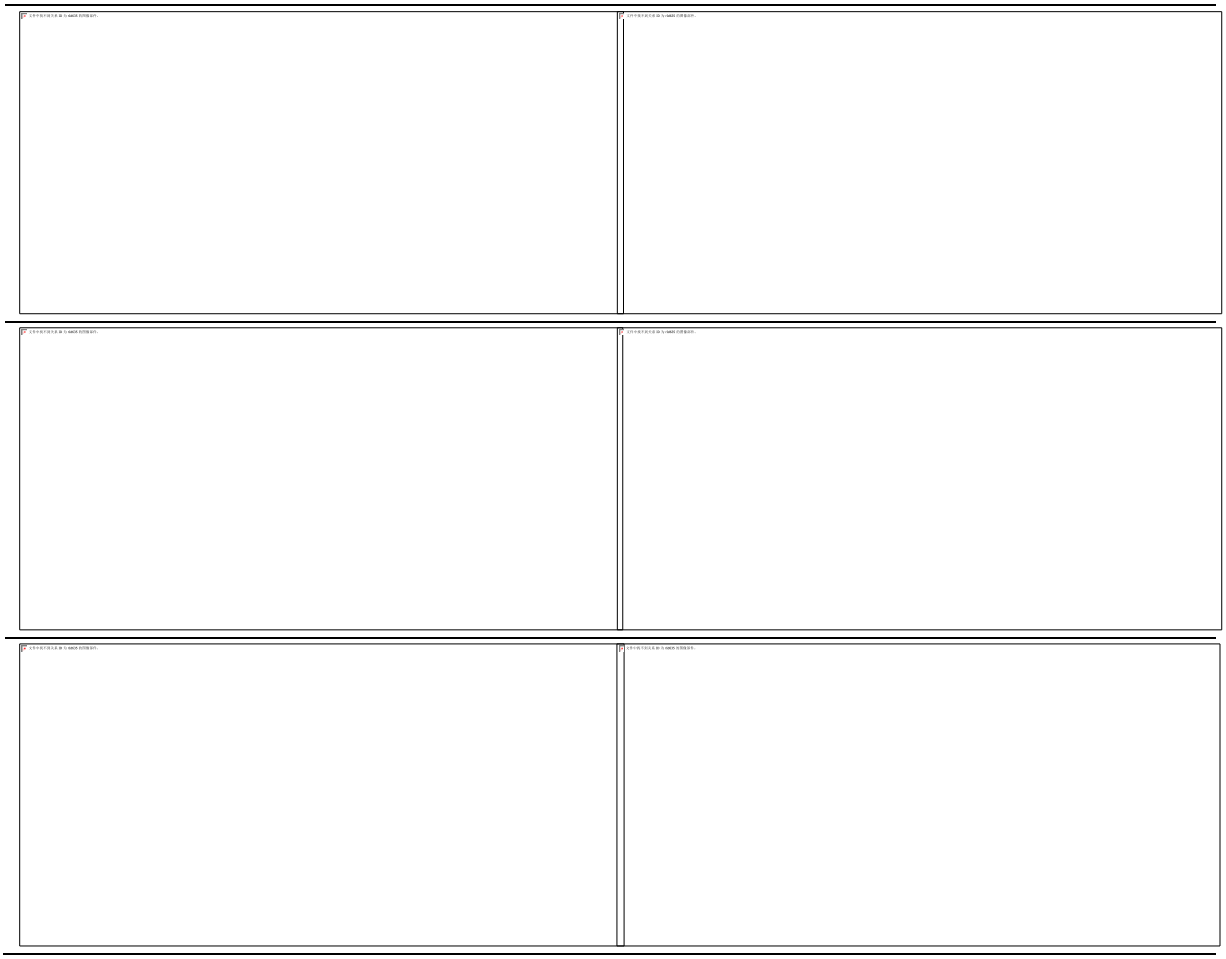

Fig. 4.15 Evolution of principal strains and strain path ratios along the three directions: (a) longitudinal; (b) transversal; (c) diagonal.

- **Tensile speed of 200mm/s at 160°C.**

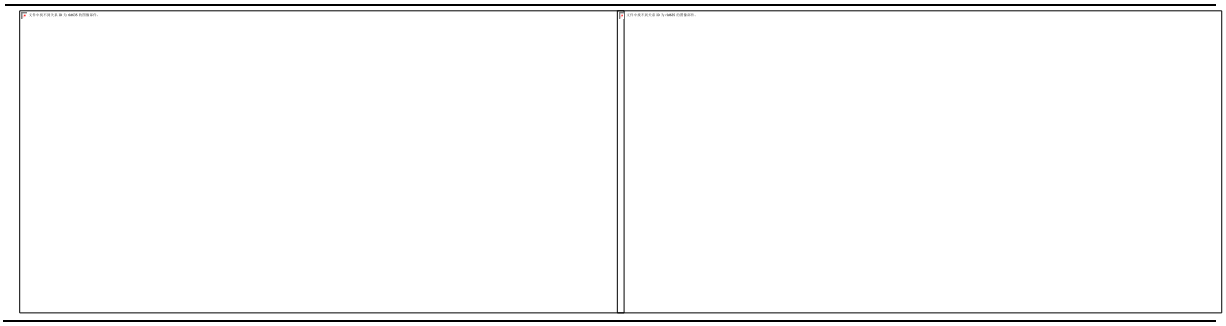

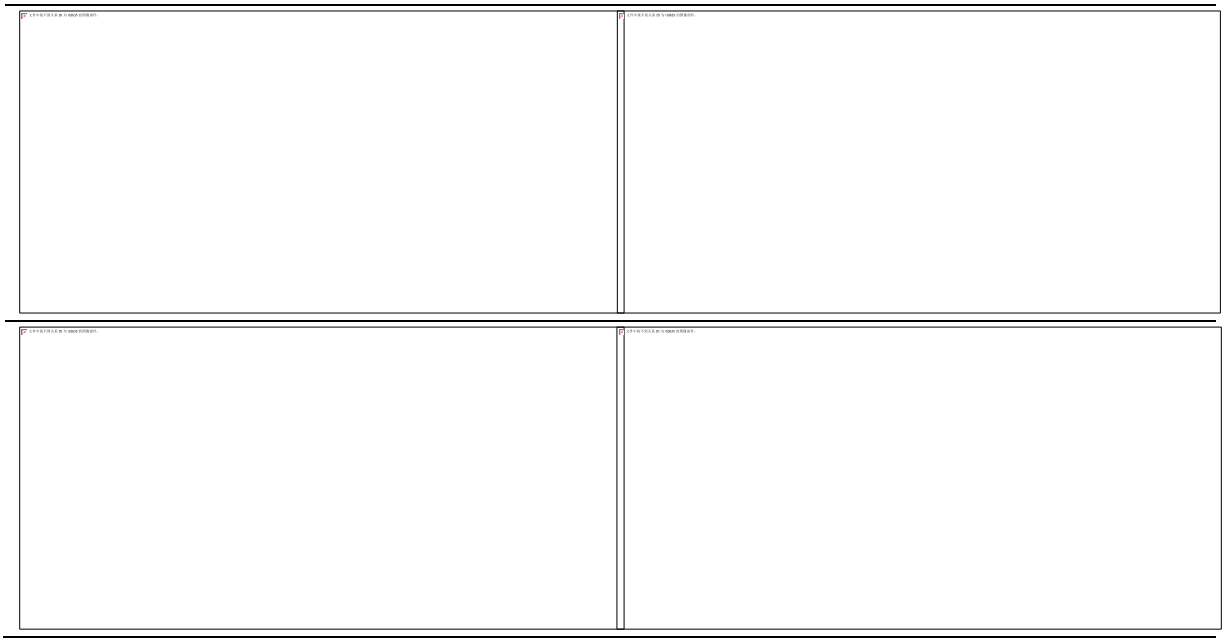

Fig. 4.16 Evolution of principal strains and strain path ratios along the three directions: (a) longitudinal; (b) transversal; (c) diagonal.

Table 4.4 Summarized of the analysis time for each condition.

v (mm/s), T (°C)	Total time (s)	Analysis time (s)
1mm/s, -40°C	6.06	5
1mm/s, ambient	6.16	5
1mm/s, 160°C	4.692	3.5
200mm/s, -40°C	0.044	0.36
200mm/s, ambient	0.043	0.35
200mm/s, 160°C	0.04	0.35

4.3.2 Identification of yield criterion

The parameters of Bron and Besson yield criterion for AA6061 are identified by using the experimental data from the test performed at 1mm/s and at ambient temperature. Due to the low strain values reached during the test, the results are not very sensitive to the hardening type chosen for the identification procedure by inverse analysis. For the same conditions of temperature and strain rate, the hardening is well represented by a simple formulation based on a Voce hardening law (Eq. (4.4)). The calibrated parameters are presented in Table 4.5.

$$\bar{\sigma} = \sigma_s + k \cdot \left(1 - e^{-n \cdot \bar{\varepsilon}_p}\right) \tag{4.4}$$

Table 4.5 Identified parameters for Voce law.

σ_s (MPa)	*k* (MPa)	*n*
166.16	191.3	13.32

The identified parameters of the Bron and Besson yield criterion are presented in Table 4.6. The prediction of principal strains and strain path ratios for Bron and Besson are compared with the prediction of Von-Mises model and experimental data (Fig. 4.17). It can be seen that, compared with the isotropic model, the anisotropic model gives a better description of strain evolutions and strain path ratios along the different directions. Considering the evolutions of major and minor strains, The Bron and Besson yield model gives an excellent match to the experimental data for the three directions. Also, a good agreement is observed for the strain path ratios along the three directions.

Table 4.6 Identified parameters for Bron and Besson yield criterion.

Y_0(MPa)	α_1	a	b_1	b_2	c_1^1	c_2^1
120.5	0.901	0.508	10.075	4.41	0.863	0.773
η	c_3^1	c_4^1	c_1^2	c_2^2	c_3^2	c_4^2
0.725	0.61	0.573	0.155	0.453	1.494	0.946

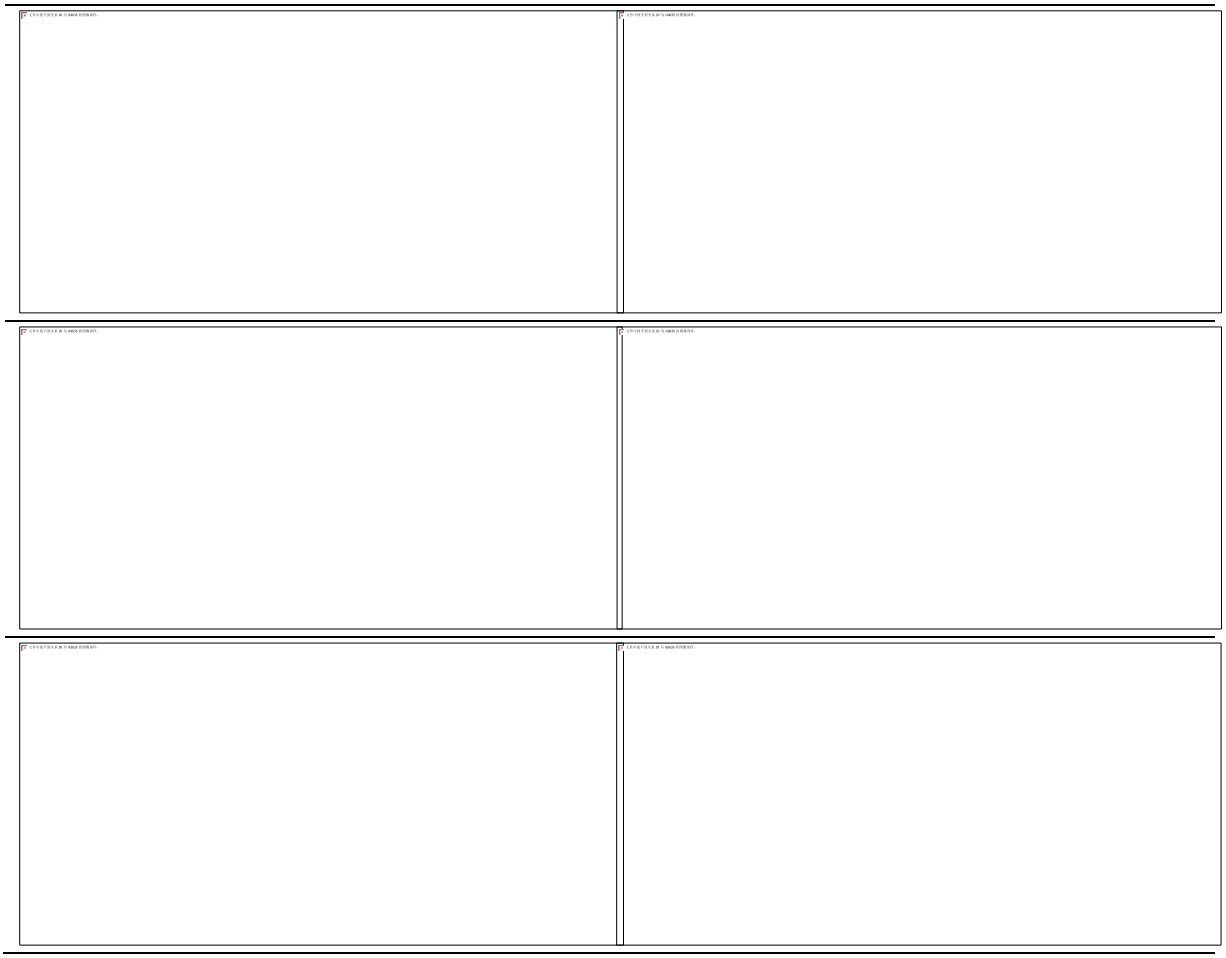

Fig. 4.17 Prediction of principal strains and strain path ratios along the different strain paths (1mm/s and ambient temperature) and comparison with experimental data: (a) longitudinal; (b) transversal; (c) diagonal.

In order to check the reliability of the set of parameters, the comparison of principal strains is performed at a smaller time point (t = 4s) (Fig. 4.18). The agreement between predictive and experimental results is also very good at this time. It can be concluded that the Bron and Besson

yield criterion identified by the proposed method is efficient to predict the strain fields for AA6061 under quasi-static condition and room temperature.

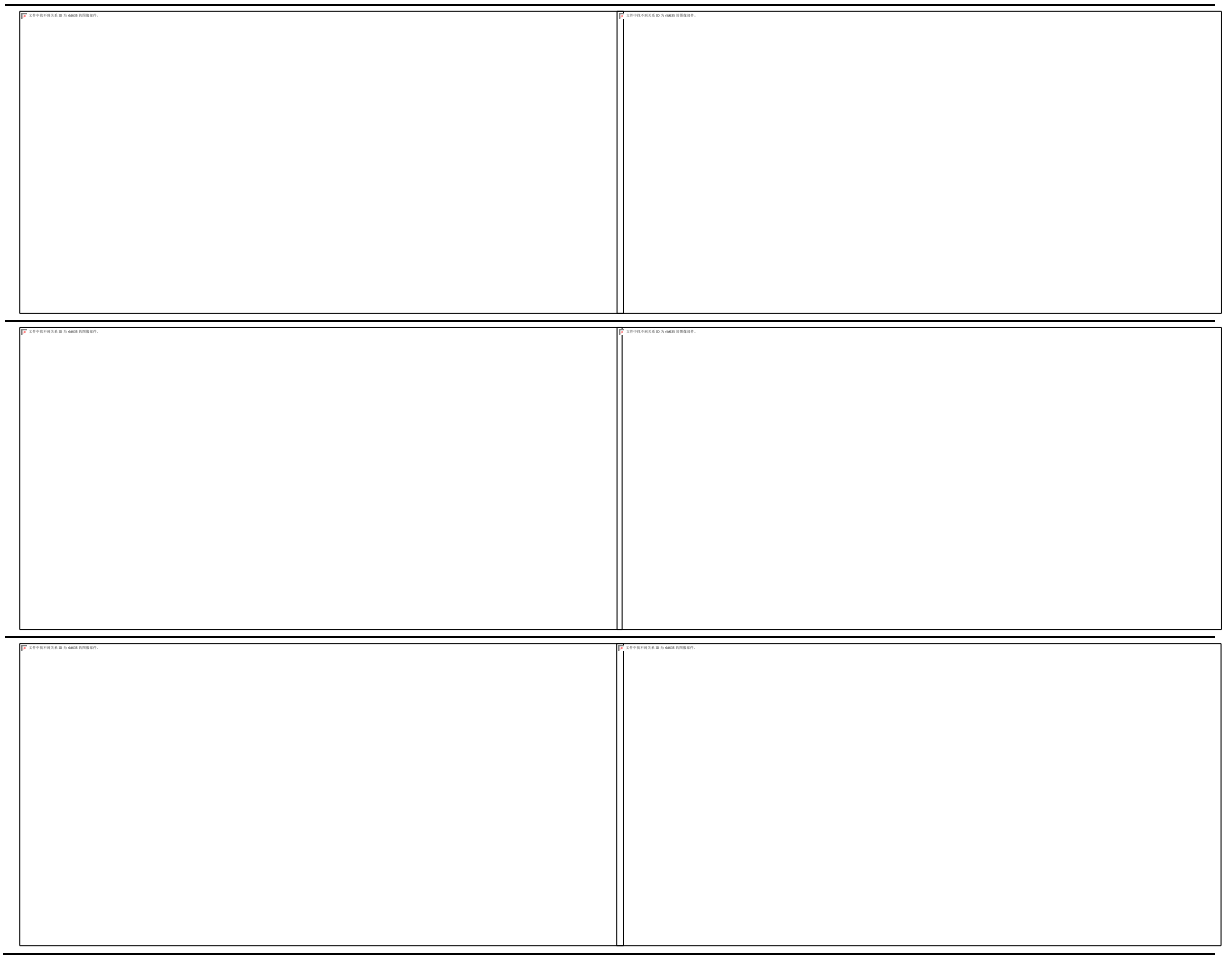

Fig. 4.18 Prediction of principal strains and strain path ratios at the time t = 4s: (a) longitudinal; (b) transversal; (c) diagonal.

Fig. 4.19 gives a comparison between the yield surfaces predicted by the identified Bron and Besson yield criterion and by the isotropic Mises yield criterion (σ_0=166.16MPa). It is seen that the Bron and Besson yield locus is inside the Mises one under biaxial tension, indicating that the yield stress under equi-biaxial stretching is lower than the one under uniaxial tension. This tendency is confirmed by the results of the identification of the hardening model in Chapter 3. At the center of the cruciform specimen, where an equi-biaxial strain state is mainly observed, the use of a Mises model gives a value of 148.55MPa for the yield stress.

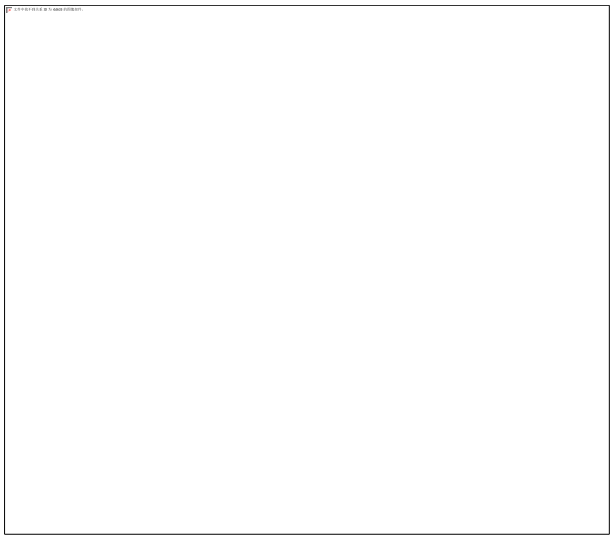

Fig. 4.19 Initial yield contours obtained by B&B yield model and Mises model.

4.4 Sensitivity to temperature and strain rate for yield criterion

The temperature and strain rate dependent hardening model which has been identified in Chapter 3 is used now and combined with the identified Bron and Besson yield criterion. By means of FE simulations of the equi-biaxial tensile test presented in this chapter, the main objective is to verify if the yield criterion characterized at ambient temperature and for quasi-static conditions, is able to predict the strain evolutions for the other conditions.

The experimental forces measured from the experimental equi-biaxial tensile tests for the different temperatures and tensile velocities are imposed as boundary conditions in the FE model of the equi-biaxial tensile test. Based on the experimental results, a low strain level is observed in the center gauge of the specimen, which indicates that the plastic deformation has little contribution on the self-heating of the specimen. Hence, we consider that the temperature in the FE model is constant and the numerical simulation can be performed in a static general procedure.

For the comparison of the principal strains and strain path ratios along longitudinal, transversal and diagonal profiles in the following figures (Fig. 4.20 to 4.25), two hardening models are considered with the identified Bron and Besson yield model:

- **P1 model**: Bron and Besson yield criterion combined with the Voce hardening model (Eq. 4.4);
- **P2 model**: Bron and Besson yield criterion combined with the V_1 hardening model (Eq. 2.9), which is sensitive to temperature and strain rate effect and has been identified in previous Chapter (Table 2.7).

Firstly, Fig. 4.20 gives a comparison between the principal strain evolutions and strain path ratios for a tensile speed of 1mm/s and at ambient temperature The P2 model gives almost the same predictions than the ones of P1 model. It can be concluded that, if the Bron and Besson yield criterion is preliminarily well-defined, changing the expression of the hardening model

does not affect the predictive result.

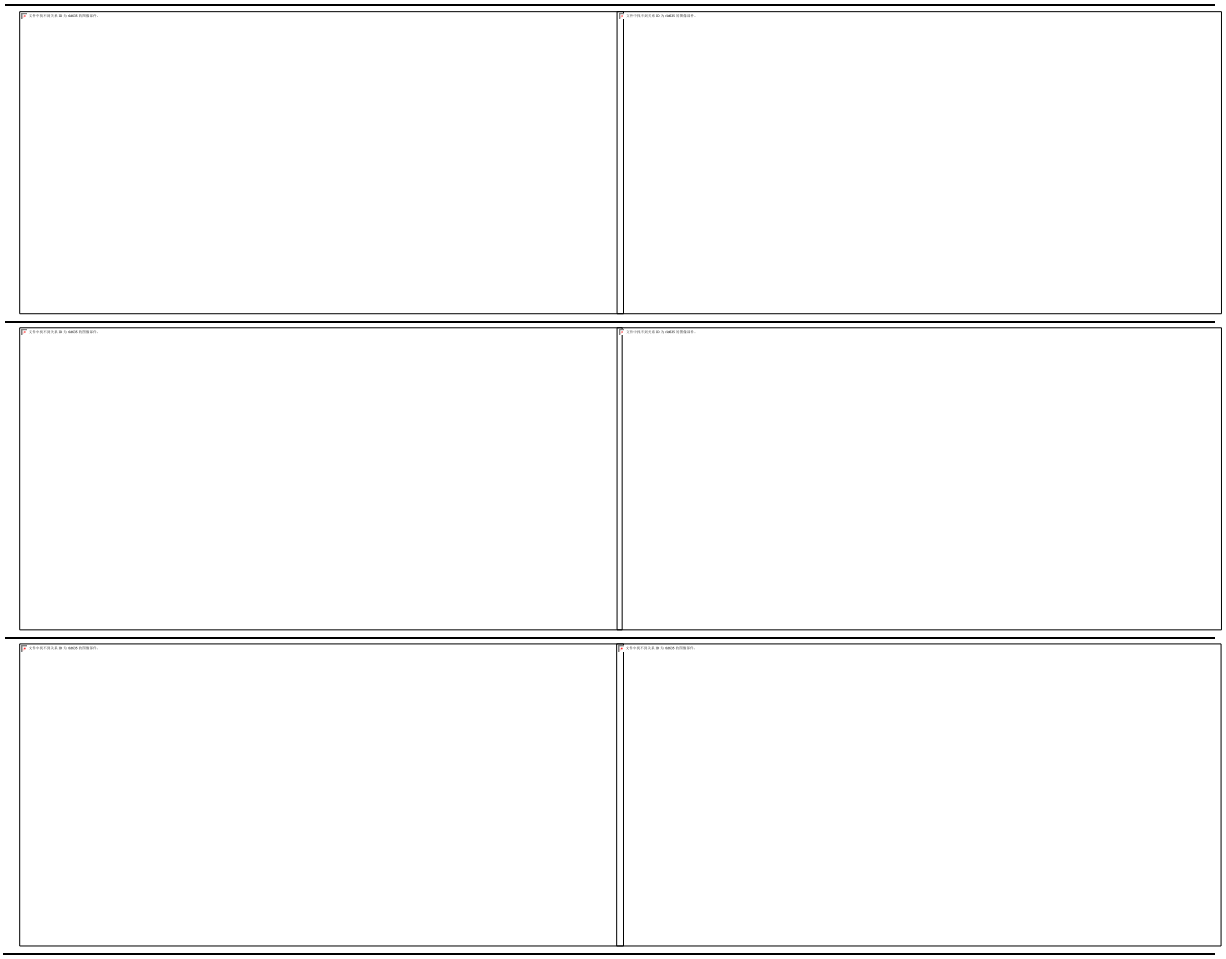

Fig. 4.20 Prediction of principal strains and strain path ratios along the different directions (1mm/s and ambient temperature) and comparison with experimental data: (a) longitudinal; (b) transversal; (c) diagonal.

For the temperature of 160°C, for a tensile speed of 1mm/s, both the P1 and P2 model give an underestimation of the experimental strains, while the predictions of P2 are closer to the experimental ones (Fig 4.21). Similarly, for the strain path ratio, the P2 model presents a better agreement to experiments than the P1 model. It shows that the hardening model including temperature sensitivity is better to describe the plastic behavior under high temperatures. Nevertheless, introducing the temperature effect only in the hardening model seems not to be sufficient to give a correct description of the strain evolutions. .

For the dynamic condition (200mm/s) at ambient temperature (Fig 4.22), it can be seen that the predictions of principal strains of the P1 model are underestimated, compared with the experimental principal strains. The P2 model correctly describes the major strains along the three directions; however, the minor strains are lower than the experimental curves, especially at the center area.

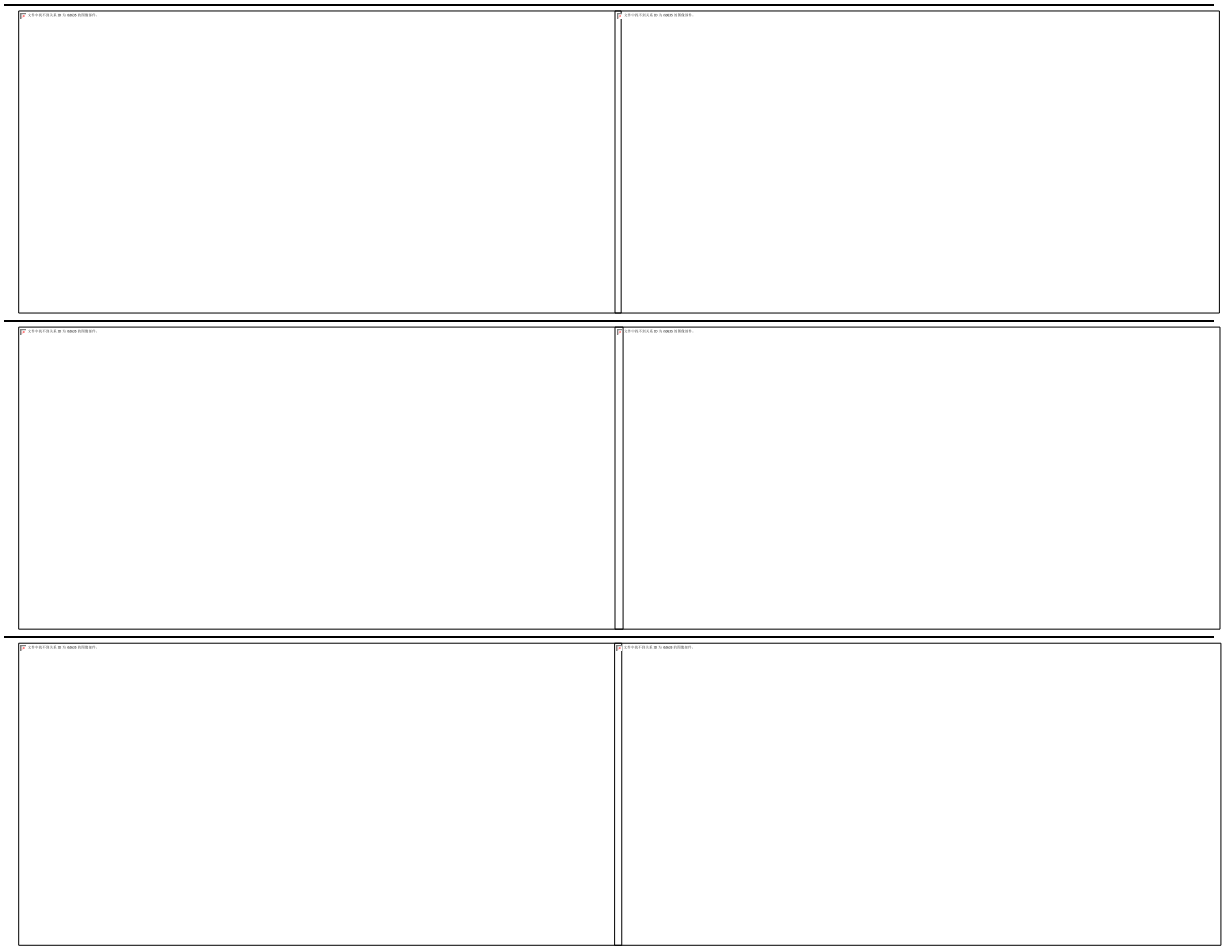

Fig. 4.21 Prediction of principal strains and strain path ratios along the different directions (1mm/s and 160°C) and comparison with experimental data: (a) longitudinal; (b) transversal; (c) diagonal.

For the same tensile speed at 160°C (Fig 4.23), the P1 and P2 models give almost the same predictions for principal strains along the three directions. Predictions are much lower than the experimental results. Similar conclusion than the one from Fig 4.21 can be drawn, introducing the temperature effect only in the hardening model is not sufficient to describe the plastic behavior of the material. In Fig. 4.21, the difference between predictive and experimental results is emphasized by the strain rate effect.

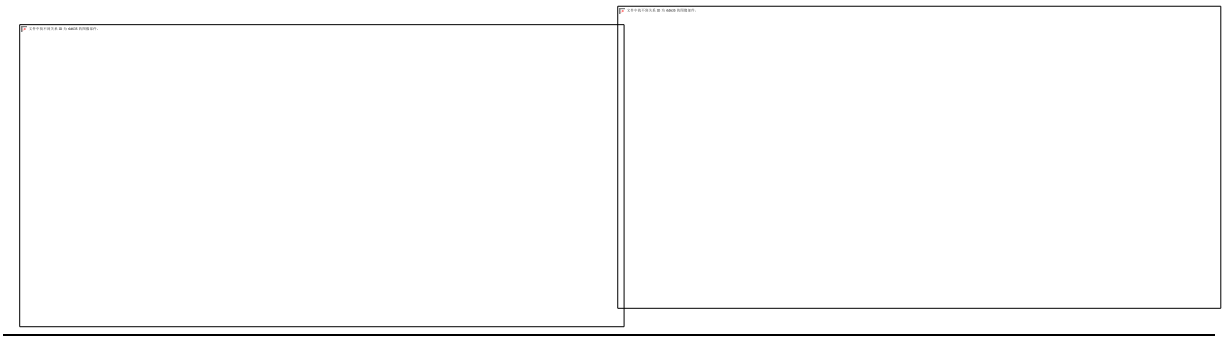

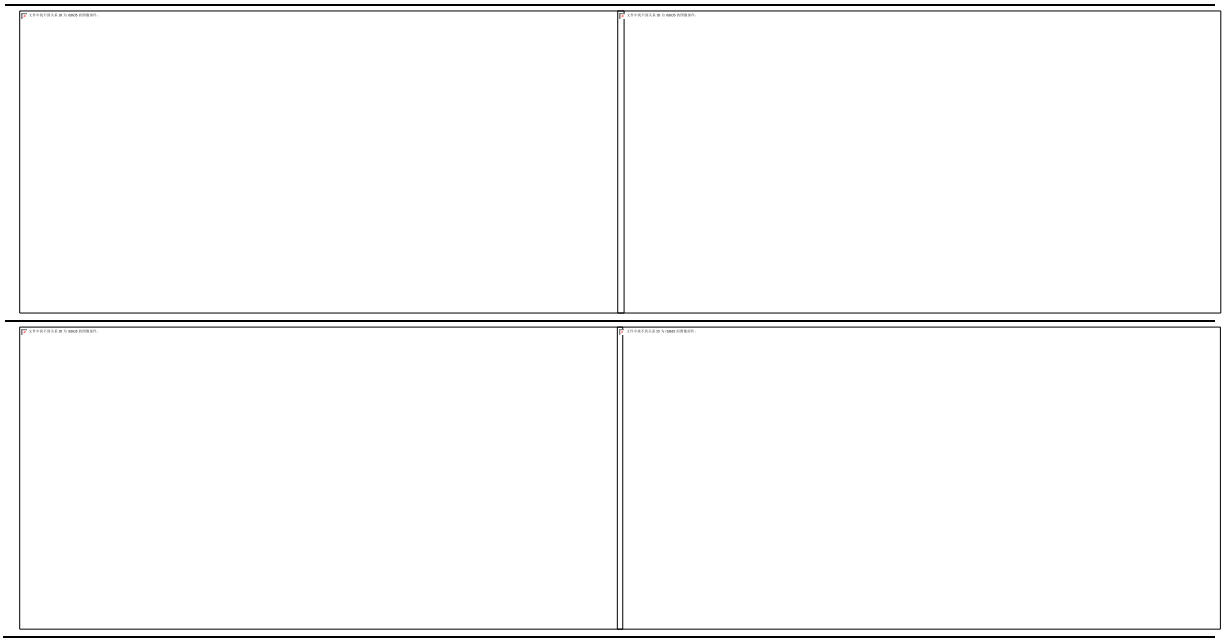

Fig. 4.22 Prediction of principal strains and strain path ratios along the different directions (200mm/s and ambient temperature) and comparison with experimental data: (a) longitudinal; (b) transversal; (c) diagonal.

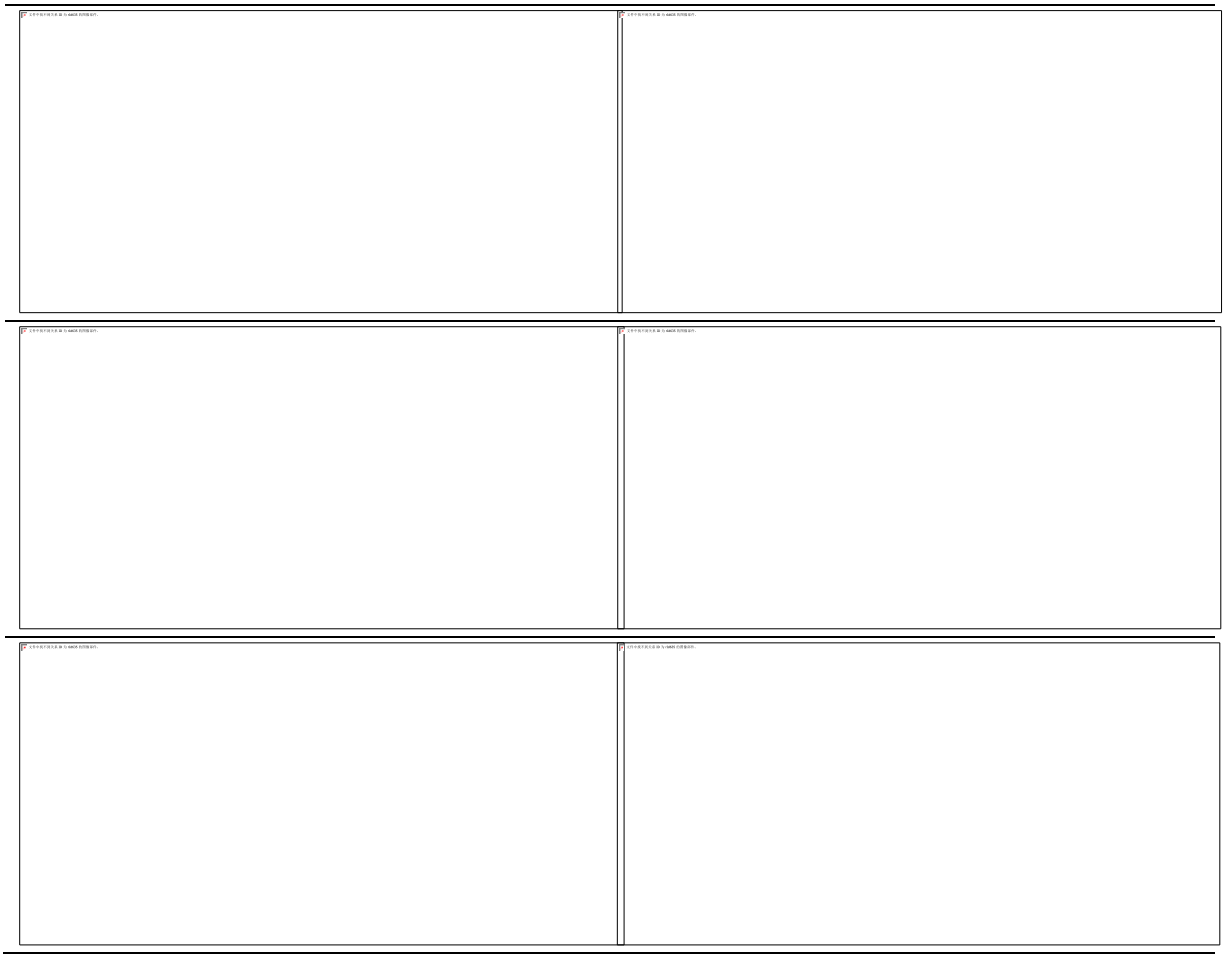

Fig. 4.23 Prediction of principal strains and strain path ratios along the different directions (200mm/s and 160°C) and comparison with experimental data: (a) longitudinal; (b) transversal; (c) diagonal.

Moreover, the constitutive models have been also applied to predict the strain field for the two tensile speeds at the low temperature of -40°C.

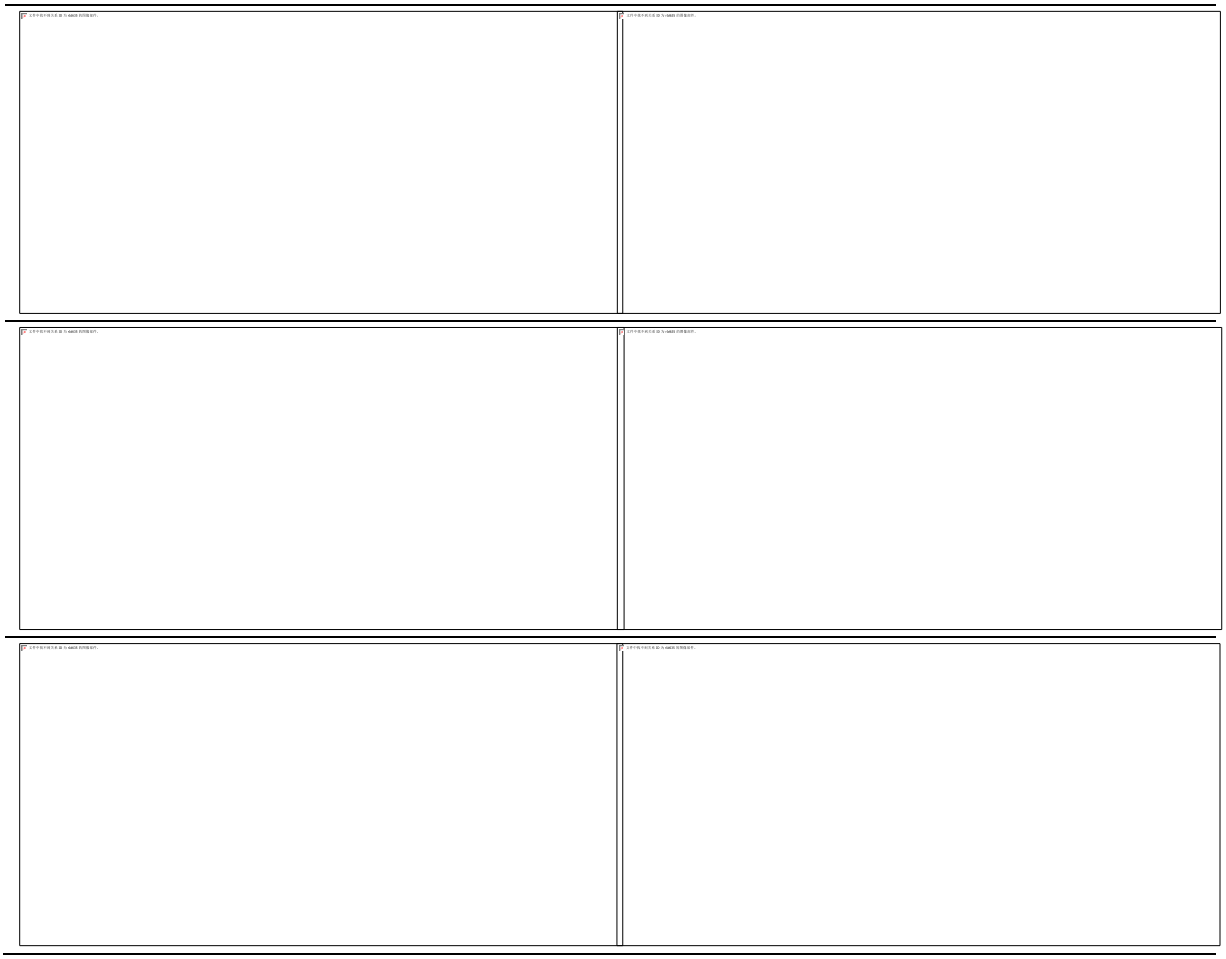

Fig. 4.24 Prediction of principal strains and strain path ratios along the different directions (1mm/s and -40°C) and comparison with experimental data: (a) longitudinal; (b) transversal; (c) diagonal.

Fig. 4.24 gives a comparison between the experimental principal strains and strain path ratios with the predictions from the two constitutive models at the low tensile speed and at -40°C. The P2 model gives a better prediction of the principal strain evolutions than the P1 model, indicating that the hardening model is efficient to describe the flow stress at this temperature. It seems that this temperature has a slight influence on the anisotropy of AA6061.

For the same temperature, but at the high tensile speed of 200mm/s (Fig. 4.25), the predicted major strain at the center point is about 40% higher than the minor strain. Also, the predicted strain path ratio at the center is about 30% lower than the experimental one. By comparing the results from Fig. 4.24 and Fig. 4.25, strain rate seems to have a significant effect on the anisotropy behavior of the material at this temperature since the values of major and minor strains at the center become very different when the strain rate increases.

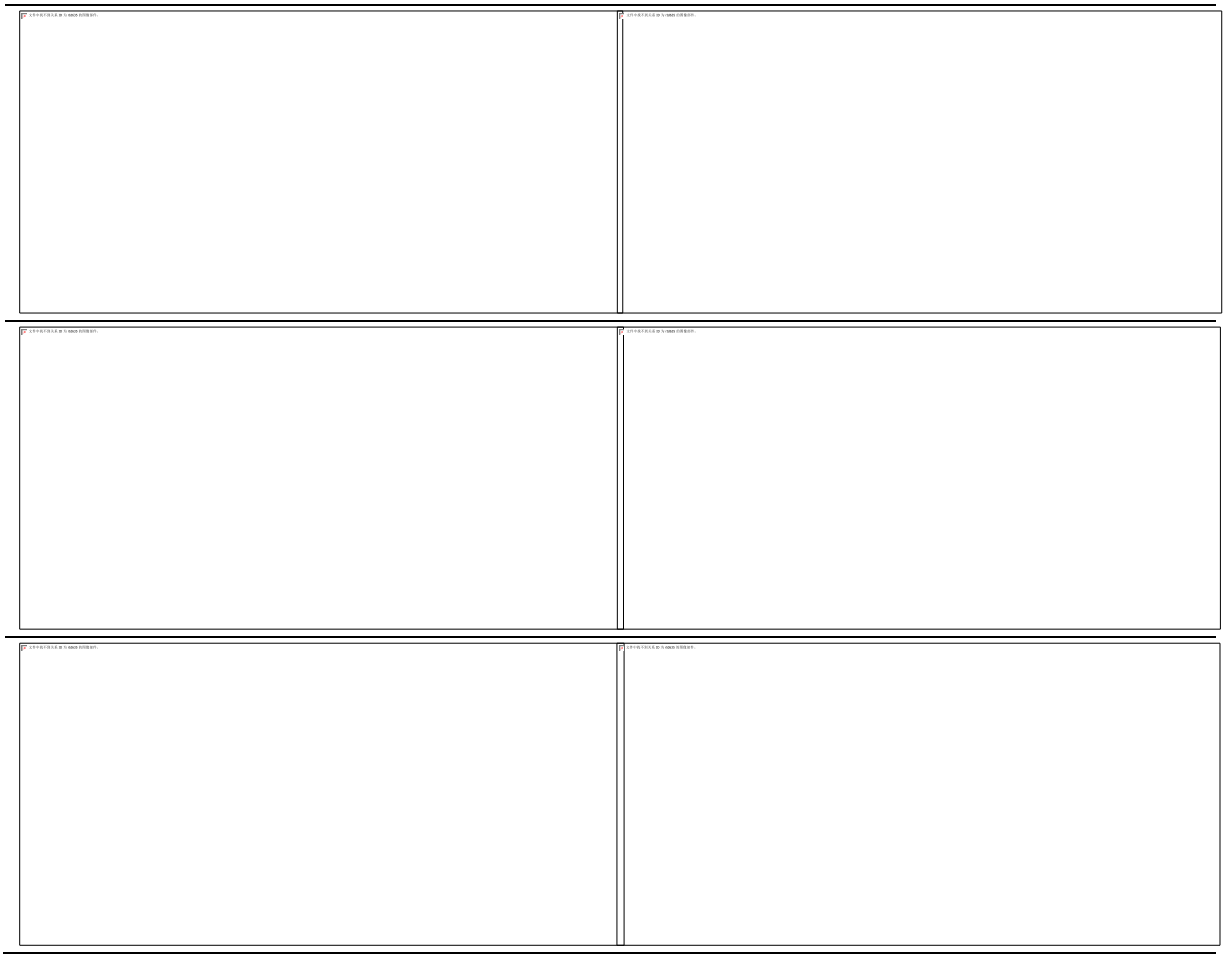

Fig. 4.25 Prediction of principal strain and strain path ratio along different directions at 200mm/s, -40°C and compared with experimental data. (a) longitudinal; (b) transversal; (c) diagonal.

Based on the aforementioned analysis, the Bron and Besson yield criterion coupled with a temperature and strain rate sensitive hardening model can give suitable predictions of strain fields for AA6061 for different ranges of temperatures and strain rates. Nevertheless, it could be interesting to make an identification of the parameters of the Bron and Besson yield criterion for each condition in order to evaluate the influence of temperature and strain rate on the shape of the yield contours.

4.5 Conclusion

The method based on a heterogeneous in-plane biaxial tensile test and a dedicated cruciform specimen is applied to characterize the anisotropic behavior of AA6061. The method was improved in order to include additional data in the identification procedure of complex yield criteria. To investigate the anisotropic plastic behavior of AA6061, biaxial tensile tests have been performed at different temperatures (-40°C, ambient, 160°C) and tensile velocities (1mm/s and 200mm/s). Experimental data (forces and strain fields) have been successfully measured by using the biaxial testing machine equipped with an air flow generator.

The Bron and Besson yield criterion is firstly identified for the lower speed and at ambient temperature. The identified yield model can well describe the evolution of principal strains for different strain states. After that, this yield criterion is combined with a temperature and strain rate sensitive hardening model in order to predict the strain fields for the tested temperatures and strain rates. Through the comparison between experimental and numerical principal strains and strain path ratios along with different profiles, the combined material model can give a suitable prediction of the strain field. Nevertheless, for some conditions (high temperature (160°C) and low temperature (-40°C) with high strain rate) the parameters of the yield criterion need to be adjusted in order to include the coupling effect of temperature and strain rate.

Conclusions and perspectives

The main objective of this thesis was to contribute to the improvement and reliability of calibration methods of thermo-viscoplastic behavior of metal sheets under biaxial loadings. The strategy has been validated by the identification of thermo-viscoplastic hardening model for AA6061 with an in-plane biaxial tensile test at various temperatures and strain rates. The identified hardening model was also applied to discuss the temperature and strain rate effect on the anisotropy plastic behavior of AA6061.

The conclusions of this work are summarized as follows:

- ✓ The hardening behavior of AA6061 shows a significant temperature dependency for a given strain rate. The strain rate dependency is emphasized at high temperatures. Both power and saturation type models give a good description of flow stress at a strain level < 15% for this material. While for higher strains, saturation-type models tend to give better predictive results.

- ✓ A heating system has been successfully used in the in-plane biaxial tensile test. The temperature on the specimen can be precisely controlled and kept homogeneous just before the test. With two dedicated cruciform specimens, the tensile forces and strain fields in the central zone of the specimen at different temperatures and tensile velocities have been successfully measured by using the biaxial testing machine equipped with an air flow generator. The thermo-viscoplastic hardening model for AA6061 identified from the in-plane biaxial tensile tests at different conditions presents a good agreement with experimental data in a temperature range from 20°C to 160°C and strain rates from 10^{-3} to $10s^{-1}$. The strategy of identifying the thermo-viscoplastic hardening model by considering multiple sets of experimental data simultaneously is validated.

- ✓ The methodology of identification of an anisotropic yield criterion, based on a unique equi-biaxial tensile test has been improved by adding two additional strain profiles in the identification procedure. The Bron and Besson yield criterion identified with this improved method gives a good prediction of strain fields for different strain states for AA5086 and AA6061 at room temperature and for quasi-static conditions.

- ✓ The identified yield model associated with the thermo-viscoplastic hardening model can give a suitable prediction of strain field at low strain rate and low temperature, but for high strain rate or temperature conditions, the yield model need to be adjusted in order to include the coupling effect of temperature and strain rate.

In the future, several perspectives are suggested as following:

- ➢ Thanks to the biaxial machine, non-proportional loadings can be applied. The applied velocities can be different along the two perpendicular directions and can change

independently during the test. For these conditions, complex strain paths can be followed in order to replicate the actual strain paths observed in some forming processes. In that case, the identification of advanced combined isotropic-kinematic hardening models, including the coupling effect of temperature and strain rate, should be possible according to the proposed method.

- For the AA6061, the parameters of the anisotropic yield criterion seem to be sensitive to the conditions of temperatures and strain rates. It could be interesting to identify the parameters of the yield criterion for each tested condition in order to see if a significant evolution of some parameters is observed. This might be a first step in order to make reliable the identification of the hardening model on a wide range of temperatures and strain rates.

Reference

[1] Zhang X, Chen Z, Liu Y. The Material Point Method: A Continuum-Based Particle Method for Extreme Loading Cases. Academic Press; 2016.

[2] Choi S-H, Brem JC, Barlat F, Oh KH. Macroscopic anisotropy in AA5019A sheets. Acta Mater 2000;48:1853–63. https://doi.org/10.1016/S1359-6454(99)00470-X.

[3] Kobayashi S, Oh S-I, Altan T. Metal Forming and the Finite-element Method. Oxford University Press; 1989.

[4] Hu J, Marciniak Z, Duncan J. Mechanics of Sheet Metal Forming. Elsevier; 2002.

[5] Banabic D. Sheet Metal Forming Processes: Constitutive Modelling and Numerical Simulation. Springer Science & Business Media; 2010.

[6] Hill R, Orowan E. A theory of the yielding and plastic flow of anisotropic metals. Proc R Soc Lond Ser Math Phys Sci 1948;193:281–97. https://doi.org/10.1098/rspa.1948.0045.

[7] Banabic D, Bunge HJ, Pöhlandt K, Tekkaya AE. Formability of Metallic Materials: Plastic Anisotropy, Formability Testing, Forming Limits. Springer Science & Business Media; 2013.

[7] Hosford W F. On yield loci of anisotropic cubic metals[C]//Proceedings of the Seventh North American Metal working Conference SME. 1979: 191-197.

[9] Barlat F, Lege DJ, Brem JC. A six-component yield function for anisotropic materials. Int J Plast 1991;7:693–712. https://doi.org/10.1016/0749-6419(91)90052-Z.

[11] Texture and Planar Anisotropy of *r*-Value in Duplex Stainless Steel Sheet n.d. https://www.jstage.jst.go.jp/article/matertrans/51/4/51_MG200908/_article/-char/ja/.

[11] Barlat F, Maeda Y, Chung K, Yanagawa M, Brem JC, Hayashida Y, et al. Yield function development for aluminum alloy sheets. J Mech Phys Solids 1997;45:1727–63. https://doi.org/10.1016/S0022-5096(97)00034-3.

[12] Karafillis AP, Boyce MC. A general anisotropic yield criterion using bounds and a transformation weighting tensor. J Mech Phys Solids 1993;41:1859–86. https://doi.org/10.1016/0022-5096(93)90073-O.

[13] Barlat F, Becker RC, Hayashida Y, Maeda Y, Yanagawa M, Chung K, et al. Yielding description for solution strengthened aluminum alloys. Int J Plast 1997;13:385–401. https://doi.org/10.1016/S0749-6419(97)80005-8.

[14] Bron F, Besson J. A yield function for anisotropic materials Application to aluminum alloys. Int J Plast 2004;20:937–63. https://doi.org/10.1016/j.ijplas.2003.06.001.

[15] Zhang S, Leotoing L, Guines D, Thuillier S, Zang S. Calibration of anisotropic yield criterion with conventional tests or biaxial test. Int J Mech Sci 2014;85:142–51. https://doi.org/10.1016/j.ijmecsci.2014.05.020.

[16] Chung K, Lee SY, Barlat F, Keum YT, Park JM. Finite element simulation of sheet forming based on a planar anisotropic strain-rate potential. Int J Plast 1996;12:93–115. https://doi.org/10.1016/S0749-6419(95)00046-1.

[17] Kurukuri S, Miroux A, Ghosh M, van den Boogaard AH. Effect of temperature on anisotropy in forming simulation of aluminum alloys. Int J Mater Form 2009;2:387–90. https://doi.org/10.1007/s12289-009-0462-4.

[18] Abedrabbo N, Pourboghrat F, Carsley J. Forming of aluminum alloys at elevated

temperatures – Part 1: Material characterization. Int J Plast 2006;22:314–41. https://doi.org/10.1016/j.ijplas.2005.03.005.

[19] Khan AS, Baig M. Anisotropic responses, constitutive modeling and the effects of strain-rate and temperature on the formability of an aluminum alloy. Int J Plast 2011;27:522–38. https://doi.org/10.1016/j.ijplas.2010.08.001.

[20] Zadpoor AA, Sinke J, Benedictus R. 4 - Numerical simulation modeling of tailor welded blank forming. In: Kinsey BL, Wu X, editors. Tailor Welded Blanks Adv. Manuf., Woodhead Publishing; 2011, p. 68–94. https://doi.org/10.1533/9780857093851.1.68.

[21] Salvado FC, Teixeira-Dias F, Walley SM, Lea LJ, Cardoso JB. A review on the strain rate dependency of the dynamic viscoplastic response of FCC metals. Prog Mater Sci 2017;88:186–231. https://doi.org/10.1016/j.pmatsci.2017.04.004.

[22] Panov V. Modelling of behaviour of metals at high strain rates 2006.

[23] Huang C-Q, Deng J, Wang S-X, Liu L. A physical-based constitutive model to describe the strain-hardening and dynamic recovery behaviors of 5754 aluminum alloy. Mater Sci Eng A 2017;699:106–13. https://doi.org/10.1016/j.msea.2017.04.086.

[24] Vilamosa V, Clausen AH, Børvik T, Holmedal B, Hopperstad OS. A physically-based constitutive model applied to AA6082 aluminium alloy at large strains, high strain rates and elevated temperatures. Mater Des 2016;103:391–405. https://doi.org/10.1016/j.matdes.2016.04.047.

[25] Knezevic M, Beyerlein IJ, Lovato ML, Tomé CN, Richards AW, McCabe RJ. A strain-rate and temperature dependent constitutive model for BCC metals incorporating non-Schmid effects: Application to tantalum–tungsten alloys. Int J Plast 2014;62:93–104. https://doi.org/10.1016/j.ijplas.2014.07.007.

[26] Bobbili R, Madhu V. Physically-based constitutive model for flow behavior of a Ti-22Al-25Nb alloy at high strain rates. J Alloys Compd 2018;762:842–8. https://doi.org/10.1016/j.jallcom.2018.05.252.

[27] Chu X. Caractérisation expérimentale et prédiction de la formabilité d'un alliage d'aluminium en fonction de la température et de la vitesse de déformation. phdthesis. INSA de Rennes, 2013.

[28] Lemaitre J, Chaboche J-L, Benallal A, Desmorat R. Mécanique des matériaux solides. vol. 2. Dunod Paris; 1985.

[29] Huh H, Ahn K, Lim JH, Kim HW, Park LJ. Evaluation of dynamic hardening models for BCC, FCC, and HCP metals at a wide range of strain rates. J Mater Process Technol 2014;214:1326–40. https://doi.org/10.1016/j.jmatprotec.2014.02.004.

[30] Diot S. Caractérisation expérimentale et numérique. thesis. Rennes, INSA, 2003.

[31] Paul SK, Raj A, Biswas P, Manikandan G, Verma RK. Tensile flow behavior of ultra low carbon, low carbon and micro alloyed steel sheets for auto application under low to intermediate strain rate. Mater Des 2014;57:211–7. https://doi.org/10.1016/j.matdes.2013.12.047.

[32] Sung JH, Kim JH, Wagoner RH. A plastic constitutive equation incorporating strain, strain-rate, and temperature. Int J Plast 2010;26:1746–71. https://doi.org/10.1016/j.ijplas.2010.02.005.

[34] The temperature dependence of the yield stress of polycrystalline iron: The Philosophical Magazine: A Journal of Theoretical Experimental and Applied Physics: Vol 8, No 85 n.d. https://www.tandfonline.com/doi/abs/10.1080/14786436308212493.

[34] Rusinek A, Rodríguez-Martínez JA, Arias A. A thermo-viscoplastic constitutive model for FCC metals with application to OFHC copper. Int J Mech Sci 2010;52:120–35. https://doi.org/10.1016/j.ijmecsci.2009.07.001.

[35] Johnson GR, Cook WH. A Constitutive Model And Data For Metals n.d.:7.

[36] Chen S, Huang C, Wang C, Duan Z. Mechanical properties and constitutive relationships of 30CrMnSiA steel heated at high rate. Mater Sci Eng A 2008;483–484:105–8. https://doi.org/10.1016/j.msea.2006.09.132.

[37] Chu X, Leotoing L, Guines D, Ragneau E. Temperature and strain rate influence on AA5086 Forming Limit Curves: Experimental results and discussion on the validity of the M-K model. Int J Mech Sci 2014;78:27–34. https://doi.org/10.1016/j.ijmecsci.2013.11.002.

[38] Liang J, Guines D, Léotoing L. Thermo-viscoplastic behavior of AA6061 under dynamic biaxial loadings. AIP Conf. Proc., vol. 2113, AIP Publishing LLC; 2019, p. 180014.

[39] Kocks UF, Mecking H. Physics and phenomenology of strain hardening: the FCC case. Prog Mater Sci 2003;48:171–273. https://doi.org/10.1016/S0079-6425(02)00003-8.

[40] Gavrus A, Davoodi B, Ragneau E. A study of material constitutive behaviour at elevated temperature from compressive SHPB test using an inverse analysis method. J Phys IV Proc 2006;134:661–6. https://doi.org/10.1051/jp4:2006134102.

[41] Børvik T, Hopperstad OS, Berstad T, Langseth M. A computational model of viscoplasticity and ductile damage for impact and penetration. Eur J Mech - ASolids 2001;20:685–712. https://doi.org/10.1016/S0997-7538(01)01157-3.

[42] Rule WK, Jones SE. A REVISED FORM FOR THE JOHNSON–COOK STRENGTH MODEL. Int J Impact Eng 1998;21:609–24. https://doi.org/10.1016/S0734-743X(97)00081-X.

[43] Zhang H, Wen W, Cui H. Behaviors of IC10 alloy over a wide range of strain rates and temperatures: Experiments and modeling. Mater Sci Eng -Struct Mater Prop Microstruct Process - MATER SCI ENG -STRUCT MATER 2009;504:99–103. https://doi.org/10.1016/j.msea.2008.10.056.

[44] Vural M, Caro J. Experimental analysis and constitutive modeling for the newly developed 2139-T8 alloy. Mater Sci Eng A 2009;520:56–65. https://doi.org/10.1016/j.msea.2009.05.026.

[45] Lin YC, Xia Y-C, Xiao-Min C, Chen M-S. Constitutive descriptions for hot compressed 2124-T851 aluminum alloy over a wide range of temperature and strain rate. Comput Mater Sci - COMPUT MATER SCI 2010;50:227–33. https://doi.org/10.1016/j.commatsci.2010.08.003.

[46] Lin YC, Chen X-M, Liu G. A modified Johnson–Cook model for tensile behaviors of typical high-strength alloy steel. Mater Sci Eng A 2010;527:6980–6. https://doi.org/10.1016/j.msea.2010.07.061.

[47] Shin H, Kim J-B. A Phenomenological Constitutive Equation to Describe Various Flow Stress Behaviors of Materials in Wide Strain Rate and Temperature Regimes. J Eng Mater Technol 2010;132. https://doi.org/10.1115/1.4000225.

[48] Wang Y, Zhou Y, Xia Y. A constitutive description of tensile behavior for brass over a wide range of strain rates. Mater Sci Eng A 2004;372:186–90. https://doi.org/10.1016/j.msea.2003.12.009.

[49] Hou QY, Wang JT. A modified Johnson–Cook constitutive model for Mg–Gd–Y alloy extended to a wide range of temperatures. Comput Mater Sci 2010;50:147–52.

https://doi.org/10.1016/j.commatsci.2010.07.018.

[50] Lin YC, Li Q-F, Xia Y-C, Li L-T. A phenomenological constitutive model for high temperature flow stress prediction of Al–Cu–Mg alloy. Mater Sci Eng A 2012;534:654–662. https://doi.org/10.1016/j.msea.2011.12.023.

[51] Khan AS, Huang S. Experimental and theoretical study of mechanical behavior of 1100 aluminum in the strain rate range 10−5−104s−1. Int J Plast 1992;8:397–424. https://doi.org/10.1016/0749-6419(92)90057-J.

[52] Khan AS, Liang R. Behaviors of three BCC metal over a wide range of strain rates and temperatures: experiments and modeling. Int J Plast 1999;15:1089–109. https://doi.org/10.1016/S0749-6419(99)00030-3.

[53] Zerilli FJ, Armstrong RW. Dislocation ‐ mechanics ‐ based constitutive relations for material dynamics calculations. J Appl Phys 1987;61:1816–25. https://doi.org/10.1063/1.338024.

[54] Yu H, Guo Y, Zhang K, Lai X. Constitutive model on the description of plastic behavior of DP600 steel at strain rate from 10−4 to 103s−1. Comput Mater Sci 2009;46:36–41. https://doi.org/10.1016/j.commatsci.2009.01.025.

[55] Li D, Ghosh A. Tensile deformation behavior of aluminum alloys at warm forming temperatures. Mater Sci Eng A 2003;352:279–86. https://doi.org/10.1016/S0921-5093(02)00915-2.

[56] Abedrabbo N, Pourboghrat F, Carsley J. Forming of AA5182-O and AA5754-O at elevated temperatures using coupled thermo-mechanical finite element models. Int J Plast 2007;23:841–75. https://doi.org/10.1016/j.ijplas.2006.10.005.

[57] Codrington J, Nguyen P, Ho SY, Kotousov A. Induction heating apparatus for high temperature testing of thermo-mechanical properties. Appl Therm Eng 2009;29:2783–9. https://doi.org/10.1016/j.applthermaleng.2009.01.013.

[58] Chen Z, Fang G, Zhao J-Q. Formability Evaluation of Aluminum Alloy 6061-T6 Sheet at Room and Elevated Temperatures. J Mater Eng Perform 2017;26:4626–37. https://doi.org/10.1007/s11665-017-2895-0.

[59] Bouvier S, Haddadi H, Levée P, Teodosiu C. Simple shear tests: Experimental techniques and characterization of the plastic anisotropy of rolled sheets at large strains. J Mater Process Technol 2006;172:96–103. https://doi.org/10.1016/j.jmatprotec.2005.09.003.

[60] B07 Committee. Test Method for Shear Testing of Thin Aluminum Alloy Products. ASTM International; n.d. https://doi.org/10.1520/B0831-05.

[61] Merklein M, Biasutti M. Forward and reverse simple shear test experiments for material modeling in forming simulations. Proc. 10th Int. Conf. Technol. Plast. ICTP, 2011, p. 702–707.

[62] Yin Q, Zillmann B, Suttner S, Gerstein G, Biasutti M, Tekkaya AE, et al. An experimental and numerical investigation of different shear test configurations for sheet metal characterization. Int J Solids Struct 2014;51:1066–74. https://doi.org/10.1016/j.ijsolstr.2013.12.006.

[63] Pellegrino S, Fratini L, Merklein M, Böhm W, Nguyen H. Modeling of the Plastic Characteristics of AA6082 for the Friction Stir Welding Process. Key Eng Mater 2015;639:309–16. https://doi.org/10.4028/www.scientific.net/KEM.639.309.

[64] Bernard C, Coër J, Laurent H, Manach PY, Oliveira M, Menezes LF. Influence of Portevin-Le Chatelier Effect on Shear Strain Path Reversal in an Al-Mg Alloy at Room and High Temperatures. Exp Mech 2017;57:405–15. https://doi.org/10.1007/s11340-016-

0229-z.

[65] Edwards NJ, Kariem MA, Rashid RAR, Cimpoeru SJ, Lu G, Ruan D. Dynamic shear testing of 2024 T351 aluminium at elevated temperature. Mater Sci Eng A 2019;754:99–111. https://doi.org/10.1016/j.msea.2019.03.033.

[66] Peirs J, Verleysen P, Van Paepegem W, Degrieck J. Novel pure-shear sheet specimen geometry for dynamic material characterisation. DYMAT 2009 - 9th Int. Conf. Mech. Phys. Behav. Mater. Dyn. Load., vol. 1, Brussels, Belgium: EDP Sciences; 2009, p. 35–41. https://doi.org/10.1051/dymat/2009005.

[67] Bouvier S, Gardey B, Haddadi H, Teodosiu C. Characterization of the strain-induced plastic anisotropy of rolled sheets by using sequences of simple shear and uniaxial tensile tests. J Mater Process Technol 2006;174:115–26. https://doi.org/10.1016/j.jmatprotec.2005.04.086.

[68] Rees DWA. Plane strain compression of aluminium alloy sheets. Mater Des 2012;39:495–503. https://doi.org/10.1016/j.matdes.2012.03.015.

[69] Loveday MS, Mahon GJ, Roebuck B, Lacey AJ, Palmiere EJ, Sellars CM. Measurement of flow stress in hot plane strain compression tests n.d.:34.

[70] Boldetti C, Pinna C, Howard IC. Measurement and prediction of deformation in plane strain compression tests of AA5182. Mater Sci Technol 2006;22:1380–6. https://doi.org/10.1179/174328406X118375.

[71] Cheng L, Xue X, Tang B, Liu D, Li J, Kou H, et al. Deformation behavior of hot-rolled IN718 superalloy under plane strain compression at elevated temperature. Mater Sci Eng A 2014;606:24–30. https://doi.org/10.1016/j.msea.2014.03.075.

[72] Xiao Y, Liu H, Yi D, Le J, Zhou H, Jiang Y, et al. High-Temperature Deformation Behavior of Ti-6Al-2Sn-4Zr-2Mo Alloy with Lamellar Microstructure Under Plane-Strain Compression. J Mater Eng Perform 2018;27:4941–54. https://doi.org/10.1007/s11665-018-3573-6.

[74] Gleeble 3800-GTC n.d. https://www.gleeble.com/products/gleeble-systems/gleeble-3800.html.

[74] An YG, Vegter H, Elliott L. A novel and simple method for the measurement of plane strain work hardening. J Mater Process Technol 2004;155–156:1616–22. https://doi.org/10.1016/j.jmatprotec.2004.04.344.

[75] Gutscher G, Wu H-C, Ngaile G, Altan T. Determination of flow stress for sheet metal forming using the viscous pressure bulge (VPB) test. J Mater Process Technol 2004;146:1–7. https://doi.org/10.1016/S0924-0136(03)00838-0.

[76] Lăzărescu L, Comşa D-S, Nicodim I, Ciobanu I, Banabic D. Characterization of plastic behaviour of sheet metals by hydraulic bulge test. Trans Nonferrous Met Soc China 2012;22:s275–9. https://doi.org/10.1016/S1003-6326(12)61719-1.

[77] Kalkman AJ, Verbruggen AH, Janssen GCAM. High-temperature bulge-test setup for mechanical testing of free-standing thin films. Rev Sci Instrum 2003;74:1383–5. https://doi.org/10.1063/1.1539901.

[78] Mahabunphachai S, Koç M. Investigations on forming of aluminum 5052 and 6061 sheet alloys at warm temperatures. Mater Des 1980-2015 2010;31:2422–34. https://doi.org/10.1016/j.matdes.2009.11.053.

[79] Liu K, Lang L, Cai G, Yang X, Guo C, Liu B. A novel approach to determine plastic hardening curves of AA7075 sheet utilizing hydraulic bulging test at elevated temperature. Int J Mech Sci 2015;100:328–38. https://doi.org/10.1016/j.ijmecsci.2015.07.002.

[80] Ramezani M, Ripin ZM, Ahmad R. Plastic bulging of sheet metals at high strain rates. Int J Adv Manuf Technol 2010;48:847–58. https://doi.org/10.1007/s00170-009-2335-x.

[81] Grolleau V, Gary G, Mohr D. Biaxial Testing of Sheet Materials at High Strain Rates Using Viscoelastic Bars. Exp Mech 2008;48:293–306. https://doi.org/10.1007/s11340-007-9073-5.

[82] Makinde A, Thibodeau L, Neale KW. Development of an apparatus for biaxial testing using cruciform specimens. Exp Mech 1992;32:138–44. https://doi.org/10.1007/BF02324725.

[83] Kuwabara T, Ikeda S, Kuroda K. Measurement and analysis of differential work hardening in cold-rolled steel sheet under biaxial tension. J Mater Process Technol 1998;80–81:517–23. https://doi.org/10.1016/S0924-0136(98)00155-1.

[84] Hannon A, Tiernan P. A review of planar biaxial tensile test systems for sheet metal. J Mater Process Technol 2008;198:1–13. https://doi.org/10.1016/j.jmatprotec.2007.10.015.

[85] Tiernan P, Hannon A. Design optimisation of biaxial tensile test specimen using finite element analysis. Int J Mater Form 2014;7:117–23. https://doi.org/10.1007/s12289-012-1105-8.

[86] Ohtake Y, Rokugawa S, Masumoto H. Geometry Determination of Cruciform-Type Specimen and Biaxial Tensile Test of C/C Composites. Key Eng Mater 1998;164–165:151–4. https://doi.org/10.4028/www.scientific.net/KEM.164-165.151.

[87] Kuwabara T, Van Bael A, Iizuka E. Measurement and analysis of yield locus and work hardening characteristics of steel sheets wtih different r-values. Acta Mater 2002;50:3717–29. https://doi.org/10.1016/S1359-6454(02)00184-2.

[88] Naka T, Nakayama Y, Uemori T, Hino R, Yoshida F. Effects of temperature on yield locus for 5083 aluminum alloy sheet. J Mater Process Technol 2003;140:494–9. https://doi.org/10.1016/S0924-0136(03)00780-5.

[89] Naka T, Nakayama Y, Uemori T, Hino R, Yoshida F. Effect of Strain-Rate and Temperature on Yield Locus for 5083 Aluminum Alloy Sheet. Key Eng Mater 2004;274–276:937–42. https://doi.org/10.4028/www.scientific.net/KEM.274-276.937.

[90] Teaca M, Charpentier I, Martiny M, Ferron G. Identification of sheet metal plastic anisotropy using heterogeneous biaxial tensile tests. Int J Mech Sci 2010;52:572–80. https://doi.org/10.1016/j.ijmecsci.2009.12.003.

[91] Teaca M. Caractérisation expérimentale et modélisation de la déformation plastique des tôles métalliques. phdthesis. Université Paul Verlaine - Metz, 2009.

[92] Gozzi J, Olsson A. - Extra high strength steel plasticity-experimental work and constitutive modelling. In: Shen ZY, Li GQ, Chan SL, editors. Fourth Int. Conf. Adv. Steel Struct., Oxford: Elsevier Science Ltd; 2005, p. 1571–6. https://doi.org/10.1016/B978-008044637-0/50234-1.

[93] Gozzi J, Olsson A, Lagerqvist O. Experimental investigation of the behavior of extra high strength steel. Exp Mech 2005;45:533–40. https://doi.org/10.1007/BF02427907.

[94] Liu W. Identification of strainrate dependent hardening sensitivity of metallic sheets under in-plane biaxial loading. thesis. Rennes, INSA, 2015.

[95] Xiao R, Li X-X, Lang L-H, Song Q, Liu K-N. Forming limit in thermal cruciform biaxial tensile testing of titanium alloy. J Mater Process Technol 2017;240:354–61. https://doi.org/10.1016/j.jmatprotec.2016.10.016.

[96] Zidane I, Guines D, Léotoing L, Ragneau E. Development of an in-plane biaxial test for

forming limit curve (FLC) characterization of metallic sheets. Meas Sci Technol 2010;21:055701. https://doi.org/10.1088/0957-0233/21/5/055701.

[97] Song X, Leotoing L, Guines D, Ragneau E. Characterization of forming limits at fracture with an optimized cruciform specimen: Application to DP600 steel sheets. Int J Mech Sci 2017;126:35–43. https://doi.org/10.1016/j.ijmecsci.2017.03.023.

[98] Pelton AR. SMST 2003: Proceedings of the International Conference on Shape Memory and Superelastic Technologies. ASM International; 2004.

[100] Specimen for a novel concept of the biaxial tension test - ScienceDirect n.d. https://www.sciencedirect.com/science/article/abs/pii/S0924013605006242.

[101] Testing and modelling of material behaviour and formability in sheet metal forming - ScienceDirect n.d. https://www.sciencedirect.com/science/article/abs/pii/S0007850614001875.

[101] Geiger M, Van der Heyd G, Merklein M, Hussnätter W. Novel concept of experimental setup for characterisation of plastic yielding of sheet metal at elevated temperatures. Adv. Mater. Res., vol. 6, Trans Tech Publ; 2005, p. 657–664.

[102] Abu-Farha F, Hector LG, Khraisheh M. Cruciform-shaped specimens for elevated temperature biaxial testing of lightweight materials. Jom 2009;61:48–56.

[103] Kulawinski D, Henkel S, Holländer D, Thiele M, Gampe U, Biermann H. Fatigue behavior of the nickel-base superalloy Waspaloy^{TM} under proportional biaxial-planar loading at high temperature. Int J Fatigue 2014;67:212–219.

[104] Xiao R, Li X-X, Lang L-H, Chen Y-K, Yang Y-F. Biaxial tensile testing of cruciform slim superalloy at elevated temperatures. Mater Des 2016;94:286–94. https://doi.org/10.1016/j.matdes.2016.01.045.

[105] Shao Z, Li N, Lin J, Dean TA. Development of a New Biaxial Testing System for Generating Forming Limit Diagrams for Sheet Metals Under Hot Stamping Conditions. Exp Mech 2016;56:1489–500. https://doi.org/10.1007/s11340-016-0183-9.

[106] Xiao R. A Review of Cruciform Biaxial Tensile Testing of Sheet Metals. Exp Tech 2019;43:501–20. https://doi.org/10.1007/s40799-018-00297-6.

[107] Murtha SJ. New 6XXX Aluminum Alloy for Automotive Body Sheet Applications. SAE Trans 1995;104:657–66.

[108] Dorbane A, Ayoub G, Mansoor B, Hamade R, Kridli G, Imad A. Observations of the mechanical response and evolution of damage of AA 6061-T6 under different strain rates and temperatures. Mater Sci Eng A 2015;624:239–49. https://doi.org/10.1016/j.msea.2014.11.074.

[109] Agarwal H, Gokhale AM, Graham S, Horstemeyer MF. Void growth in 6061-aluminum alloy under triaxial stress state. Mater Sci Eng A 2003;341:35–42. https://doi.org/10.1016/S0921-5093(02)00073-4.

[110] Fan X, Suo T, Sun Q, Wang T. Dynamic mechanical behavior of 6061 al alloy at elevated temperatures and different strain rates. Acta Mech Solida Sin 2013;26:111–20. https://doi.org/10.1016/S0894-9166(13)60011-7.

[111] Mohamed MS, Foster AD, Lin J, Balint DS, Dean TA. Investigation of deformation and failure features in hot stamping of AA6082: Experimentation and modelling. Int J Mach Tools Manuf 2012;53:27–38. https://doi.org/10.1016/j.ijmachtools.2011.07.005.

[113] ASM Material Data Sheet n.d. http://asm.matweb.com/search/SpecificMaterial.asp?bassnum=MA6061O.

[113] Flanigan AE, Tedsen LF, Dorn JE. Tensile properties affecting the formability of aluminum-alloy sheet at elevated temperatures. J Aeronaut Sci 1946;13:457–468.

[114] Yao X, Zajac S. The strain-rate dependence of flow stress and work-hardening rate in three Al-Mg alloys. Scand J Metall 2000;29:101–107.

[115] Aretz H. An extension of Hill's localized necking model. Int J Eng Sci 2010;48:312–31. https://doi.org/10.1016/j.ijengsci.2009.09.007.

[116] Zhang S. Characterization of anisotropic yield criterion with biaxial tension test. PhD Thesis. PhD thesis at Université de INSA Rennes, 2014.

[118] modeFRONTIER n.d. https://ww2.mathworks.cn/products/connections/product_detail/modefrontier.html.

[118] Liu W. Identification of strainrate dependent hardening sensitivity of metallic sheets under in-plane biaxial loading. PhD Thesis. Rennes, INSA, 2015.

[119] Song X, Leotoing L, Guines D, Ragneau E. Identification of forming limits at fracture of DP600 sheet metal under linear and unloaded non-linear strain paths. Procedia Eng 2017;207:562–7. https://doi.org/10.1016/j.proeng.2017.10.1021.

[120] Liu W, Guines D, Leotoing L, Ragneau E. Identification of sheet metal hardening for large strains with an in-plane biaxial tensile test and a dedicated cross specimen. Int J Mech Sci 2015;101–102:387–98. https://doi.org/10.1016/j.ijmecsci.2015.08.022.

[121] Hähner P, Rizzi E. On the kinematics of Portevin–Le Chatelier bands: theoretical and numerical modelling. Acta Mater 2003;51:3385–97. https://doi.org/10.1016/S1359-6454(03)00122-8.

INSA de RENNES
Service des Formations

AVIS DU JURY SUR LA REPRODUCTION DE LA THESE SOUTENUE

Titre de la thèse:
Characterization of thermo-viscoplastic behavior of metallic alloys under dynamic biaxial loadings

Nom Prénom de l'auteur : LIANG JIABIN

Membres du jury :
- Madame BOUDEAU Nathalie
- Monsieur LABERGERE Carl
- Monsieur MERAGHNI Fodil
- Monsieur GUINES Dominique
- Monsieur LEOTOING Lionel

Président du jury : **Prof. Fodil MERAGHNI**

Date de la soutenance : 03 Juin 2020

Reproduction de la these soutenue

☒ **Thèse pouvant être reproduite en l'état**

☐ ~~Thèse pouvant être reproduite après corrections suggérées~~

Fait à Rennes, le 03 Juin 2020

Signature du président de jury
Prof. Fodil MERAGHNI

Le Directeur,

M'hamed DRISSI

DOCTORAT BRETAGNE SCIENCES LOIRE POUR L'INGENIEUR

INSA RENNES

Titre : Caractérisation du comportement thermo-viscoplastique d'alliages métalliques soumis à des chargements dynamiques biaxiaux

Mots clés : Traction biaxiale ; anisotropie ; écrouissage thermo-viscoplastique ; analyse inverse

Résumé : Des travaux récents ont montré tout l'intérêt de l'essai de traction biaxial sur éprouvette plane en croix pour la caractérisation des comportements rhéologiques des tôles métalliques soumises à des chargements complexes. L'objectif de ce travail est de proposer une méthode de calibration des modèles de comportement plastique (écrouissage thermo-viscoplastique, anisotropie) pour les tôles métalliques soumises à des chargements biaxiaux. On s'intéresse ici à un alliage d'aluminium AA6061. Un dispositif expérimental de traction dynamique biaxiale est utilisé conjointement avec des éprouvettes cruciformes de formes dédiées. La base de données expérimentale établie couvre une plage de température de l'ambiante à environ 200°C et une gamme de vitesse de déformation allant du quasi-statique à 5/s.

La calibration de critères de plasticité anisotropes complexes (comme le critère de Bron et Besson) et de modèles d'écrouissage thermo-viscoplastique est effectuée par une procédure inverse. Cette procédure s'appuie sur une modélisation EF de l'essai de traction biaxiale, la mesure de l'effort selon les deux axes de l'éprouvette et la détermination du champ de déformation par technique de corrélation d'image dans la partie centrale de l'éprouvette. L'identification du critère plastique anisotrope est effectuée sur un essai équibiaxial unique dans des conditions de traction quasi-statique à température ambiante alors que l'écrouissage est calibré à partir de plusieurs essais de traction équi-biaxiaux réalisés à différentes vitesses et températures.

Title : Characterization of thermo-viscoplastic behavior of metallic alloys under dynamic biaxial loadings

Keywords : Biaxial tension ; anisotropic behavior ; thermo-viscoplastic hardening ; inverse analysis

Abstract : Several recent works have shown the interest of the biaxial tensile test on a flat cross section specimen for the characterization of rheological behaviors (limit behaviors, strain hardening, anisotropy, ...) of thin sheet metallic materials subjected to complex loadings (biaxial, linear or non-linear). In this work, a calibrating method of plastic behavior models of metallic sheets subjected to biaxial loading is proposed and illustrated through the characterization of an aluminium alloy AA6061. For this purpose, an experimental biaxial dynamic tensile testing device is used to perform tensile tests on cruciform specimens of dedicated shapes. The established experimental database covers a temperature range from room temperature to about 200°C and a strain rate range from quasi-static to 5/sec.

From this database, the calibration of complex anisotropic plasticity criteria (Bron and Besson criteria) and thermo-viscoplastic strain-hardening models are performed by an inverse procedure. This procedure is based on a FE modeling of the biaxial tensile test, force measurements along the two axes of the specimen and determination of the strain field in the specimen central area. The identification of the parameters of the anisotropic plastic criterion is carried out on a single equibiaxial test under quasi-static tensile conditions at room temperature while the strain hardening is calibrated from several equibiaxial tensile tests carried out at different speeds and temperatures. Results highlight the potential of the biaxial tensile test on a flat specimen for the calibration of thermo-viscoplastic models used in forming applications where large strains are encountered.